The Dissertation Committee for Yi Lu Certifies that this is the approved version of the following dissertation:

Micro/Nano Fabrication of Polymeric Materials by DMD-based Micro-Stereolithography and Photothermal Imprinting

Committee:

Shaochen Chen, Supervisor

Li Shi

John R. Howell

Krishnendu Roy

Christine Schmidt

Micro/Nano Fabrication of Polymeric Materials by DMD-based Micro-Stereolithography and Photothermal Imprinting

by

Yi Lu, B.S., M.S.

Dissertation

Presented to the Faculty of the Graduate School of
The University of Texas at Austin
in Partial Fulfillment
of the Requirements
for the Degree of

Doctor of Philosophy

The University of Texas at Austin
December 2006

Dedication

To my parents and wife

Acknowledgements

Firstly, I would like to thank my advisor Professor Shaochen Chen for his guidance, encouragement and financial support throughout my graduate study at University of Texas at Austin. He has been my advisor: his knowledgeable, experienced, and resourceful; He has inspired and guided me to find out solutions to problems. He has been my mentor:

I would also like to acknowledge the valuable comments and feedback from Prof. Schmidt and Prof. Roy for my research in the biomedical area; Prof. Li Shi in microfabrication; Prof. Howell in numerical modeling. It has been a great pleasure to work and interact with my fellow graduate and undergraduate students in our group, Gazell Mapili in Prof. Roy's group, and Natalia Gomez in Prof. Schmidt's group.

I am deeply indebted to my parents and my wife for their love, blessing, and understanding. They have always offered unconditioned support encouragement for my endeavors. My mother has given me nothing less than the love and care any child could ever imagine. Together, she and I have gone through physical and emotional difficulties. She put the pain and hardness on her shoulders, while letting me focus on my studies. Rather than simply appreciate her support, I would dedicate this dissertation to her.

Micro/Nano Fabrication of Polymeric Materials by DMD-based Micro-Stereolithography and Photothermal Imprinting

Publication No._____________

Yi Lu, Ph.D.
The University of Texas at Austin, 2006

Supervisor: Shaochen Chen

The revolutionary advancement in semiconductor device manufacturing promoted micro/nano fabrication technologies viable for research and applications in broader fields such as biology and optics. This dissertation is aimed at developing parallel fabrication technologies for polymeric micro/nano structures that can potentially be used in biomedical or optical devices. The objective of the dissertation is three told: a) develop and characterize a digital micro-mirror device (DMD)-based micro-stereolithographic system and explore the fabrication of hydrogel tissue engineering scaffolds, b) use the micro-stereolithographic system to fabricate microlens arrays, c) develop a photothermal imprinting technique to pattern nanostructures on the surface of polymer composites.

In the first part of the dissertation, we demonstrated a simple and fast, layer-by-layer micro-stereolithographic system based on DMD dynamic photomask that allows fabrication of complex internal features along the precise spatial distribution of biological factors inside a single scaffold. Photo-crosslinkable poly(ethylene glycol) diacrylate and diamethacrylate were used as the scaffold material. In situ encapsulation of fluorescently-labeled micro-particles and cells was demonstrated. We investigated the photopolymerization process and its effects on the properties of the scaffolds. This technique could provide a powerful tool in studying progenitor cell behavior and differentiation under biomimetic, three-dimensional (3D) culture conditions.

In the second part, we developed a novel fabrication technique for microlens arrays using a modified DMD-based micro-stereolithographic system. The DMD can generate high resolution images with quasi-continuous intensity gradient, thanks to its high density mirror elements with a bandwidth of 10 KHz. The projected UV patterns were simply drawn in a computer software. Topographic patterns were created in photocurable resin by spatially controlling the curing depth. Spherical microlens arrays were fabricated and their optical performance was characterized. This technique is capable of fabricating optical elements with any surface topography.

In the third part, we discussed the photo-induced radical polymerization. A numerical model was established to correlate the geometry of the resulting gels and system parameters.

In the fourth part, we reported a laser-assisted photothermal imprinting method for directly patterning carbon nanofiber reinforced polyethylene nanocomposite. A single laser pulse was used to melt/soften a thin skin layer of polymer nanocomposite. Meanwhile, high resolution patterns were transferred from a quartz mold to the surface of the composite.

Table of Contents

List of Tables

List of Figures

Chapter 1: Introduction to Photo-based Micro/Nano Fabrication

Microfabrication is a process used to construct physical objects with dimensions in the micrometer to millimeter range. It takes advantage of established semiconductor fabrication processes and augments these with processes specially developed for microfabrication.

Microfabricated devices may consist of a variety of miniaturized structures, including moving parts such as valves and cantilevers, static structures such as channels and reservoirs, chemical or biological bodies and surfaces such as proteins and cells, and electrical components such as resistors and transducers. They are also known as micro-electro-mechanical systems (MEMS), micromachining, lab-on-a-chip, microsystems, and micro-total analysis systems (micro TAS), have existed for decades, with several applications attaining commercial and/or scientific success. Although there have been a few applications to biology or medicine during that time, only in the past decade has a closer union emerged. Several factors have driven this recent fusion. Commercially, high-throughput, low-volume-consumption technologies such as whole genome sequencing projects and drug discovery have created a need for these devices. Scientifically, the ability to design and control experiments at the micrometer scale has attracted the interest of biologists, who have started devising fundamental studies using this technology.

Several microfabricated devices have significantly enhanced performance compared to their macro counterparts. A good example is the microfluidic polymerase chain reactor (μ-PCR) [1]. These plastic fluidic devices are fabricated using low cost, high throughput micro imprinting technique, which allows these devices to be disposable. Microfabrication also enables entirely new devices, such as precise surface patterning of arrays of fluorescent protein receptors allows for the rapid screening for the identification of specific proteins [2].

Among many microfabrication technologies, those based on photochemical and/or photophysical reactions are used ubiquitously in manufacturing as well as scientific research. Photons are “clean” particles. It provides avenue to fast and contamination free fabrication, which is essential to semiconductor manufacturing.

A variety of lithographic techniques have been derived for specific applications. Stereolithography (SL) is the first and still the most widely used three-dimensional microfabrication technique. It was developed by 3D Systems of Valencia, California, USA, founded in 1986.

SL is a liquid-based method that allows real three-dimensional microfabrication in a room-temperature environment [3, 4]. This method relies on a photosensitive monomer resin or a photocrosslinkable polymer resin which solidifies when exposed to visible or ultraviolet (UV) light. The photosensitive monomers cure via photopolymerization, while the photocrosslinkable polymers become solids or hydrogels by forming crosslinking networks. Complex 3D structures can be created in layer-by-layer fashion.

Conventional SL has greatly improved the efficacy of product designing and surgical planning and education by providing a convenient platform for rapidly creating physical and anatomical models [3].

Enhanced by high-precision optics and motion control systems, micro-stereolithography (μ-SL) system enables the fabrication of complex internal features, such as intricate passageways for microfluidic devices and curved surfaces, to be accurately produced [5]. Furthermore, the approach can easily incorporate different proteins and microparticles containing polymer solutions for each layer (or even for partial layers). This allows SL the unique ability to rapidly create a precise spatial distribution of biochemical microenvironments within a single scaffold or system.

μ-SL also provides new opportunities to micro/nano structures highly demanded in the fields of information storage and photonics [6]. Two-photon microfabrication has proven its extraordinary capability in writing arbitrary 3D structures at submicron resolution. Its serial nature still remains a drawback.

Tremendous efforts have been devoted to developing parallel 3D fabrication technology. In chapter 2, I give a briefly overview of recent advancement in 3D microfabrication technologies and their applications in tissue engineering. Our technology concept based on a digital mirror dynamic photomask will be introduced. A prototype system was built, characterized. Its capability of producing complex 3D tissue engineering scaffolds by photopolymerization reaction of biocompatible hydrogels was then demonstrated. We investigated in detail how the system parameters affect the properties of the hydrogel scaffolds.

In chapter 3, I compare our DMD-based projection method with existing microoptics fabrication technologies. Its unique advantages will be highlighted and limitations will be discussed. Proof-of-concept microlens arrays are fabricated and their optical performance is characterized.

In chapter 4, I discuss the complex photopolymerization mechanism and how a comprehensive understanding of the underlying mechanism will influence the design and fabrication of 3D microstructures not limited to tissue engineering scaffolds and microlens. A numerical model is established and its limitation is discussed.

In chapter 5, I discuss our parallel effort on nanoimprinting lithography. Nanoimprinting lithography represents a non-photolithographic strategy based on replica molding for carrying out micro- and nanofabrication. Currently, the most powerful microfabrication technique is photolithography, and essentially all integrated circuits are fabricated using this technology [7]. Projection photolithography is a parallel process: the entire pattern of the photomask can be projected onto a thin film of photoresist at the same time. State-of-the-art photolithographic techniques are capable of mass-producing patterned structures in thin films of photoresists with feature sizes as small as 45 nm, and their capability has been extended to features as small as ~ 10 nm in laboratory [8]. Reduction of feature sizes have been made possible by a combination of short wavelength light source and optical proximity corrected photomask.

Advanced lithographic techniques currently being explored as potential substitutes for conventional photolithography in the regime <100 nm include extreme UV (EUV) lithography, soft X-ray lithography, e-beam writing, focused ion beam (FIB) writing, and proximal-probe lithography [9]. These techniques have the capability to generate extremely small features, but their development into economical methods for mass-production of nanostructures still requires substantial effort: EUV and X-ray techniques, for example, require the development of reflective optics and/or new types of masks, and arrays of beams or some form of flood illumination rather than a single beam must be developed in e-beam or FIB writing [10]. Hence, technologies that can reduce the tool cost by an order of magnitude will have a significant effect on the economics of the fabrication process.

On the other hand, nano-imprint lithography, an imprint process performed at low pressure and at room temperature, can recreate the topography of a template pattern on a substrate. The key element of this technology is a rigid/elastic master that possesses surface relief structures made by e-beam lithography or interference lithography. Pattern transfer is realized by drawing contact with plastic or curable materials. This process can be repeated many times as long as the master remains free of contamination or defects. Investigations by several researchers in the sub-50 nm regime indicate that imprint lithography resolution is only limited by the resolution of the template fabrication process [11, 12]. This suggests that for high resolution lithographic features expensive projection optics or advanced illumination sources that are central to photolithography are not required. However, for nano-imprint lithography to be successfully implemented, significant aspects of the technology development need to be addressed in regards to pattern transfer fidelity, process compatibility, and high throughput.

Bearing the same underlying mechanism as its macroscopic brethren, nano-imprinting lithography often requires an elevated temperature to soften the substrate material. That induces pattern distortion due to difference in thermal expansion coefficients. Also, excessive heating may cause damage to devices beneath the surface of the substrate, making the process less compatible.

Here in this chapter I introduce a laser-assisted photothermal imprinting method, which potentially improves process compatibility and throughput.

Finally, summary and perspectives are given in Chapter 6.

Reference

[1] Yang, J.N., Liu, Y.J., Rauch, C.B., Stevens, R.L., Liu, R.H., Lenigk, R., Grodzinski, P.., *High sensitivity PCR assay in plastic micro reactors.* Lab on a Chip, 2002. **2**(4): p. 179-187.

[2] Baldini, L., Wilson, A. J., Hong, J., Hamilton, A.D., *Pattern-based detection of different proteins using an array of fluorescent protein surface receptors.* Journal of the American Chemical Society, 2004. **126**(18): p. 5656-5657.

[3] Chua, C.K., Leong, K.F., *Rapid Prototyping: Principles and Applications in Manufacturing,* John Wiley, Singapore, 1997.;

[4] Chu, T.M.G., Orton, D.G., Hollister, S.J., Feinberg, S.E., Halloran, J.W., *Mechanical and in vivo performance of hydroxyapatite implants with controlled architectures.* Biomaterials, 2002. **23**(5): p. 1283-1293.

[5] Cabral, J.T., Hudson, S.D., Harrison, C., Douglas, J.F., *Frontal photopolymerization for microfluidic applications.* Langmuir, 2004. **20**(23): p. 10020-10029.

[6] Nguyen, L.H., Straub, M., Gu, M., *Acrylate-based photopolymer for two-photon microfabrication and photonic applications.* Advanced Functional Materials, 2005. **15**(2): p. 209-216.

[7] Moreau W.M., *Semiconductor Lithography:Principles and Materials,* Plenum, New York, 1988..

[8] Intel New Release, *Intel First to Demonstrate Working 45 nm Chips*, Jan, 2006.

[9] Pease, R.F.W., *Nanolithography and Its Prospects as a Manufacturing Technology.* Journal of Vacuum Science & Technology B, 1992. **10**(1): p. 278-285.

[10] Hand, A., *Infrastructure Steps Closer to EUV Lithography*, Semiconductor International, September 1, 2005.

[11] Colburn, M., Johnson, S., Stewart, M., Damle, S., Bailey, T., Choi, B., Wedlake, M., Michaelson, T., Sreenivasan, S.V., Ekerdt, J., Willson, C.G., *Step and Flash Imprint Lithography: A new approach to high resolution patterning*, Proc. SPIE, Emerging Lithographic Technologies III, (1999) **379**: p. 3676.

[12] Chou, S.Y., Krauss, P.R., Renstrom, P.J., *Nanoimprint lithography.* Journal of Vacuum Science & Technology B, 1996. **14**(6): p. 4129-4133.

Chapter 2: Digital Micro-Mirror (DMD) Based Micro-stereolithography of Tissue Engineering Scaffolds

2.1 INTRODUCTION

Every year, millions of Americans suffer tissue loss or end-stage organ failure. The total national health care cost for these patients exceed $400B per year [1]. Physicians treat organ or tissue loss by transplanting organs from one individual to another, performing surgical reconstruction, or using mechanical (artificial) devices such as kidney dialyzers. Organ transplantation, although it has saved countless lives, is severely limited by a critical donor shortage. For example, fewer than 3,000 donors are available annually for the approximately 30,000 patients who die from liver failure [2]. Surgical reconstruction can result in long-term problems, whereas mechanical devices cannot perform all of the functions of a single organ and therefore cannot prevent progressive patient deterioration [3].

Tissue engineering is the use of a combination of cells, engineering materials, and suitable biochemical factors to improve or replace biological functions. Probably the first definition of tissue engineering was by Langer and Vacanti who stated it to be "an interdisciplinary field that applies the principles of engineering and life sciences toward the development of biological substitutes that restore, maintain, or improve tissue function or a whole organ" [3]. It has the potential to produce immunologically tolerant 'artificial' organ and tissue substitutes that can grow with the patient. This should lead to a long-term solution to the damaged organ or tissue at relatively low cost.

One of the principle methods behind tissue engineering involves growing the relevant cells in vitro into desired three-dimensional organ or tissue. Although isolated cells have the capacity to reform their respective tissue structure, they do so only to a limited degree since they have no intrinsic tissue organization and are hindered by the lack of a template to guide restructuring. Such template, known as scaffold, serves as a synthetic extracellular matrix (ECM) to organize cells into a three-dimensional architecture and to present stimuli, which direct the growth and formation of a desired tissue.

Several requirements have been identified as crucial for the production of tissue engineering scaffolds [4]: (1) the scaffold should possess interconnecting pores of appropriate scale to favor tissue integration and vascularisation, (2) be made from biocompatible and biodegradable materials so that tissue will eventually replace the scaffold, (3) have appropriate surface chemistry to favor cellular attachment, differentiation and proliferation, (4) posses adequate mechanical properties to match the intended site of implantation and handling, (5) should not induce any adverse response and, (6) be easily fabricated into a variety of shapes and sizes.

Despite recent advancements in fabricating 3D tissue engineering scaffolds, most systems are only capable of differentiating a single progenitor cell population into one particular cell lineage due to either (a) bulk incorporation of bio-factors within the scaffolding matrix or (b) exogenous delivery of hormones, chemicals, or growth factors in culture medium.

From a tissue engineering perspective, a significant advancement could be attained by creating precise, spatially distributed microenvironments within a single scaffold that would allow us to study simultaneous, patterned differentiation of stem and progenitor cells into multiple lineages and develop concepts to ultimately engineer complex, hybrid organ structures. A key step towards achieving such patterned 3D structures is the development of novel scaffold-manufacturing techniques by which distributed environments can be incorporated in a simple yet precise, reproducible fashion.

In the past decades, continuous investment has led to the rapid advances of micro/nano-fabrication technology for chemical, mechanical, or biological applications [5]. MEMS technology, known as chip-level integration of mechanical sensors and actuators, provides attractive advantage of low cost manufacturing, low power consumption, and high function integration. MEMS technologies, heavily relied on the established integrated-circuit (IC) manufacturing, have enabled three-dimensional device fabrication in micro-meter scale. However, due to the nature of silicon process, surface and bulk micromachining technology is rather limited in its ability to create complex microstructures, producing relatively simple geometries from isotropic/anisotropic etching and deposition [5]. In addition, IC micromachining technology can be only applied to materials such as common semiconductors (e.g. Si, Ge), metals (e.g. Al, Au, Ag), and dielectrics (e.g. SiO_2) [5]. It is highly desired to extend the capability of MEMS technology in making more complex microstructures from diverse materials, such as ceramics, metal alloy, and polymer.

As a novel micro-fabrication process, micro-stereolithograhy (μSL) has been developed to produce high precision, 3D MEMS devices [6]. In the process, a 3D solid model designed with CAD software is numerically sliced into a series of 2D layers with an equal thickness [7]. The code generated from each sliced 2D file is then executed to control a motorized x-y-z platform immersed in a liquid photopolymer. The liquid polymer is selectively exposed to a focused laser light, which moves in x-y directions. The polymer cures and forms a solid in the focal point only. After the first layer is formed the elevator moves downward and a new layer of polymer is solidified according to the design. This layer-by-layer micro-manufacturing enables complex internal features such as complex passageways and curved surfaces to be accurately produced. Furthermore, sub-micron resolution has been achieved through a two-photon polymerization process [8]. Not limited to polymeric microstructure, fabrication of ceramic and metal with complex shapes can be accomplished by mixing curable resin with fine powders.

Although individual devices can be created in a few hours by μSL, the serial nature of the direct writing process limits the yield rate for mass production as well as its bio-related applications. For instance, it prevents the incorporation of cells within the polymeric structures during the fabrication process and could also lead to denaturation and inactivation of biological molecules. To overcome the limitation, a parallel process has been proposed whereby each layer is fabricated simultaneously while the mask pattern is projected onto the liquid resin surface [9]. Although masks can be readily made by high-resolution printing or electron-beam lithography, a great number of masks are required for complex devices, which significantly increases the processing time and cost. To avoid the difficulties involved in the multiple mask process, the mask sets have been replaced by a dynamic mask, which is capable of modulating multiple patterns electronically, without physically changing masks for each layer. Bertsch and colleagues reported a μSL process employing a liquid crystal display (LCD) as a dynamic mask to photopolymerize an entire layer simultaneously [10]. The processing time reduced dramatically, microstructures containing more than 1000 layers could be fabricated within a few hours. Free-standing mechanical parts such as turbine and spring were demonstrated. Itoga and colleagues have also explored LCD projectors to study two-dimensional cellular behavior through the micro-patterning of non-cytoadhesive polymers onto plasma-treated glass surfaces [11].

However, the LCD technique has intrinsic drawbacks that hamper its performance. Low optical density of the refractive elements during the OFF mode hinders the contrast of the transmitted pattern. On the other hand, LCD absorbs UV light significantly higher during the ON mode. The aforementioned difficulties limit further improvement of the μSL system with the dynamic mask using the LCD technology. A new technology, Digital Micro-mirror Device™ (DMD, Texas Instruments, Dallas, TX), offers better performance in terms of optical fill factor (85% with DMD versus 64% with LCD) and light transmission (71% with DMD versus 21% with LCD). Furthermore, computer projectors, like the ones widely used for PowerPoint presentations, are commercially available for utilizing the DMD technology in image transferring.

Rather than writing a 3D microstructure by conventional scanning μSL, we developed a DMD-based μSL system for the fabrication of photosensitive polymers. In this chapter, 3D tissue engineering scaffolds were constructed using bio-compatible, acrylate-based resins. The system was able to precisely create internal architectures (i.e. pore size and shape). By changing biofactors or controlled-released particles pre-mixed in the polymerizable resin, each layer or even partial layers were made up of a variety of controlled-release microparticles, thereby creating spatially distributed environments with a micron-size resolution. In addition, the fast patterning speed made it possible to encapsulate living cells inside the scaffold walls efficiently during the fabrication process.

2.2 EXPERIMENTAL

2.2.1 DMD μSL apparatus

The micro-stereolithographic system was developed based on a commercial projector (BenQ P2120, Taiwan) coupled with a digital micro-mirror device (DMD^{TM}, Texas Instruments). A schematic layout of the projector is shown in Figure 2.1. A high-intensity bulb emits visible light, which is filtered by a rotating color wheel and homogenized by passing through a rectangular cross-sectioned light tunnel. The light is redirected by two coupler lenses and then reflected by two concave mirrors or a prism to illuminate the DMD chip. The image on the chip is captured and projected through a magnifying projection lens assembly to the screen.

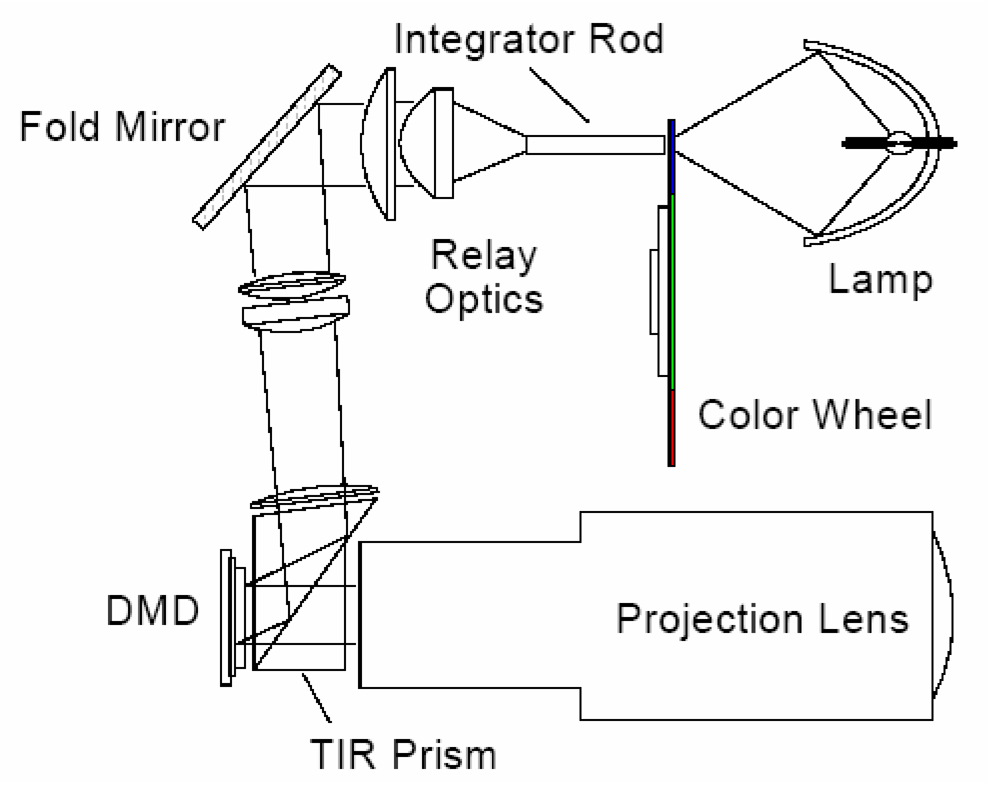

Figure 2.1. Schematic diagram of a typical DLP projector.

The projector was modified as described as follows. The light bulb, light tunnel, and the color wheel were removed. Interlock was disabled. To ensure cell viability through the use of a biocompatible UV photoinitiator, a GreenSpot UV curing system with a timer (UV Source Inc., CA) was used as the light source. The light was guided through a ¼ inch (6.35 mm) liquid-filled optical fiber. To enhance transmission in UV spectra, two fused silica plano-convex lenses (25 mm diameter, 25 mm focal length) with 5 mm spacing were used to converge the light emanating from the fiber optics. A UV fixed focal length lens (focal length = 25 mm, F2.8 – 16, spectral range 230 – 1200 nm, Edmund Optics, NJ) replaced the original glass counterpart. However, due to shorter focal length, instead of magnifying the image on the DMD chip, the UV fixed focal length lens reduced it. The reduction ratio can be adjusted by moving the lens towards or away from the chip.

The working principle of the DMD chip is also detailed in Figure 2.2. The DMD chip serves as an array of reflective aluminum micro-mirrors, which can be tilted with two bias electrodes to form angles of either +10° or - 10° with respect to the surface. Illumination from the light source reflects into the projection lens only when the micro-mirror is in its +10° state. In the -10° state, the pixel appears dark because the illuminated light is not reflected into the projection lens. The reflected light from the -10° micro-mirror is collected by a light absorber. When the micro-mirror is in +10° state, it is classified as "tilt on" or ON. Conversely, when the micro-mirror is in -10° state, it is classified as "tilt off" or OFF.

Similar to a conventional stereolithography process, the DMD μSL creates 3D microstructures in a layer-by-layer fashion. The shapes of the constructed layers are determined by slicing the desired 3D scaffold design into a series of evenly spaced planes. Patterns of each layer are drawn in a series of PowerPoint slides, which were then executed on the DMD chip to generate a dynamic mask. The illumination light is modulated according to the defined mask on the DMD chip and then goes through a reduction-projection lens assembly to form an image on the surface of the resin or macromer solution. The illuminated area is solidified simultaneously under one exposure, while the dark regions remain in the liquid phase. After one layer is patterned, the substrate is lowered and the as-patterned layer is then covered by fresh macromer solution. Microstructures with complex geometries are created by sequentially polymerizing the layers.

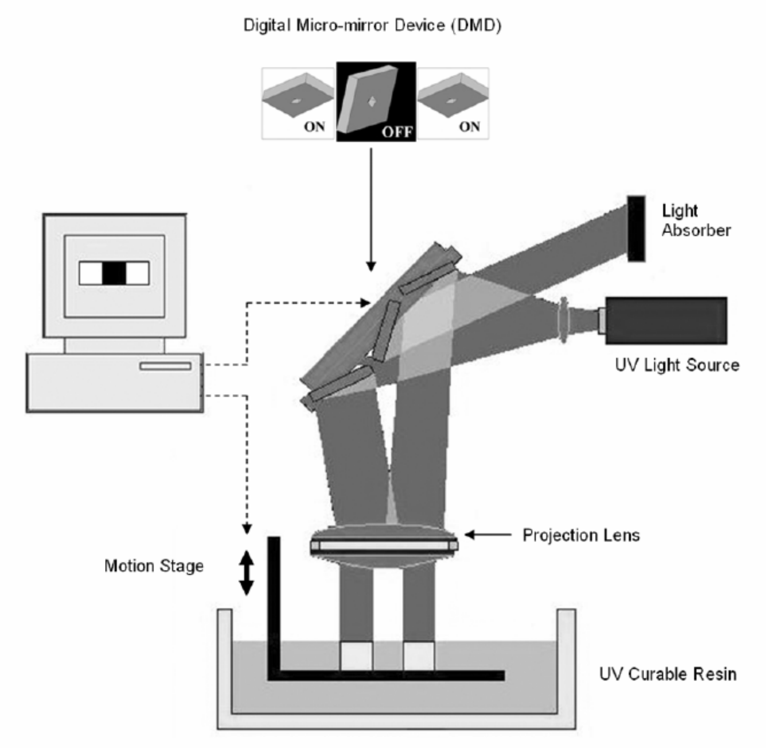

Figure 2.2. Schematic diagram of the DMD μSL apparatus.

2.2.2 Materials and preparation

Hydrogels are polymers crosslinked via chemical bonds, ionic interactions, hydrogen bonds, hydrophobic interactions, or physical bonds [12]. These materials absorb water and swell readily without dissolving. Hydrogels can chemically or physically hold the cells to provide stability, structural support, or immunoisolation. Both synthetic and naturally derived hydrogels are being investigated for cell immobilization in medicine and biotechnology.

Hydrogels produced from polymerization of multifunctional monomers, especially photopolymerizations, provide excellent materials for biomedical applications in which thermally stable, mechanically strong, solvent resistant materials are required. Poly(ethylene glycol) (PEG) diacrylates and PEG dimethacrylates were used in this research. Often when strength and durability are major requirements for certain tissue engineering scaffolds, diamethacrylates are used. Though they polymerize more slowly, the highly crosslinked methacrylates form a stronger polymer with a higher glass transition temperature when compared to their multiacrylate counterparts. This feature makes them particularly useful for applications such as dental materials in which mechanical strength and durability are primary concerns [13].

Poly(ethylene glycol) diacrylate (PEGDA, Mw 3400) and poly(ethylene glycol) dimethylacrylate (PEGDMA, Mw 1000) were obtained from Polysciences Inc.. They were dissolved in phosphate-buffered saline (PBS) to form 10-100% (w/v) solutions. The photoinitiator, 2-hydroxy-1-[4(hydroxyethoxy)phenyl]-2-methyl-1-propanone (Irgacure 2959, Ciba Geigy, USA), was used to generate free radicals for the induction of chain polymerization, with a concentration from 0.1 to 3 wt%. Prepared polymer solutions were kept in a dark environment to inhibit the pre-crosslinking of the polymer by incidental exposure to ambient light. In this work, PEG(3400)DA was used in cell experiments owing to its fast curing rate. However, it was cost prohibitive to use PEG(3400)DA in system characterization, in which large quantity was needed. Instead, PEG(1000)DMA, which had similar properties as its counterpart, was cost advantageous.

In order to fabricate multilayer/multicomponent scaffolds, precise registration is crucial. However, we found that PEG scaffolds did not securely adhere to the glass coverslips. A stronger bonding between the scaffolds and the glass coverslips was achieved through surface modification. The Surface of glass coverslips was modified with an organosilane to covalently bond the hydrogel upon polymerization, thereby promoting a strong adhesion with the hydrogels when rinsed with PBS or placed in buffered solutions/cell medium [14]. Surface-tethered methacrylate groups, which covalently attach to the acrylate groups of PEGDMA upon photopolymerization, were created on the surface of glass coverslip by first immersing the slides in a solution of 3:1

ratio of 30% (w/v) H_2O_2 in distilled water and H_2SO_4. The hydroxylated slides were then immersed in 1mM solution of 3-(trichlorosily)propyl methacrylate in a 4:1 solution of heptane and carbon tetrachloride. All chemicals were purchased from Sigma-Aldrich, unless otherwise noted.

2.2.3 System Characterization

Imaging system: The object distance and image distance were measured. Magnification of the optical system was determined by exposing a square pattern (3 x 3 mm) to a thin layer of photoresist (SU-8). The size of the resist pattern was measured and compared to that of the image in the PowerPoint file.

Intensity-gray scale relation: A DMD equipped projector can display images with various brightness and contrast. The unique capability of representing a gray scale is probably the most essential merit of the device. DMD chip's micromirrors are mounted on tiny hinges that enable them to tilt either toward the light source in the projection lens (ON) or away from it (OFF), creating a light or dark pixel on the projection surface. The bit-streamed image code entering the semiconductor directs each mirror to switch on and off up to 10,000 Hz. When the mirror is switched on more frequently than off, it reflects a light gray pixel; a mirror that is switched off more frequently reflects a darker gray pixel. In this way, the mirrors in a DMD system can reflect pixels in up to 1,024 shades of gray to convert the video or graphic signal entering the DMD chip into a highly detailed grayscale image.

Since the light intensity may not vary linearly with respect to the gray scale, it is necessary to calibrate the correlation. A test pattern (circle, ½ inch diameter) in the middle of the screen was measured at a gray scale ranging from 100% (brightest) to 0% (darkest).

Intensity distribution: A photopolymerization process is highly sensitive to the light intensity. To ensure a uniform illumination, we used a series of lens, mirrors, and holographic homogenizers to re-shape the illumination light from the fiber optics. Further compensation was done by adjusting the local gray scale. To do so, an intensity map must be plotted. A small rectangle was drawn in the PowerPoint in a size such that the energy corresponding to the pattern can be reliably measured by the energy meter. In this experiment, a 0.2 x 0.2 inch (in PowerPoint) rectangular pattern was used, which transferred to a 170 x 170 μm image. The rectangular pattern was moved in an increment of 170 μm in X and Y axis until the entire screen was covered. In the meanwhile, energy measurement was recorded after each incremental movement. Additionally, the energy sensor moved with the image, ensuring the energy was measured by the same area on the sensor every time. Finally, an intensity map was plotted based on the energy and coordinates (the energy was projected onto the intensity map with respect to the coordinates). With the intensity map, the gray scale of each unit rectangle was adjusted using gray scale/intensity correlation to achieve uniform intensity distribution across entire screen.

Optical resolution: In many tissue engineering applications, the critical dimension (CD) of patterns in a scaffold is in the same order or even smaller than the size of a cell, which ranges from a few microns to hundreds of microns.

To measure the optical resolution of the DMD system, a CCD camera was mounted on the focal plane. A series of bars with gradually decreased spacing were projected onto the CCD. The minimum spacing appreciable was recorded as the optical resolution.

2.2.4 Gelation Time

Right after photoinitiation, propagation proceeds by addition of one monomer molecule to another or by intramolecular crosslinking (cyclization reaction). Macroscopically, the resin becomes more and more viscous because large molecules move slower than small ones. The resin remains its fluidic characters until the onset of gelation. As the large polymer chains become entangled or crosslinked in the network, center-of-mass mobility is dramatically suppressed and a gel is formed.

A tissue engineering scaffold not only allows cell attachment and migration, but also exerts certain mechanical influences to modify the behavior of cell phase or, in some cases, provides temporary mechanical support before the tissue is properly formed. On the other hand, when cells are encapsulated in the scaffold during the fabrication process, it is important to minimize exposing cells to harsh fabrication environment. Therefore, it is necessary to determine how fast the resin forms a gel that possesses suitable structural rigidity. A complex reaction mechanism often hinders theoretical calculation of the gelation point and hence a design of experiment was performed.

Three concentrations of monomer, 30%, 50%, and 100% (w/v), were carefully chosen. We believe that if the monomer concentration is too high (>100% (w/v)) mesh size of the crosslinked network will be too small for efficient diffusion of biomolecule-loaded particles. On the other hand, if the monomer concentration is too low (<30% (w/v)) the resulting scaffold may lack of mechanical strength required for certain applications such as bone and cartilage.

Concentrations of photoinitiator were 0.1%, 1%, and 3%. Thus a total of nine resin specimens were prepared. Irgacure 2959 has shown low cytotoxicy at concentration lower than 0.1%. A higher concentration of photoinitiator may be used when cells are not encapsulated *in situ*. It is intuitive that the higher concentration of photoiniator, the faster the polymerization reaction is. However, due to complex autoacceleration phenomena and gel effect, higher concentration of photointiator does not necessarily render faster gel formation.

In this experiment, each resin specimen was exposed to a square pattern (3 x 3 mm). The minimum exposure time required to form a complete square-shaped gel was recorded.

2.2.5 Lateral resolution and curing depth in gels

A fine optical pattern does not always transfer into a gel pattern due to refraction, scattering, or diffusion effects. Fidelity of the transfer can be studied by patterning closely spaced bars onto a thin film of resin.

Plasma cleaning rendered highly hydrophilic surface on a glass coverslide. Drops of resin were applied on the coverslide and spread into a thin film. The best resolution was recorded under various exposure conditions.

The vertical resolution is solely determined by the depth of penetration of the light. Considering a system consisting of light absorbing, photobleaching species such as photoinitiator, light penetration follows time-revolved Beer-Lambert's law [15]. A curing depth measurement apparatus is shown in Figure 2.3. A vat containing resin was mounted on a Z-motion stage. 200 µL solution was added to the vat, which was then covered by a glass coverslide with 3-(trichlorosily)propyl methacrylate treated side in contact with resin, leaving no air bubble in between. A 3 x 3 mm square pattern was projected onto the interface between the substrate and the resin. Since the resin was an absorbing and photobleaching medium, a higher fluence penetrated deeper at that point. Consequently, the solidification of the resin was deeper at that point. The best curing depth was recorded under various exposure conditions.

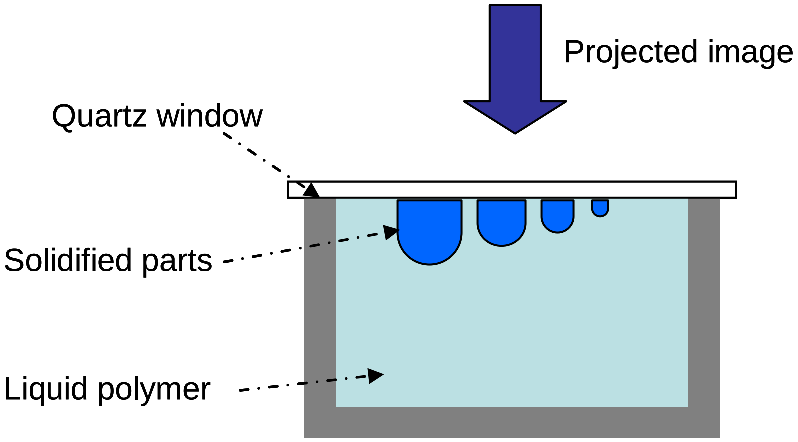

Figure 2.3. Schematic diagram of curing depth measurement. The solidified part on the left receives higher photon flux.

2.2.6 Mechanical properties of gels

The basic function of a tissue engineering scaffold is to provide structural support for the cells to attach, grow, and differentiate. Mechanical properties of tissue engineering scaffolds have been observed to affect cell migration and contractile behavior [16]. Elastic modulus of native articular cartilage is ~ 4 MPa, while the cortical bone has an average modulus value of 18600 MPa [17, 18]. If the 3-D scaffold is used as a temporary load-bearing device, the mechanical properties would maintain that load for the required time without showing symptoms of fatigue or failure.

We performed unconfined compression test to examine the mechanical strength of the scaffolds. Square-shaped gel samples were soaked in phosphate buffered saline (PBS) overnight to allow for hydration and swelling. Samples were taken out of the PBS and dimensions were measured before being placed between two compression plates of an Instron tension-compression tester. Dynamic stiffness properties were determined by applying unconfined compression between 0% and maximum strain obtainable before cracking. Cyclic compression was not performed because scaffolds lose water content upon compression.

2.2.7 Effect of oxygen

Atmospheric oxygen exerts a detrimental effect on photopolymerization. It quenches excited triplet states of photoinitiators reducing the quantum yields of the initiating radicals. In addition, oxygen reacts with carbon-based polymerizing radicals at the diffusion-controlled limit to form peroxy radicals that are much less reactive towards double bonds, thereby reducing the efficiency of initiation. This generally leads to significant retardation (or even inhibition) of the polymerization [13].

We removed oxygen in the resin by purging with dry nitrogen for 1 hour. The volume of the resin was measured after purging. Water was added to recover the initial concentration. Nitrogen was also guided to form a blanket over the surface of the resin during the reaction. The flow rate of the nitrogen was measured by a balloon. The gelation time and mechanical strength were compared between samples that contains oxygen and were absent of oxygen.

2.2.8 Post-effect

Photopolymerization of multifunctional monomers exhibits a marked postcuring effect. After the irradiation has been interrupted, the photoinduced reaction continues to proceed over a time scale of seconds, minutes or even hours [19]. A significant conversion in the dark is a prerequisite for the drying of printing inks and curing of protective coatings for optical fibers, where the polymerization is only started by light exposure and then undergoes a completion in the dark.

A qualitative investigation on postcuring was performed. Resin samples were exposed for time periods of 80 - 95% of the corresponding gelation time, with and without nitrogen protection. Size and thickness of the resulting gel were compared to its fully exposed counterpart.

2.2.9 Fabrication of tissue engineering scaffolds

The DMD μSL apparatus shown in Figure 2.2 was used to fabricate tissue engineering scaffolds. The resin container was slightly modified to eliminate "bottoming effect" (formation of a thin layer of gel at the bottom of the resin). A small inlet was made in the bottom of the plastic container (10 mm in diameter). A high-precision syringe pump fed resin into the container via the inlet. Each injection raised the fluid level equivalent to the layer thickness. Microstructures with complex geometries were created by sequentially polymerizing the layers. To fabricate scaffolds with multiple material compositions, solidified areas were rinsed thoroughly before immersing with a different monomer composition.

To demonstrate the ability of this system to create spatially-patterned, multi-layered scaffolds, fluorescently-labeled polystyrene microparticles (1.0 μm Cy5-labeled and 1.0 μm FITC-labeled, Molecular Probes, Eugene, OR) were added separately to PEGDA solutions at a final concentration of 0.03 wt% prior to irradiation.

Cell encapsulation was demonstrated using OP-9 cells. The PEGDA resin was filter sterilized and added to the cell pellet at a concentration of 5 x 106 cells/mL monomer. A 15 μL suspension of cell-monomer solution was then pattern-polymerized using DMD μSL for ~3 minutes. The unpolymerized resin was rinsed away extensively with sterile PBS, and scaffolds were transferred into tissue culture plates with medium and placed into an incubator. Scaffolds were observed using fluorescence microscopy, and images were captured. Detailed procedure was elucidated elsewhere.

2.2.10 Characterization of tissue engineering scaffolds

Resulting constructs were analyzed using either a confocal microscope for fluorescence patterning (Leica SP2 AOBS) or scanning electron microscopy (Phillips 515 SEM) for multi-layered scaffolds.

2.3 Discussion

The DMD μSL system has gone through numerous modifications since the first version was built. The intention of these modifications was to improve the optical resolution, illumination intensity, and uniformity.

Before an appropriate imaging lens was chosen, we studied extensively how the DMD system works. UV light exited the liquid-filled fiber optics and formed an illumination cone with an angle of 30°. Light was condensed through a condensing doublet and two concave mirrors before illuminating the DMD. As illustrated in the context, each micromirror was tilted + or - 10°, towards the imaging lens or light absorber, respectively. It was critical to properly adjust the position of the fiber with respect to the condensing doublet so that the diverging angle of imaging and waste beam was less than 10°. This was to avoid overlapping of these two beams.

Large aperture imaging lens was desired because of its fine resolution and energy efficiency. Spatial constraints of the projector compromised the use of lenses with diameter larger than 30 mm. Furthermore, there was a trade-off between numerical aperture and working distance. Both resolution and illumination intensity could benefit from having a large numerical aperture. On the other hand, a working distance greater than 10 mm was necessary for sample loading/unloading. Finally, a UV fixed focal length lens was installed (Table 2.1).

Table 2.1. Specification of the UV fixed focal length lens

Focal Length	25 mm
Aperture f/# (C = closed)	F 2.8 – 16 C
Angular FOV*	14.0 °
FOV* at Min. Working Dist.	58.9 mm
Minimum Working Distance	0.23 m
Spectral Range	230 nm – 1200 nm
Dimensions	30.0 mm Dia x 25.4 mm L

This imaging lens was not chromatically corrected. Coupled with a broadband UV light source, it induced a discrepancy in focal length at various wavelengths. The premise is supported by the refractive index chart in Figure 2.4. We usually rely on CCD camera or human eyes to find the focal plane. Camera and eyes are sensitive to wavelength greater than 400 nm, while the peak absorption of Irgacure 2959 was around 270 nm. The refractive index of BK7, which is used as lens material, is ~ 1.57 at 270 nm and is ~ 1.53 at 400 nm. Without detailed specifications of the lens, it was difficult to calculate the discrepancy of the focal length. We experimentally determined the focal plane at which the best resolution was obtained. The focal plane for Irgacure 2959 turned out to be 4 mm closer to the imaging lens than the focal plane obtained using a CCD camera.

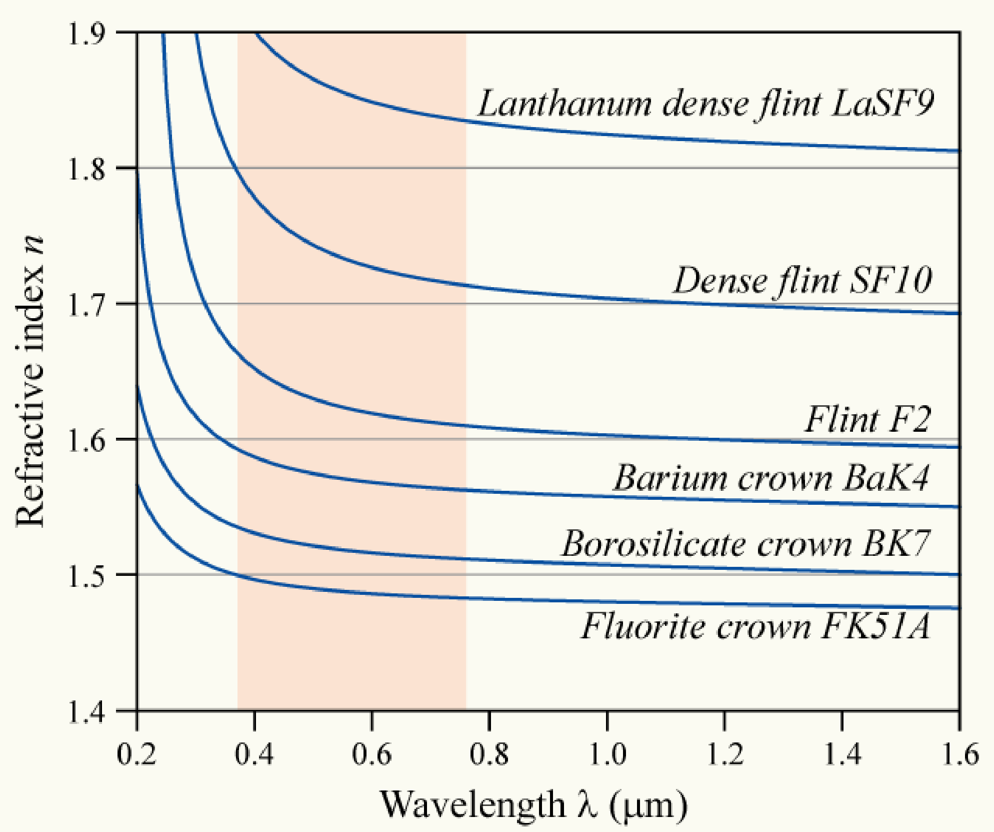

Figure 2.4. The variation of refractive index vs. wavelength for various glasses. (from http://en.wikipedia.org/wiki/Dispersion optics)

The image distance and object distance (the distance between the DMD chip and the top edge of the lens) were measured to be 38 mm and 37 mm, respectively. The ratio of the image to the actual pattern was 30/1.

Intensity vs grey scale: The relation between the intensity and grey scale is shown in Figure 2.5. It was obvious that the relation was not linear. It may be because the grey scale was set based on the sensitivity of human eyes instead of that of the energy meter. We also noticed that it was not completely dark even at 0% grey scale. The contrast must be taken into account in fabrication.

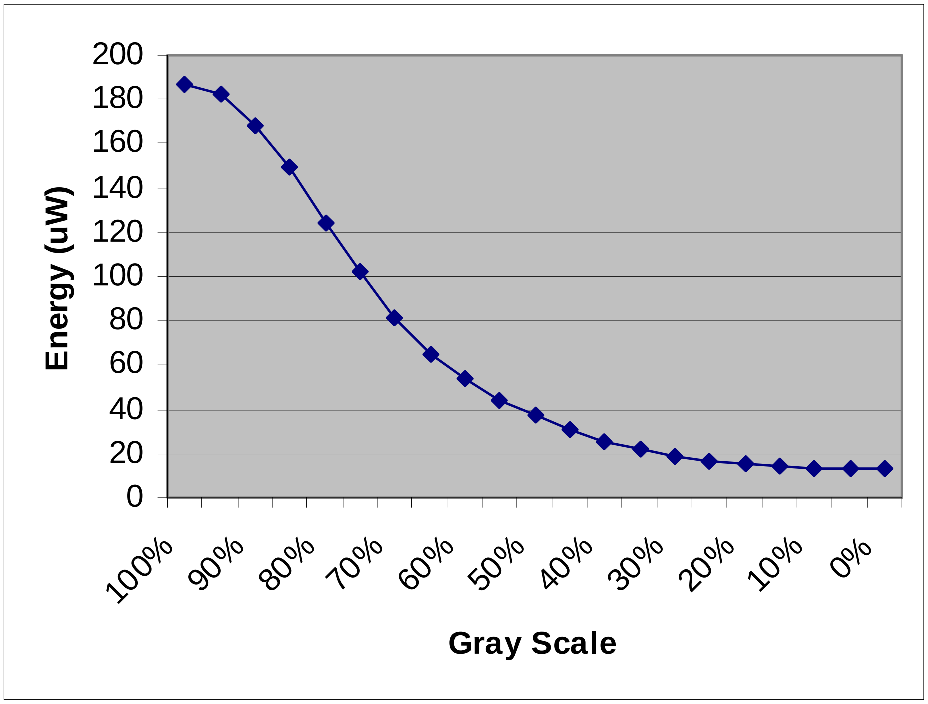

Figure 2.5. The correlation between intensity and grey scale.

Intensity distribution: The intensity distribution for the area of DMD which was used most frequently was measured. Measurement resulted in a two dimensional matrix and each element corresponded to the intensity. Figure 2.6 visualized the distribution. The standard deviation was 3.76 mW/cm^2. We believe the small variation was caused by measurement noise.

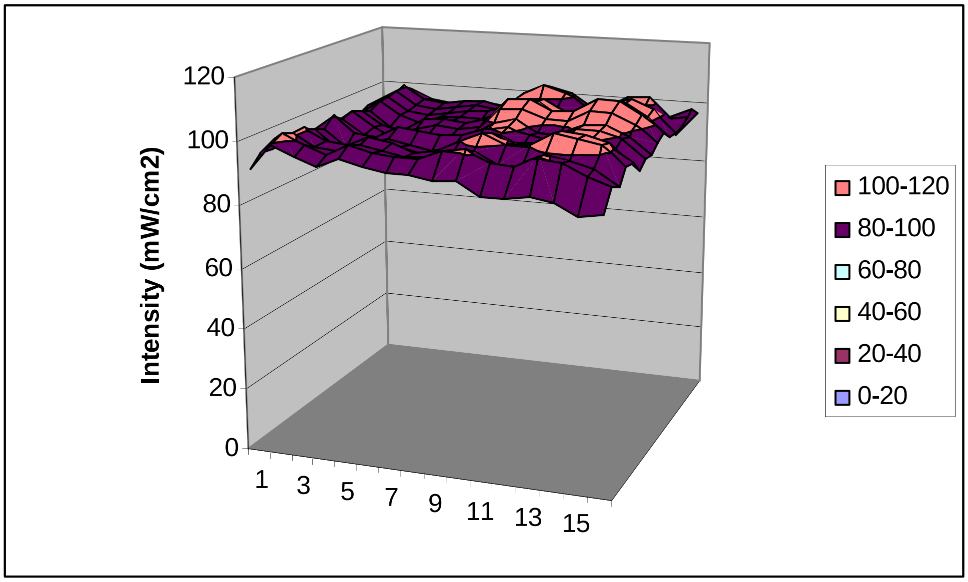

Figure 2.6. Intensity distribution of a square pattern of 3.4 x 3.4 inches in PowerPoint.

Optical resolution: An image of closely spaced bars was captured by a CCD camera placed at the focal plane (Figure 2.7). The width of each line was 85 µm on the projected image. Line spacing decreased towards the top of the image. The minimum spacing observed was 17 µm.

Contrast transfer function (CTF) can be used to determine the limiting resolution.

$$Contrast = \frac{C_{\max} - C_{\min}}{C_{\max} + C_{\min}} \tag{2.1}$$

where C_{max} is the normalized value of the maximum (for example, the voltage or grey value of the white area) and C_{min} is the normalized value of the minimum (for example, the voltage or grey value of the black area).

Excessive noise can be seen in the image because the CCD was not designed for the UV light. High energy photons caused hot spot on the CCD. That made it difficult to apply CTF to evaluate the resolution. We believe the limiting resolution could be even higher than the observed value of 17 µm.

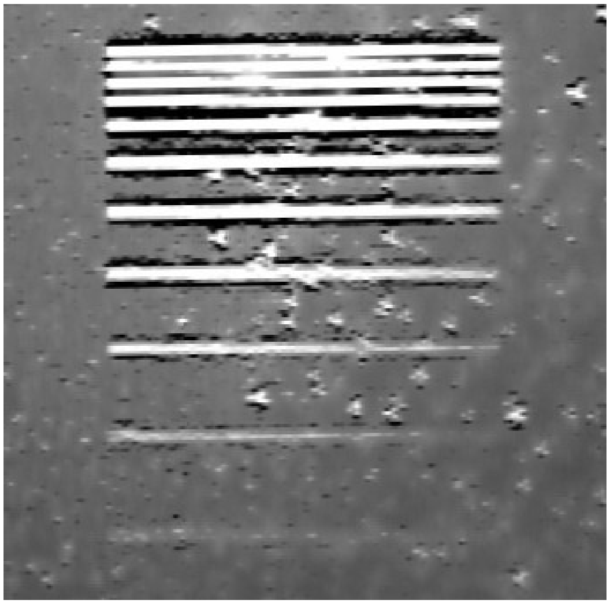

Figure 2.7. Image of the testing chart that consists a series of closely spaced bars.

Gelation times for specimens at maximum exposure intensity (100% grey scale) are compared in Figure 2.8. The exposure intensity was 417 mW/cm^2. It is safe to conclude that within the designed experimental condition increase of photoinitiator concentration accelerated gel formation. This was true for both with and without nitrogen protection. More photoinitiator molecules generated more radicals, which consequently increased the rate of network forming. Furthermore, higher photoinitiator concentration counterbalanced radical scavenging caused by oxygen. We expect that the effect of photoinitiator concentration on gelation time will reach a maximum and follow by a possible inversed trend. This is because at high concentration, one primary radical is quickly terminated by another. The observed gelation time was almost the same in resin containing 3% and 1% photoinitiator when oxygen was removed, whereas the gelation time was up to 3.75 times longer in resin containing 1% photoinitiator than one with 3% when oxygen was not removed. Similar results were obtained for exposure intensity at 80% grey scale (278 mW/cm^2) as shown in Figure 2.9. With oxygen present, it took longer than one hour to induce gel formation (except for 100% PEGDMA, 3% Irgacure 2959) at intensity at 60% grey scale. We only recorded results for trials with nitrogen protection (Figure 2.10).

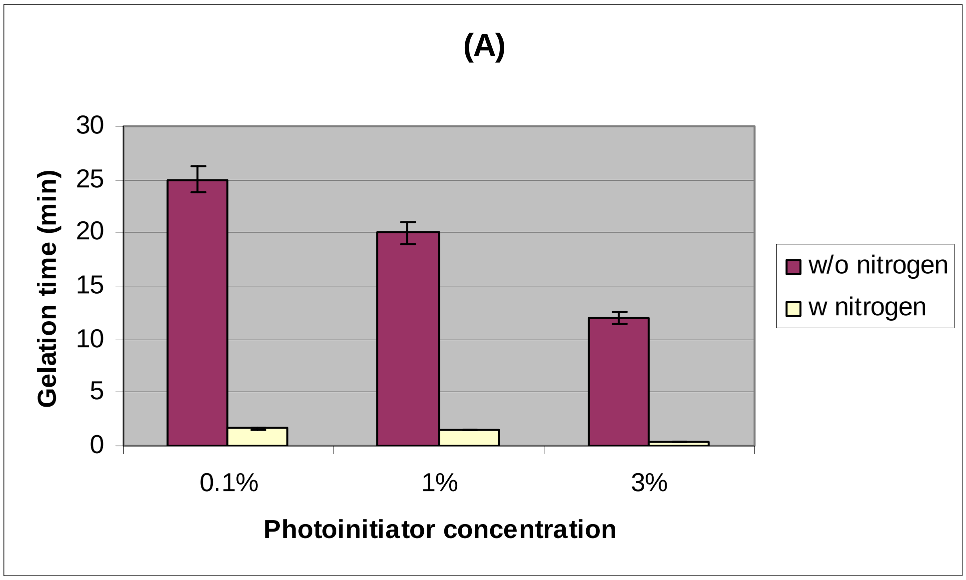

Figure 2.8 (A). Gelation time for resin containing 30% (w/v) PEG(1000)DMA with/without nitrogen protection at 100% grey scale.

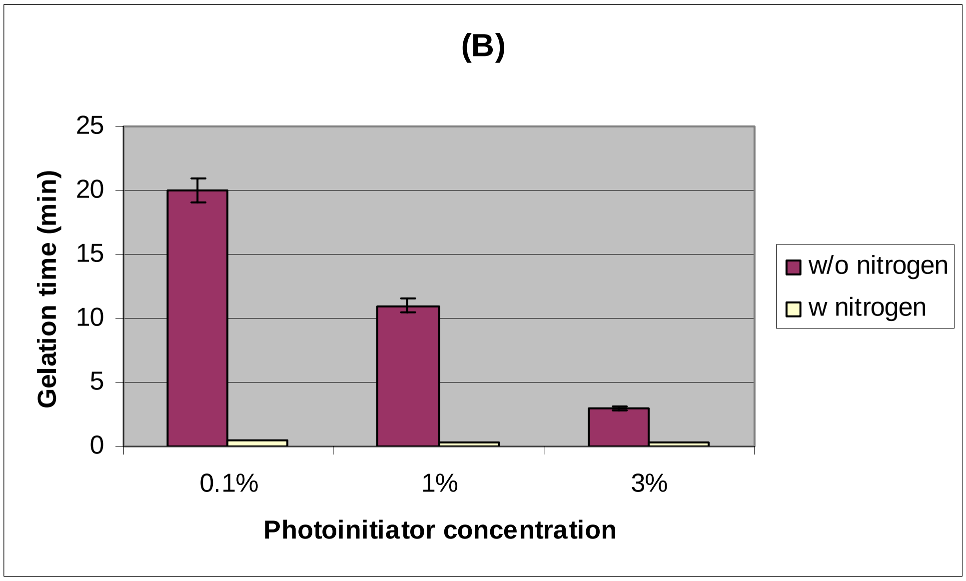

Figure 2.8 (B). Gelation time for resin containing 50% (w/v) PEG(1000)DMA with/without nitrogen protection at 100% grey scale.

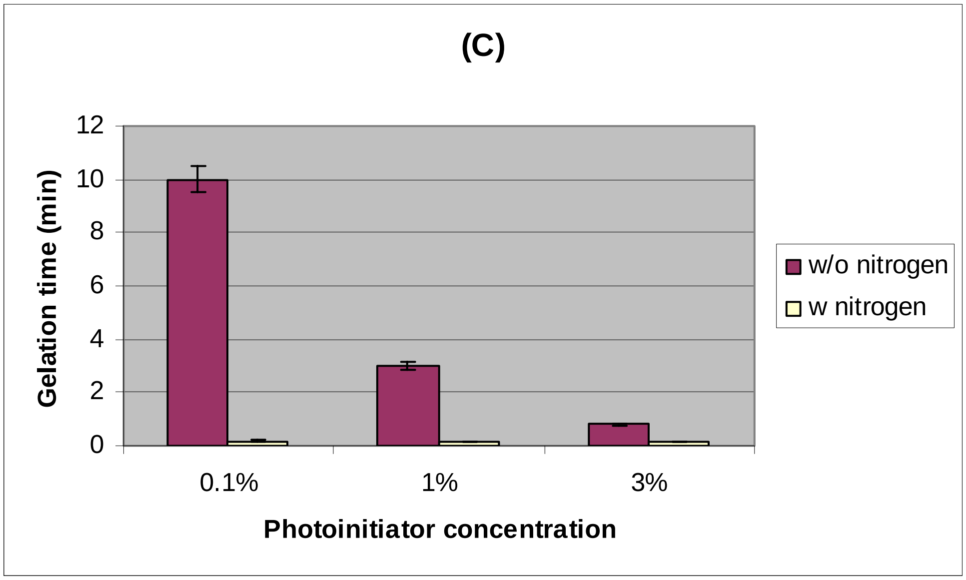

Figure 2.8 (C). Gelation time for resin containing 100% (w/v) PEG(1000)DMA with/without nitrogen protection at 100% grey scale.

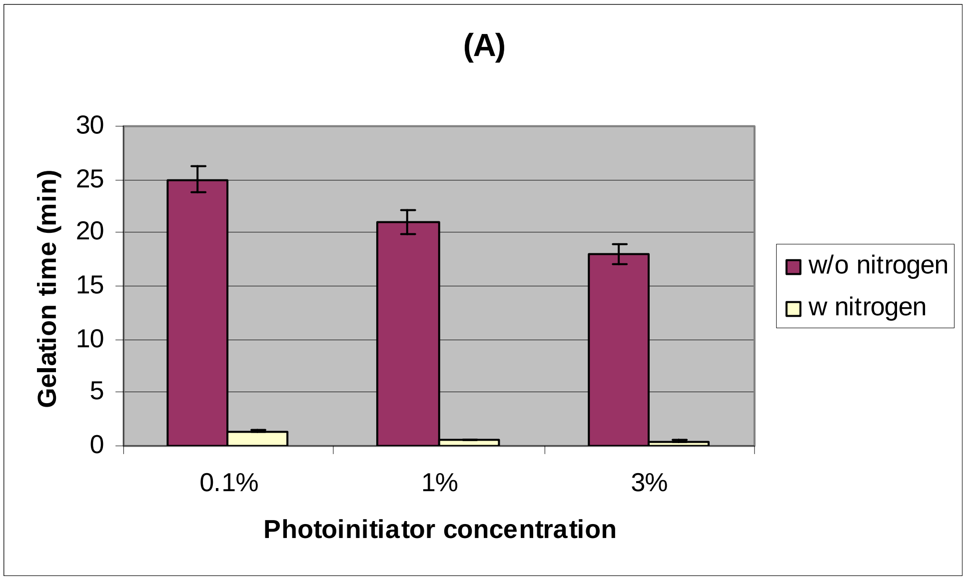

Figure 2.9 (A). Gelation time for resin containing 30% (w/v) PEG(1000)DMA with/without nitrogen protection at 80% grey scale.

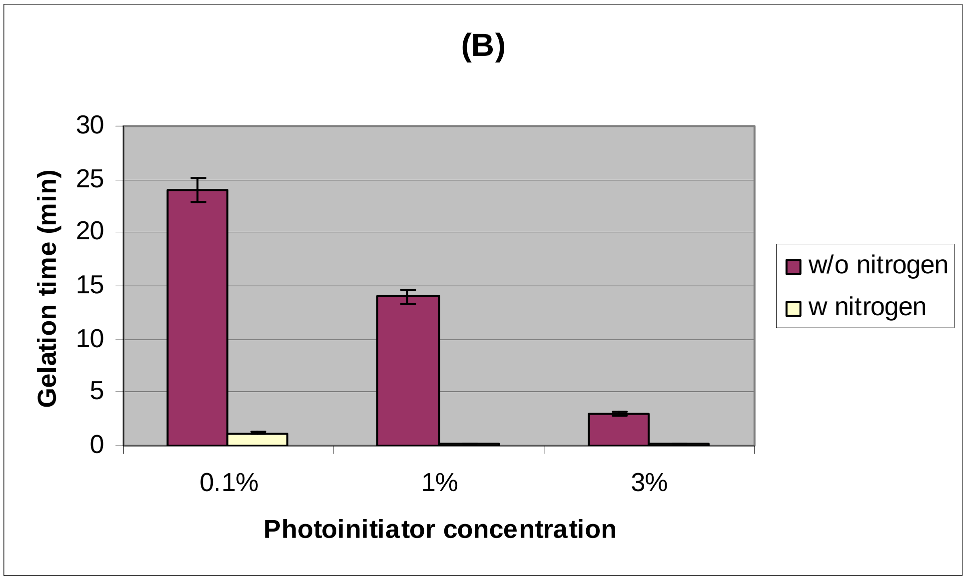

Figure 2.9 (B). Gelation time for resin containing 50% (w/v) PEG(1000)DMA with/without nitrogen protection at 80% grey scale.

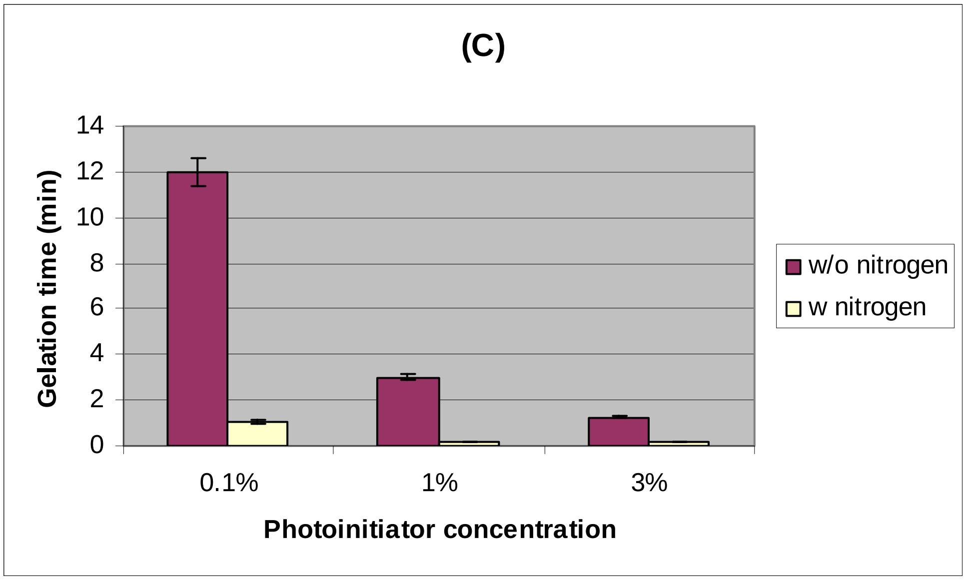

Figure 2.9 (C). Gelation time for resin containing 100% (w/v) PEG(1000)DMA with/without nitrogen protection at 80% grey scale.

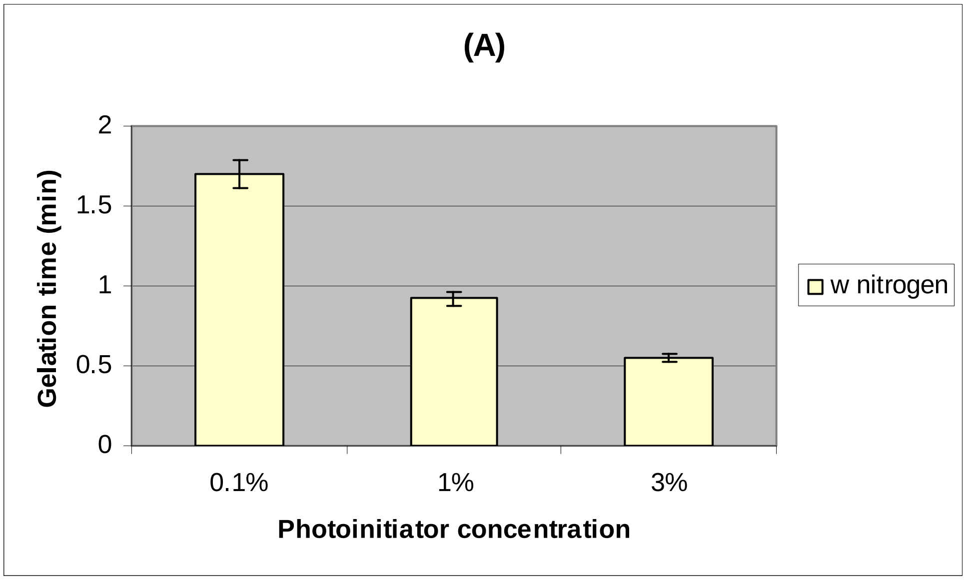

Figure 2.10 (A). Gelation time for resin containing 30% (w/v) PEG(1000)DMA with nitrogen protection at 60% grey scale.

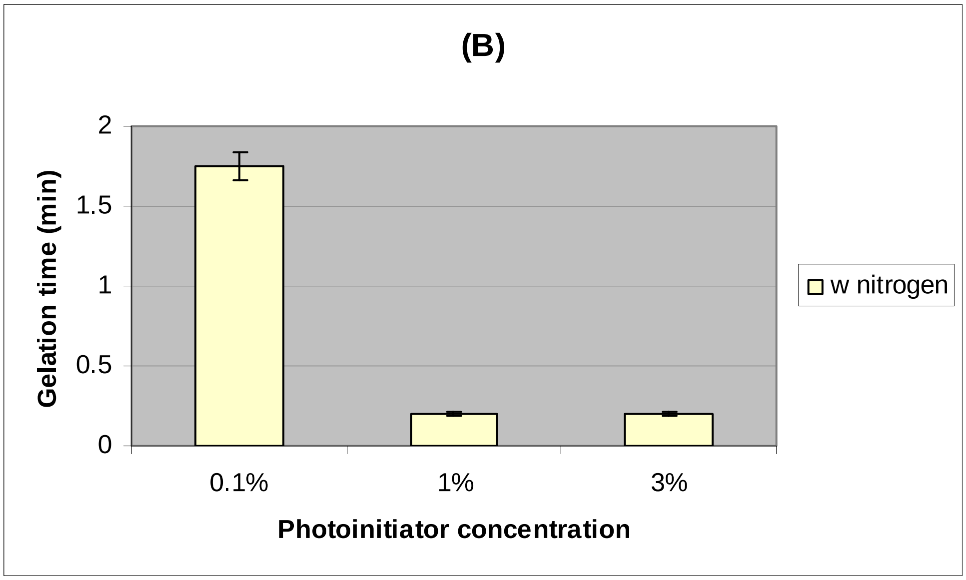

Figure 2.10 (B). Gelation time for resin containing 50% (w/v) PEG(1000)DMA with nitrogen protection at 60% grey scale.

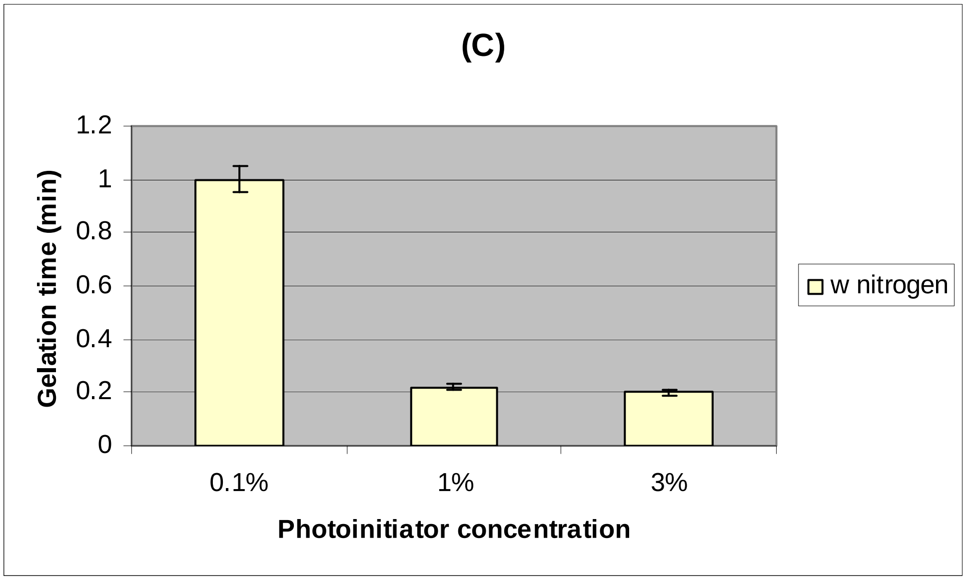

Figure 2.10 (C). Gelation time for resin containing 100% (w/v) PEG(1000)DMA with nitrogen protection at 60% grey scale.

Curing resolution: Both physical and chemical effects deteriorated the critical dimension. The best achievable resolution was recorded from a series of bars with 40 μm pitch and 50% duty cycle. As the width of bars further reduced, thin film started to form in between the bars and finally the spacing became unappreciable.

We attributed the limited resolution to several factors. Firstly, Fresnel reflection occurred at the first and second air-glass interface. The reflectivity can be calculated by Fresnel equations.

$$R_s = \left[\frac{\sin(\theta_t - \theta_i)}{\sin(\theta_t + \theta_i)}\right]^2 = \left[\frac{n_1\cos(\theta_i) - n_2\cos(\theta_t)}{n_1\cos(\theta_i) + n_2\cos(\theta_t)}\right]^2 \tag{2.2}$$

$$R_p = \left[\frac{\tan(\theta_t - \theta_i)}{\tan(\theta_t + \theta_i)}\right]^2 = \left[\frac{n_1\cos(\theta_t) - n_2\cos(\theta_i)}{n_1\cos(\theta_t) + n_2\cos(\theta_i)}\right]^2 \tag{2.3}$$

where subscript s and p depict two orthogonal polarization, n is the refractive indices, θ_i is the incident angle, and θ_t is the refracted angle. Assuming an unpolarized light source and near-normal incidence, which was a very close approximation in this case, the reflection coefficient could be simplified as

$$R = R_s = R_p = \left(\frac{n_1 - n_2}{n_1 + n_2}\right)^2 \tag{2.4}$$

At the first interface, 1% of incident light was reflected back to the resin (n_{water} = 1.33, n_{glass} = 1.63) and the reflection from the second interface was negligible. We believe reflection may not be a major factor.

The second limiting factor was diffusion of reactive species. In diluted resin, mobility of monomers, photoinitiators, and radicals were relatively high. Due to slow network formation, these reactive species could move in and out of irradiated zone less restricted and hence the polymerization zone spread out. In relatively concentrated resin (i.e. 100% (w/v) PEGDMA content), quick network forming and auto-acceleration effect limited segmental diffusion. Primary radicals were readily consumed by high concentration monomer. Both effects limited diffusion of reactive species and consequently improved resolution. On the other hand, reaction-diffusion dominated propagation in resin with high concentration monomer [20]. The propagation of macroradicals at the boundary of irradiated zone could move the gel boundary further to the dark zone, especially when the resin was free of radical quencher.

Thirdly, gel deformation due to stress build-up may also cause blurring of the geometry.

Without comprehensive understanding of the complex interplay of these factors, we had to rely on experiment to find out the optimum condition.

The light penetration depth was the major factor that determined the depth of curing. Reducing the intensity limited the penetrated depth. However, if the intensity was lower than a certain threshold, it could not initiate enough radical to form a network. Within the experimental condition, the best curing depth was 0.4 mm when the grey scale was at 60% (Figure 2.11). Lower the intensity or reduce the exposure time may result in a shallower curing depth, but the stiffness of the gel formed was not acceptable for tissue scaffold applications.

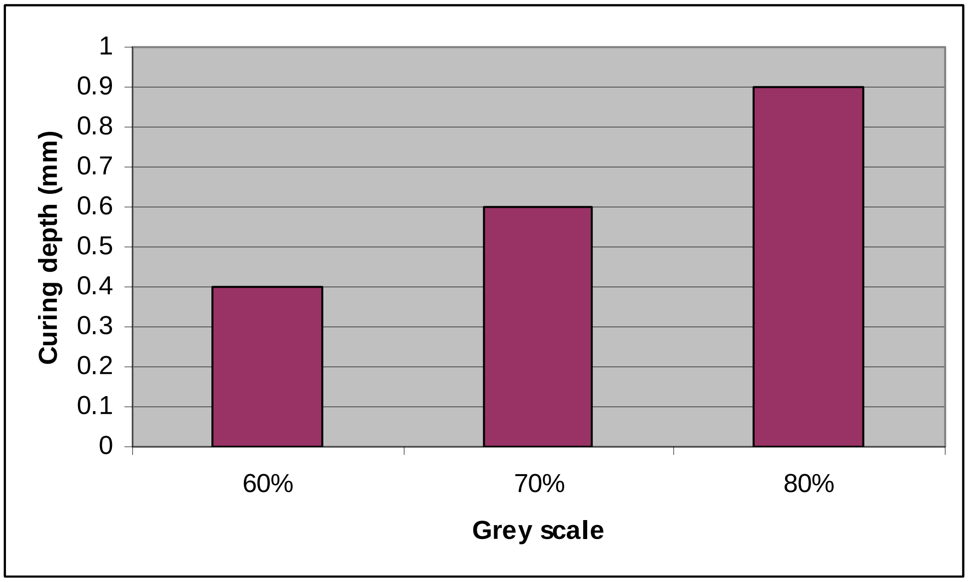

Figure 2.11. The depth of curing vs intensity. The resin contained 100% (w/v) PEGDMA and 0.1% photoinitiator. Exposure time was 1 minute. Thickness of the gel was measured using an optical microscope.

Oxygen effect: Oxygen is evidently a strong inhibitor for photopolymerization. As a primary radical was generated, it initiated a functional group in the monomer. This reaction competed with the quenching (scavenging) of primary radicals by various additives (i.e. stabilizers) and by oxygen. The extent to which oxygen overshadows other common inhibitors was significant. That can be seen from their transfer constants towards the propagating radicals in the polymerization of styrene and of methyl methacrylate [21]. Since the rate of generation of primary radicals, at a given exposure intensity, was a function of the concentration of photoinitiator, the induction period depended on the initiator concentration. Oxygen greatly slowed down the initiation process and sometimes completely inhibited it.

The consequence of oxygen effect had two folds. First, higher exposure intensity or higher photoinitiator concentration was necessary for scaffold fabrication. Excessive UV irradiation may elevate the temperature of the resin, which may induce decomposition of bioactive molecules. On the other hand, the use of initiator exceeding a safety level (0.1% for Irgacure 2959) may cause cell death. Second, a prolonged induction period could also result in cell death.

Therefore, it was critical to minimize oxygen content in the resin and to shield oxygen from diffusing into resin during the polymerization. Also we need to be aware that cells might be vulnerable without enough oxygen.

Postcuring refers to the continuation of propagation process after irradiation is interrupted. Detailed kinetics can be studied by using specially designed analytical instruments. For example, Studer and colleagues used *in-situ* FT-IR to monitor acrylate content, which was an indicator of the reaction rate [22]. Goodner and colleagues performed kinetic experiments in a differential scanning calorimeter (DSC). The rate of polymerization was determined by monitoring the heat evolved in the exothermic reactions [23]. In our experiments, we did not observe any appreciable macroscopic change after irradiation stopped. Kinetic study using FT-IR or DSC should follow in the future.

Mechanical Properties: Mechanical strength of a hydrogel is determined by the molecular structure, molecular weight, and crosslinking density. With molecular structure and molecular weight being consistent over all the resin in the experiment, crosslinking density became the dominant factor. One would expect the crosslinking density be proportional to the concentration of the monomer, which is linearly proportional to the concentration of the functional groups. However, the auto-acceleration effect and gel effect made a much more complex scenario.

In concentrated monomer systems the properties of the medium change during polymerization. The viscosity increases as polymerization progresses and this slows down all chemical process in which two macroradicals must diffuse towards each other is more strongly affected than propagation, where one of the partner is the mobile free monomer. As a result the polymerization rate increases dramatically in the course of the process, giving rise to a strong auto-acceleration effect. The onset of auto-acceleration can start at a very early stage of polymerization. The rate of polymerization reaches a maximum and finally slows down, long before all monomer is consumed, for lack of radical mobility.

Three load-compression curves representing PEGDMA gels undergoing compression loading are shown in Figure 2.12. They were cured from resins containing 100%, 50%, and 30% (w/v) PEGDMA with 0.1% photoinitiator. Exposure was conducted at the 381 mW/cm^2 for 90 seconds. These curves each consisted of three distinctive regimes: a parabolic-like regime gradually transformed to a linear-elastic regime followed by rough plateau.

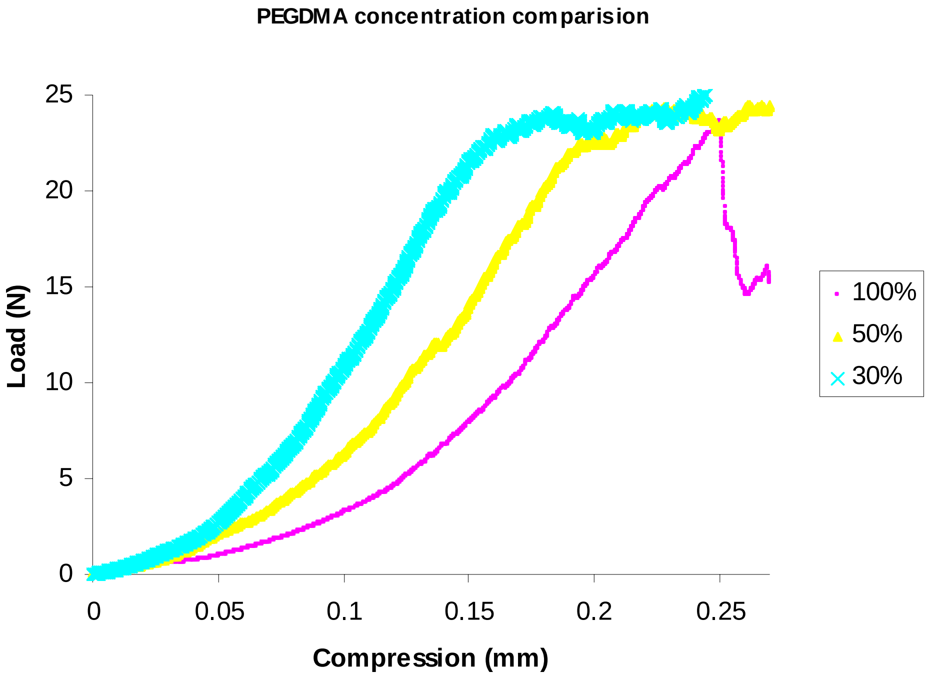

Figure 2.12. Load-compression curves for resins containing 100% (▪), 50%(▲), and 30% (**X**) (w/v) PEGDMA with 0.1% photoinitiator.

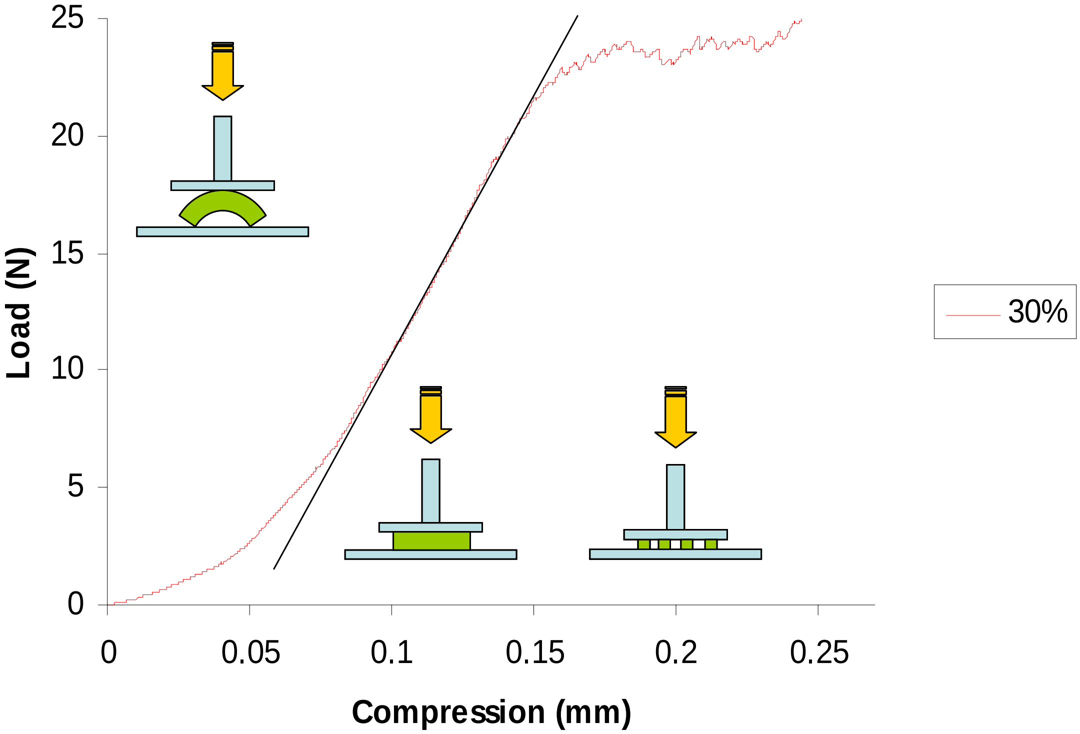

Figure 2.13. Load-compression curve for resin containing 30% (w/v) PEGDMA and 0.1% photoinitiator. Three regimes are color-coded.

We noticed that all the gel samples cambered to various extents. This was induced by polymerization shrinkage. The volume shrinkage could be partially explained by a decrease in van der Waals volume from the conversion of van der Waals bonds into covalent bonds [24]. During the polymerization, the bottom of the gel adhered to the glass substrate, while the top of the gel was in contact with the fluid. As a result, a difference in stress built up, which led to the deformation.

We can take the curve for the resin containing 30% PEGDMA as an example (Figure 2.13). At the early stage of compression, both the force component that counteracting with the camber and the component compressing the gel contributed to the total load. It appeared that the latter component outweighed the former as the contact area increased. As it required a much greater force to compress the gel than that to flatten it, the curve became linear. Finally, unconfined compression resulted in fragmentation of the gel, the curve became non-repeatable thereafter.

It was reasonable to assume that little strain was induced in the first regime so that the reduction in thickness started from the onset of the second regime. The linear portion of the stress-strain relation (shown as a straight line in Figure 2.13) was used to calculate the elastic modulus

$$E \equiv \frac{\text{tensile stress}}{\text{tensile strain}} = \frac{\sigma}{\varepsilon} = \frac{F/A_0}{\Delta L/L_0} = \frac{F L_0}{A_0 \Delta L} \tag{2.5}$$

where F is the load in N, A_0 is the area in m^2, ΔL is the deformation and L_0 is the original length along deformation, both in m.

Data in Figure 2.11 was converted to elasticity (Figure 2.14). In contradiction with our initial expectation, higher PEGDMA content did not result in stiffer structure within the conditions of our experiment. We already observed earlier onset of gelation occurred in the resin that had higher PEGDMA content. The early onset of gelation dramatically suppressed segmental or center-of-mass diffusion of macroradicals. A significant amount of macroradicals were “caged” and remained unreacted. A lower network density led to a lower elastic modulus. This counter-intuitive result has drawn attention and indicated an even more complex mechanism exists.

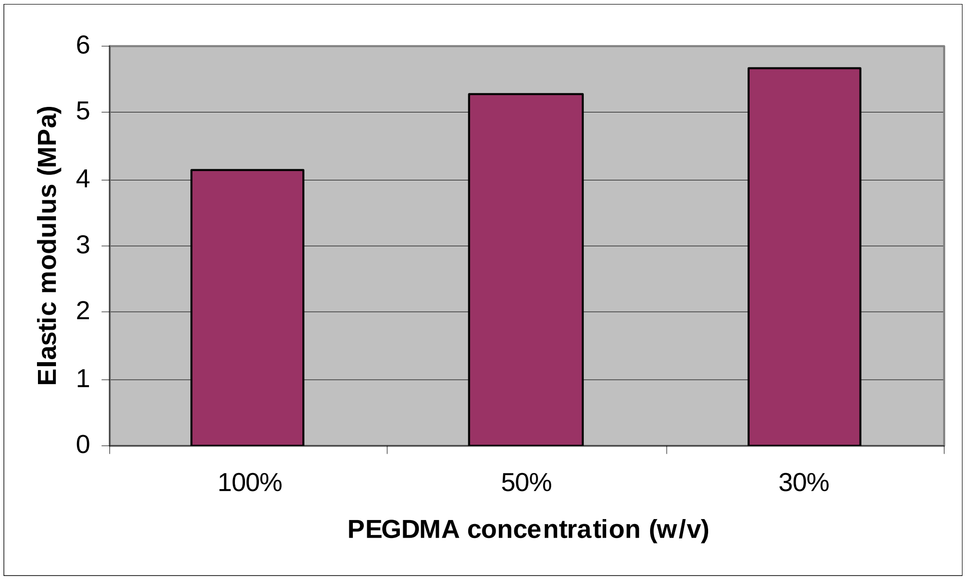

Figure 2.14. A comparison of elastic modulus vs PEGDMA content.

In addition to the concentration of monomers and photoinitiators, another major factor determining the rate of polymerization was the exposure intensity. As the quantum efficiency of the photoinitiator (the probability of a photoinitiator molecule forms a radical when it is impinged by a photon) remains constant, a higher flux of photons generated more radicals per unit time period. Consequently, the exposure intensity determines the network density and hence the elasticity of a gel. We investigated the effect of intensity based on the resin containing 100% (w/v) and 0.1 % photoinitiator as it was used most frequently throughout our experiments. Gel samples were made under 100%, 80%, 60% grey scale, corresponding to 370, 247, 107 mW/cm^2, respectively. The gel sample made under 80% grey scale shown the highest elasticity among these three samples, which indicated that a higher intensity may not always generate a stiffer structure (Figure 2.15). This result does not agree with kinetic modeling by Bowman and Peppas, which indicates that a higher polymerization rate leads to a higher final conversion [25]. A full range of experiment is necessary to draw further conclusion.

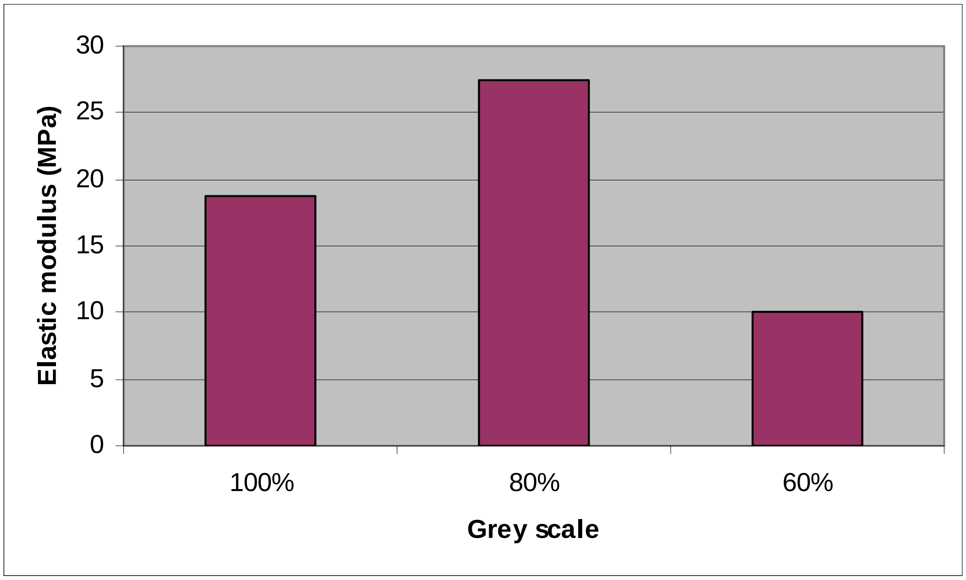

Figure 2.15. Elastic modulus vs exposure intensity.

We set the intensity constant at 80% grey scale while varying the exposure time. It appeared that longer exposure may help increasing the elasticity within our experimental condition (Figure 2.16). It may be because the photoinitiator molecules were gradually dissociated. A higher intensity exposure (i.e. a laser) may deplete photoinitiator in a relatively short time.

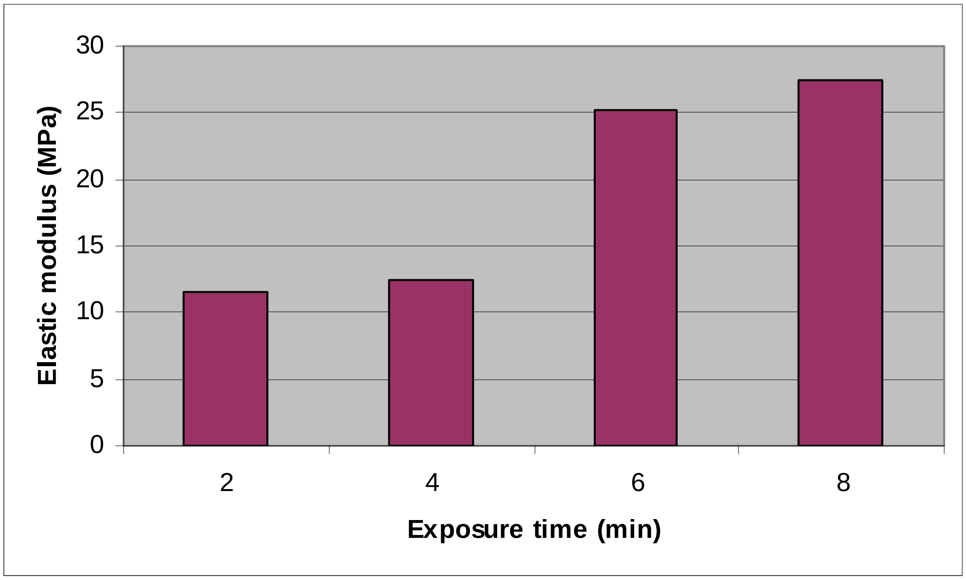

Figure 2.16. Elastic modulus vs exposure time.

Scaffold fabrication: The DMD µSL method was used to create polymer scaffolds with pores and channels having a wide variety of shapes and dimensions. The configuration of the scaffold pores was dictated simply by altering the “mask” drawn on a PowerPoint slide, thus illustrating the powerful capability of this system to design features of any shape or form. As shown in the scanning electron microscopic (SEM) micrographs of Figure 2.17 (A-D), different pore geometries (hexagons, triangles, honeycombs with triangles, and squares) can be included within a single scaffold (pore size dimensions range from ~165µm to ~650µm, scale bars shown). Precise internal features of the scaffolds were fabricated with one single 90 sec exposure to the UV light of the DMD µSL. Additionally controlled internal architectures can be generated in parallel.

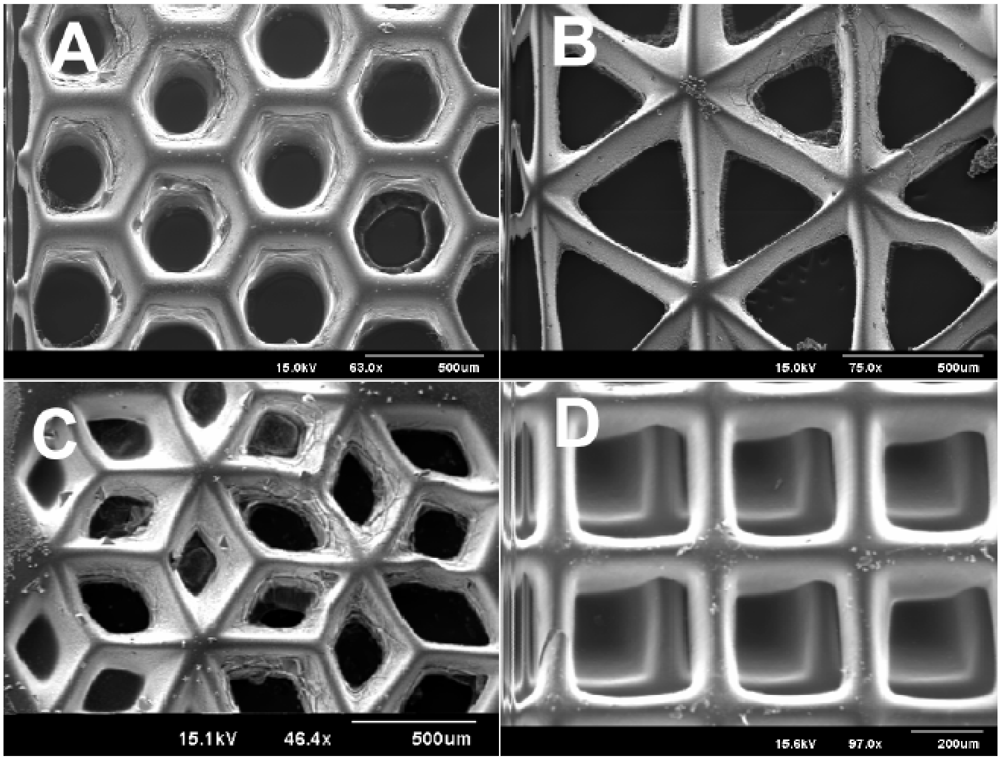

Figure 2.17. Scanning electron microscopy (SEM) illustrate that DMD-µSL can create scaffolds with intricate pore geometries. Hexagons (honeycomb), triangles, triangles inside hexagons, and squares shaped pores were created by directly drawing in PowerPoint files and using the DMD as a dynamic "mask". Scaffolds depicted in Figure D specifically show a two-layered scaffold. All scaffolds were irradiated for 90 sec per layer and formulated using 100% (w/v) PEGDA in PBS and 0.1wt% Irgacure 2959.

Figure 2.17 (D) shows scaffolds fabricated in a multilayered fashion. The pore dimensions used in this scaffold are 250µm by 250µm with a measured wall thickness of 100µm. The edges appeared to be slightly rounded, due to swelling of the hydrogel structure.

The DMD µSL system can fabricate both single layer and multi-layered scaffolds with pre-designed, spatially patterned molecules and particles. The feasibility of such precise spatial patterning was demonstrated using PEGDA solutions containing either Cy-5 or FITC-labeled polystyrene particles that were encapsulated in a pre-designed pattern during the polymerization process. As shown in Figure 2.18 (A), solutions containing different particles can be patterned in a quadrant-specific geometry, in which the solution with Cy-5 particles were polymerized in the upper left and lower right regions, and the solution with FITC particles were polymerized in the upper right and lower left regions. This Figure demonstrated the ability of the DMD μSL system to pattern multiple agents within a single layer through sequential steps of polymerization and rinsing of unpolymerized solutions. We also demonstrated spatial patterning in multi-layered scaffolds, as shown in Figure 2.18 (B and C)**,** by creating constructs that specifically consisted of two layers, each containing either Cy-5 or FITC-labeled particles. The bottom layer was pattern-polymerized with a single 90-second exposure using Cy-5 particle-polymer solution, and then rinsed extensively to remove unpolymerized polymer and particles. The second layer, containing FITC particle-polymer solution, was then polymerized in the same method on top of the first layer using the same patterning mask.

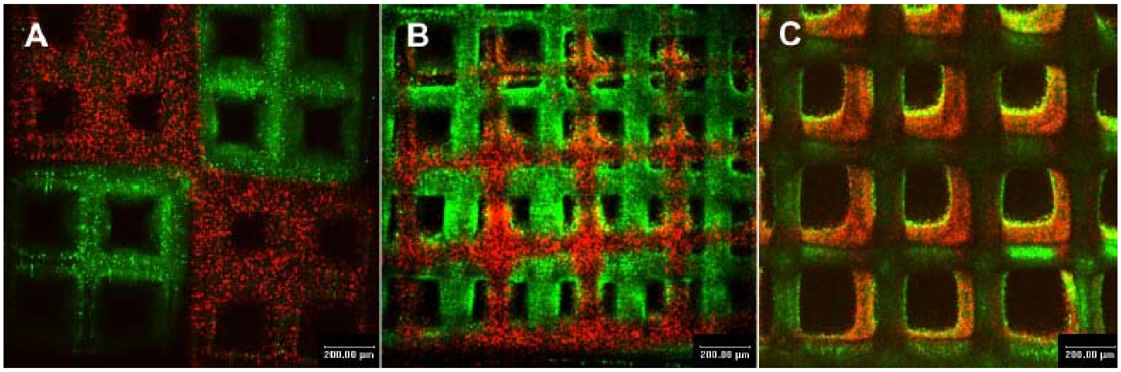

Figure 2.18. DMD-μSL can create pre-designed, spatial-patterns inside scaffold structures. Fluorescence confocal microscopy of scaffolds formulated with 100% (w/v) PEGDA in PBS, 0.1wt% Irgacure 2959, and 0.03wt% carrying either FITC- or Cy5-labeled polystyrene particles. (A) shows spatial patterning of a single-layer in a “quadrant” specific pattern. (B) and (C) show spatial patterning in multi-layered scaffolds.

Patterned encapsulation of cells within the scaffold walls was achieved by the addition of OP-9 cells to the macromer solution prior to DMD μSL UV irradiation. Figure 2.19 shows a fluorescence micrograph of cells overlaid onto a transmitted micrograph of the scaffold, and demonstrated the viability of encapsulated cells within a single-layered scaffold (~150 μm thick layer). Details of this experiment were given elsewhere.

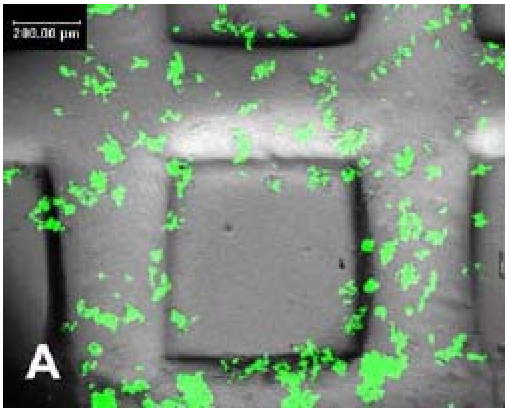

Figure 2.19. Marrow-derived stromal cells remain viable following encapsulation in DMD-μSL fabricated scaffolds. Scaffolds depicted in this Figure were formulated with 100% (w/v) PEGDA in PBS and 0.1wt% Irgacure 2959.

2.4 CONCLUSION

We have demonstrated DMD-μSL to be a powerful technology in creating pre-designed, spatially patterned scaffolds for applications in cell and tissue engineering. This novel stereolithography system has the capability of creating precise distributions of chemical and biological factors within a 3D scaffolding structure. The scaffolds are also suitable for the encapsulation of single or multiple cell types in a spatially distributed fashion. These micro-fabricated, spatially patterned scaffolds could ultimately incorporate intricate architectures that combine both spatial and controlled-release kinetics of biochemical factors, creating a suitable environment for studying hybrid tissue formation from a single stem cell population.

Our effort has been focused on understanding the system characteristics (i.e. gelation time, resolution, mechanical properties) and fabricating tissue engineering scaffolds. There are other requirements for cell immobilization and growth. For example, a tissue engineering scaffold must have proper permeability to allow sufficient diffusion and transport of oxygen and essential nutrients, metabolic waste, and secretory products across the hydrogel network. Proper design of the hydrogel network structure, pore size, and chemical composition, which affect the interaction between the diffusion species and molecular mesh, is essential. We have briefly investigated mechanical properties of the hydrogels. There are several approaches to manipulate the mechanical properties, including grafting hydrogels onto other biomaterials, semi-interpenetrating polymer network (SIPN) and linear polymer reinforcement technologies [26]. Successful immobilization by adhesion depends on cell attachment to the hydrogel substrate to preserve cell functions. We have enhanced cell adhesion by adding immobilized cell-adhesive proteins or oligopeptides in the hydrogel, which is beyond the scope of this article.

Reference

[1] Procedure number: National Inpatient Profile 1991 Data, Hospital Discharge Survey, length of stay, 1991 Diagnostic Related Groupings, Federal Register, Department of Health and Human Services (Medicare-based information).

[2] American Liver Foundation, Vital Statistics of the United States. 1988.

[3] Langer, R., Vacanti, J.P., *Tissue Engineering.* Science, 1993. **260**(5110): p. 920-926.

[4] Hutmacher, D.W., Goh, J.C.H., Teoh, S.H., *An introduction to biodegradable materials for tissue engineering applications.* Annals Academy of Medicine Singapore, 2001. **30**(2): p. 183-191.

[5] M. Madou, *Fundamentals of Microfabrication*, CRC, 2002.

[6] Zhang, X., Jiang, X.N., Sun, C., *Micro-stereolithography of polymeric and ceramic microstructures.* Sensors and Actuators a-Physical, 1999. **77**(2): p. 149-156.

[7] Kai, C.C., Fai, L.K., Liquid-based rapid prototyping systems. In *Rapid Prototyping: Principles and Applications in Manufacturing*. 1st Ed, pp 27-77, John Wiley & Sons, New York, 1997.

[8] Kawata, S., Sun, H., Tanaka, T., Takada, K., *Finer features for functional microdevices - Micromachines can be created with higher resolution using two-photon absorption.* Nature, 2001. **412**(6848): p. 697-698.

[9] Takagi, T. and Nakajima, N., *Photoforming applied to fine forming.* Jsme International Journal Series C-Dynamics Control Robotics Design and Manufacturing, 1995. **38**(4): p. 811-817.

[10] Bertsch, A., Lorenz, H., Renaud, P., *3D microfabrication by combining microstereolithography and thick resist UV lithography.* Sensors and Actuators a-Physical, 1999. **73**(1-2): p. 14-23.

[11] Itoga, K., Yamato, M., Kobayashi, J., Kikuchi, A., Okano, T., *Cell micropatterning using photopolymerization with a liquid crystal device commercial projector.* Biomaterials, 2004. **25**(11): p. 2047-2053.

[12] Peppas, N.A., Mikos, A.G., *Preparation methods and structure of hydrogels*, In: Peppas NA (ed.), p. 1-26, *Hydrogels in medicine and pharmacy: Fundamentals*. CRC Press, Boca Raton, FL, 1986.

[13] Anseth, K.S., Newman, S.M., Bowman, C.N., *Polymeric dental composites: Properties and reaction behavior of multimethacrylate dental restorations.* Biopolymers Ii, 1995. **122**: p. 177-217.

[14] Koh, W.G., Revzin, A., Pishko, M.V., *Poly(ethylene glycol) hydrogel microstructures encapsulating living cells.* Langmuir, 2002. **18**(7): p. 2459-2462.

[15] Siegel, R., Howell, J., *Thermal Radiation Heat Transfer*, Taylor & Francis, 2001.

[16] Hutmacher, D.W., *Scaffolds in tissue engineering bone and cartilage.* Biomaterials, 2000. **21**(24): p. 2529-2543.

[17] Woodfield, T.B.F., Malda, J., de Wijn, J., Peters, F., Riesle, J., van Blitterswijk, C. A., *Design of porous scaffolds for cartilage tissue engineering using a three-dimensional fiber-deposition technique.* Biomaterials, 2004. **25**(18): p. 4149-4161.

[18] Cuppone, M., Seedhom, B.B., Berry, E., Ostell, A.E., *The longitudinal Young's modulus of cortical bone in the midshaft of human femur and its correlation with CT scanning data.* Calcified Tissue International, 2004. **74**(3): p. 302-309.

[19] Scherzer, T. and Decker, U., *Real-time FTIR-ATR spectroscopy to study the kinetics of ultrafast photopolymerization reactions induced by monochromatic UV light.* Vibrational Spectroscopy, 1999. **19**(2): p. 385-398.

[20] Anseth, K.S., Kline, L.M., Walker, T.A., Anderson, K.J., Bowman, C.N., *Reaction-Kinetics and Volume Relaxation During Polymerizations of Multiethylene Glycol Dimethacrylates.* Macromolecules, 1995. **28**(7): p. 2491-2499.

[21] Billmeyer, F.W., *Textbook of Polymer Science*, 3rd ed., p. 65, Wiley, New York, 1984.

[22] Studer, K., Decker, C., Beck, E., Schwalm, R., *Overcoming oxygen inhibition in UV-curing of acrylate coatings by carbon dioxide inerting, Part I.* Progress in Organic Coatings, 2003. **48**(1): p. 92-100.

[23] Goodner, M.D., Lee, H.R., Bowman, C.N., *Method for determining the kinetic parameters in diffusion-controlled free-radical homopolymerizations.* Industrial & Engineering Chemistry Research, 1997. **36**(4): p. 1247-1252.

[24] Luck, R.M., Sadhir, R.K., *Expanding Monomers*, pp. 1, CRC Press, Boca Raton, FL, 1992.

[25] Bowman, C.N., Peppas, N.A., *Coupling of Kinetics and Volume Relaxation During Polymerizations of Multiacrylates and Multimethacrylates.* Macromolecules, 1991. **24**(8): p. 1914-1920.

[26] Corkhill, P.H., Fitton, J.H., Tighe, B.J., *Towards a Synthetic Articular-Cartilage.* Journal of Biomaterials Science-Polymer Edition, 1993. **4**(6): p. 615-630.

CHAPTER 3: DMD-BASED PROJECTION LITHOGRAPHY FOR MICROLENS ARRAYS

3.1 INTRODUCTION

The history of optics started with the fabrication of glass. This tradition has existed for several thousand years. Artificial glass was discovered accidentally in fired earthenware, through the combination of arenaceous limestone, containing sand, with soda in 7 BC. The traditional methods for the processing of glass are molding, grinding, and polishing. Glass is melted and cast over a mold. Grinding provides a surface as close as possible to the desired shape. Polishing, which is a mechanical/chemical process, finalize optical surface with tolerances well below the wavelength of the light. Dimensions for classical optics are in the range from millimeters up to meters.

The advent of fiber optics for communication purposes as well as for illumination and image transmission systems (e.g., endoscopy) brought with it a trend to miniaturization. Although new techniques were developed such as fiber pulling, the dominant fabrication techniques continued to be the classical ones. In the 70s planar lithographic fabrication techniques were adapted from semiconductor processing to the fabrication of optical components, for example, lenslet arrays [1]. The use of these techniques allows one to generate optical components with dimensions in the micron/submicron range. Various lithographic techniques have been developed for microoptics. The LIGA (German acronym for LIthographie (lithography), Galvanoformung (electroforming) and Abformung (molding)) technique as well as diamond turning have also been demonstrated for the manufacture of microoptical elements [2, 3].

Among all the microoptical elements, microlens arrays are widely used in optical and optoelectronic systems and devices, such as fiber bundle couplers in optical communication systems, charge-coupled devices (CCD), intracavity laser beam shapers, and other related optical applications. At present there are already various methods to fabricate microlenses. Analog methods include micro-jet printing [4], thermal reflow [5], local melting of doped borosilicate glass using focused laser beam [6], and others. The underlying physical principle is the natural tendency of liquid droplets to form quasi spherical shapes on the surface. For example, in thermal reflow technique, a layer of photoresist is patterned lithographically or interferometrically to form small cylinders on a substrate [7]. This structure is heated to temperatures above the glass transition temperature of the photoresist. Due to surface tension the shape of the photoresist cylinders changes to minimize the surface energy. In a good approximation the photoresist islands assume spherical shape. However, an ideal spherical shape can only be formed for specific ratios between the lens diameter and photoresist thickness. Significant deviations may occur if the resist is too thin. Moreover, these techniques are only capable of creating near-spherical lenses while non-spherical lenses are demanded for advanced imaging or lithographic applications.

Direct writing techniques, employing a focused laser beam or an electron beam with a quasi continuous intensity modulation, can generate arbitrary surface profile in an “analog” fashion, although fabricated microlenses are limited to low numerical apertures [8]. Arbitrary profiles can be generated using direct writing. However, due to its serial nature, the main application of this technological approach at the current stage of development is the generation of masters for replication.

Another approach for the fabrication of continuous relief microoptical elements through analog lithography is possible using grey-scale masks [9]. The process is interesting especially for low cost mass fabrication of microoptical components. The exposure through the grey-scale mask results in a continuous intensity distribution in the photoresist coating. The dynamic range of the grey-scale masks determines the achievable profiling depth. Grey scale masks can be fabricated with techniques for the writing of lithographic patterns. For example, aforementioned focused laser beam or electron beam can produce a quasi continuous grey scale via intensity modulation. Grey scale can also be encoded through the density and diameter of binary structures, called halftoning [10]. High energy beam sensitive glass provides higher resolution grey scale mask [11].

Not only can aforementioned processes produce microlens arrays directly, but they can create masters that are capable of replicating optical elements in a massively parallel fashion. Many of the replication techniques which are applied nowadays for microoptical components have evolved from techniques developed for more coarse structures such as compact disks. The first step towards a high quality replication involves electroforming a metal master. The electroforming of the master is performed in a galvanic bath by deposition of Ni or Cu on to the microoptical component. After the metal master is made, replicas can be produced by embossing, injection molding, or solvent casting [12].

In circumstances when specifications of microlens arrays vary frequently from one to another, it is desirable to have a dynamic masking technology that is able to "print" on-demand. Direct writing techniques can draw arbitrary shapes, however the throughput is limited. On the other hand, though photolithographic approaches do offer throughput advantage, the turn-around time and high-cost mask fabrication remain a drawback.

In this chapter, a novel fabrication technique for microlens arrays using DMD as a dynamic grey-scale mask is presented. Relying on its advanced capability of projecting a high resolution grey scale image with a bandwidth of 10 KHz, we were able to fabricate microlens arrays based on photopolymers. The design of the optical elements was simply performed in Powerpoint^{TM}.

3.2 EXPERIMENTAL

3.2.1 Material preparation

1,6-Hexanediol diacrylate (HDDA) (Sigma-Aldrich, refractive index = 1.456), a tetrafunctional monomer was used as received without further purification. It contains 100 ppm monomethyl ether hydroquinone as inhibitor, which is negligible since the concentration of the initiator is orders of magnitude higher than that of the inhibitor. 2,2-Dimethoxy-1,2-diphenylethan-1-one (Irgacure^{TM} 651, Ciba) was dissolved in HDDA to form 0.5 – 3% wt solution. The solution is sonicated, shaken overnight, and kept in dark before use. Glass coverslides (22 X 22 mm) were cleaned in acetone and isopropanol.

3.2.2 Designing grey scale patterns

Grey scale patterns were designed using MatLab, owning to a convenient function of displaying grey scale according to numerical values. For example, to produce a spherical lens element, it was intuitive to use a polynomial function that represents the spherical dome. We started with

$$z = 1 - \sqrt{x^2 + y^2}\ ;\quad x^2 + y^2 \le 1 \tag{3.1}$$

Thus, the spherical dome had its highest value at (0, 0) and zero value at its periphery. The dome was then plotted with respect to X-Y plane. By default, “1” corresponded to the grey scale of “255” (brightest) and “0” to grey scale of “0” (darkest). A circular pattern with smooth gradient was created (Figure 3.1).

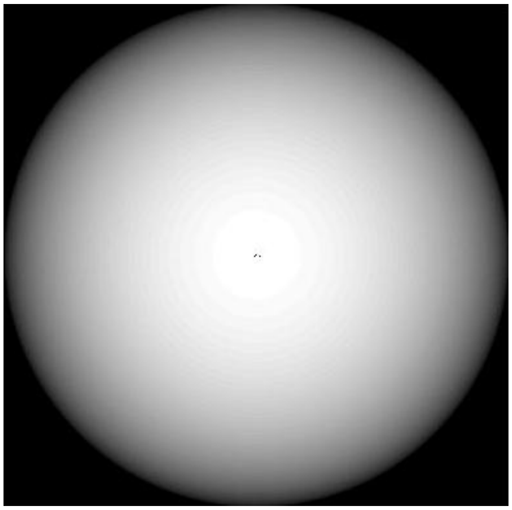

Figure 3.1 A hemispherical grey scale pattern.

Starting from the simplest scenario illustrated above, more complex patterns were drawn, taking consideration of many other factors such as the threshold intensity, non-linear correlation between the intensity and grey scale. The image data were transferred to a PowerPoint file. The pattern was then copied and arranged to a desired form, for instance, a hexagonally packed array.

3.2.3 Direct forming of microoptical elements

A container was mounted on an X-Y motion stage (Figure 3.2). 200 μL photocurable HDDA resin was added to the vat, which was then covered by a glass coverslide, leaving no air bubble in between. An image consisting of pre-designed patterns was projected onto the interface between the substrate and the resin. Since the resin was an absorbing and photobleaching medium, the light with a higher intensity penetrated deeper at that point. Consequently, the solidification of the resin was deeper at that point. The spherical dome pattern mentioned above resulted in an approximately spherical lens element. Shapes of the elements were fine tuned by adjusting the intensity profile and exposure time.

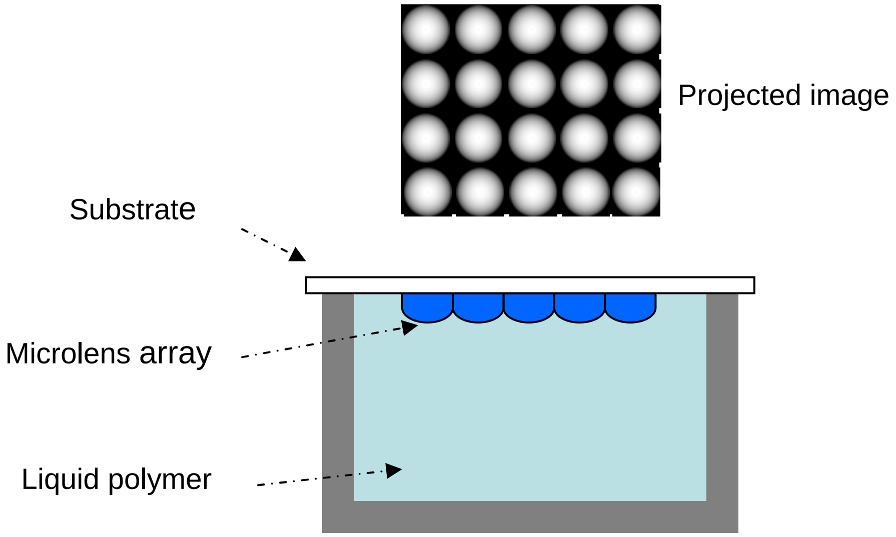

Figure 3.2. Schematic of diagram of DMD projection apparatus for direct fabrication of microlens arrays.

3.2.4. Post process

Since the fluence at each location of the elements varied, the degree of conversion, optical and mechanical properties were not homogeneous. Post curing was often necessary in order to leverage the optical and mechanical performance of the optical elements. Samples were released from the container after exposure to the projected image. Residual liquid resin was removed using compressed air. The samples were flood exposed by a UV lamp for 5 minutes at 20 mW/cm^2.

3.2.5. Characterization of microlens arrays

Optical images of resulting microlens arrays were taken by an optical microscope (Zeiss) in reflective and transmission modes. In the reflective mode, the back surface of the glass substrate was covered by black paint. In the transmission mode, a diffusive light source was placed on another side of the elements relative to the objective lens.

A two-dimensional focused spot pattern of the microlenses was recorded. The focal length of each element was measured. A schematic diagram of the experimental setup is shown in Figure 3.3. The microlens array to be tested was mounted on a linear stage, and the entire array was illuminated with a collimated He–Ne laser beam at 632.8 nm. Light passing through the lenses was collected by an objective lens L_3 (10X magnification) and detected by a CCD camera. First, we moved the linear stage till a clear image of the microlens array was observed. We then moved the stage away from the objective lens until the microlenses and the objective lens were in conjugation where an array of tightly focused spots was captured. The distance that the microlens array was moved was equivalent to its focal length. Images were interpreted in MatLab and intensity profiles were visualized.

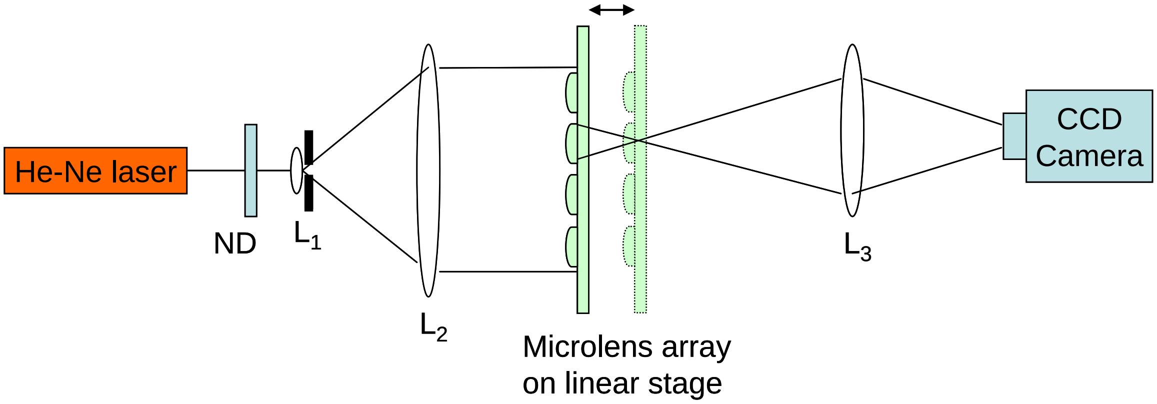

Figure 3.3. Schematic setup of the optical measurement system. The laser intensity was modulated by a neutral density filter. It was then expanded by L_1 and L_2. L_3 was the objective lens in the microscope.

An atomic force microscope (AFM, Dimension 3100, Digital Instruments) was used to measure the surface roughness of the microlenses. We chose tapping mode in order to minimize the physical damage caused by the sharp tip. Several 5 x 5 μm areas were randomly chosen. The scanning rate of AFM was 1 μm/s.

Microlens arrays were coated with a thin layer of gold (~10 Å thick) in a sputter-coater. SEM images were captured at various tilt angles. The topography of the microlenses was based on 90° tilted images. Here we attempted to use a surface profilometer. However, excessive damage was introduced.

3.3 RESULTS AND DISCUSSION

We first studied how the concentration of the photoinitiator affected the resolution using the same approach illustrated in Chapter 2. Highest resolution was achieved at a photoinitiator concentration of 1.5% (w/v). This concentration was used throughout the fabrication of microlenses.

Optical images of a microlens array are shown in Figure 3.3. The diameter of each element was 230 μm and the pitch was 510 μm. Each element was formed by projecting a modified hemispherical intensity profile onto the resin. The intensity on the edge was 90% of the maximum intensity instead of completely dark. This was to meet the threshold intensity at a fixed exposure time of 1.3 sec. Each element had the same dimension over the entire 11 X 7 array. We observed that the microlenses were able to focus the incoming light (Figure 3.4). More evidently, the reflection mode shown that each microlens condensed light coming from the objective lens onto the painted back surface and then recollected the diffusive reflection and sent back to the objective lens. A sharp focusing spot could be seen in the center of each microlens (Figure 3.5).

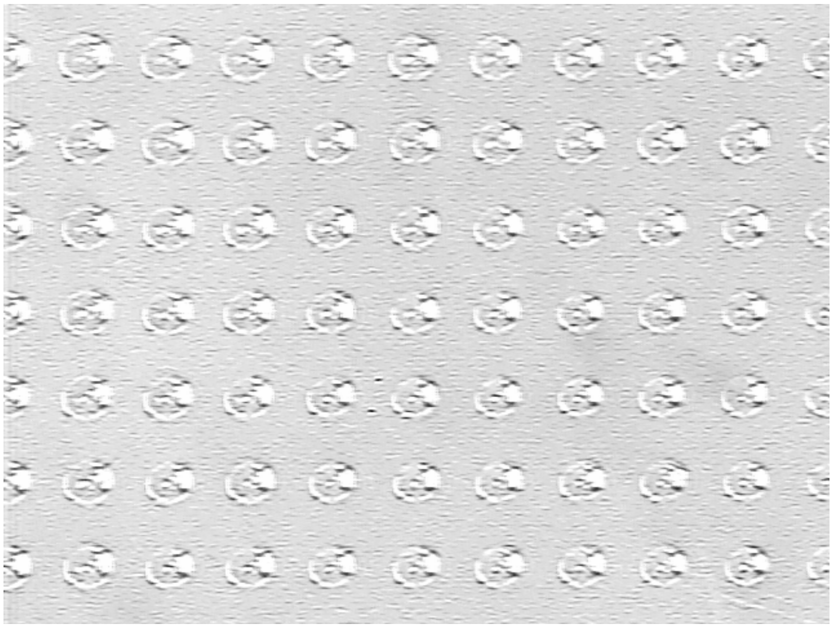

Figure 3.4. Optical micrograph of an 11 X 7 microlens array. Microlens diameter was 230 μm and pitch was 510 μm. Image taken in the transmission mode at 10X magnification.

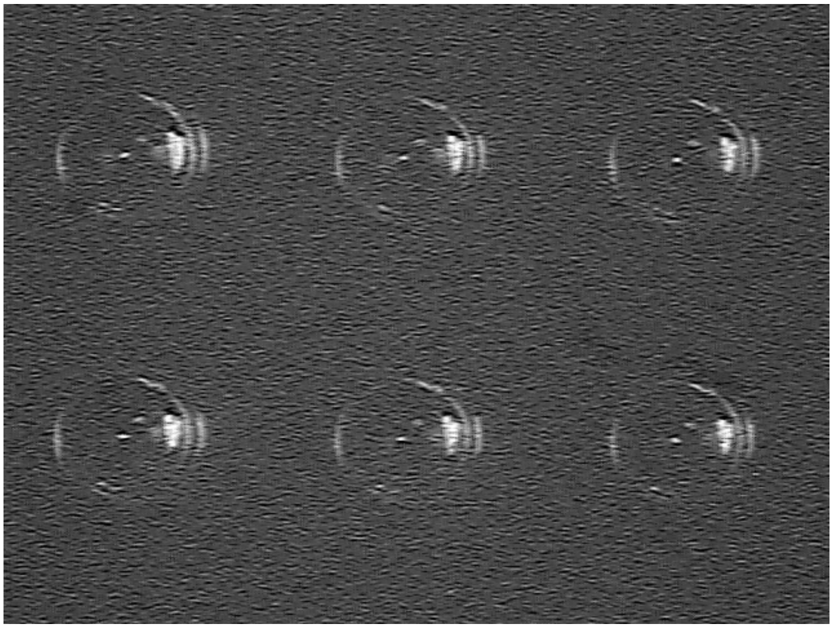

Figure 3.5. Optical micrograph of a microlens array. Microlens diameter was 230 μm and pitch was 510 μm. Image taken in reflection mode at 20X magnification.

Figure 3.6 shown the spot pattern produced by one of the microlenses. A uniform array of such spots was observed over the entire microlens array. The shape of the spot was not circular due to a non-circular laser beam. The shutter speed of the CCD was appropriately adjusted to reveal the first dark ring of the Airy pattern. The spot size defined by the diameter of the first dark ring was measured as 12 μm. The focal length was measured as 300 μm.

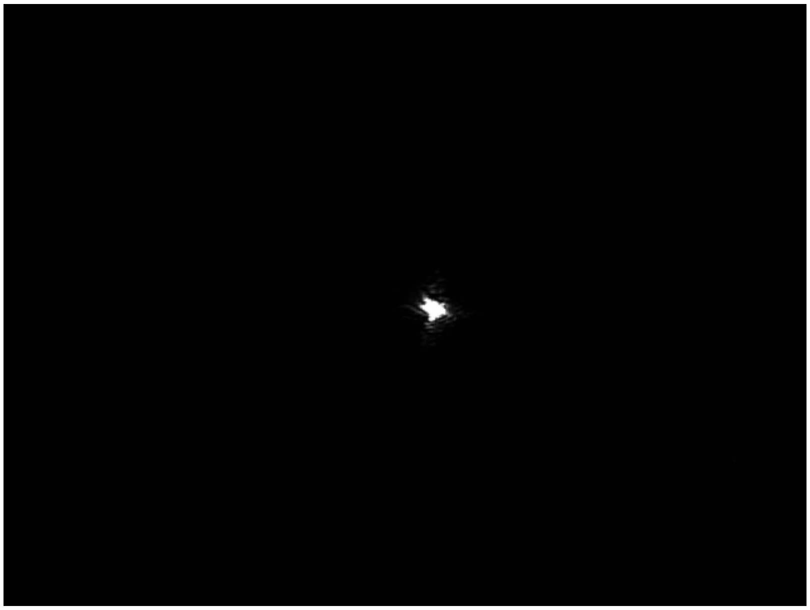

Figure 3.6. Focusing spot produced by a microlens.

The SEM micrograph showed the bird-view of the microlens array (Figure 3.7). It confirmed that each element was identical in shape and size. The surface profile was obtained by a 90° view of the microlens. The lens sag was 72 μm (Figure 3.8). The microlens profile was approximately spherical with a radius ~ 130 μm. The edge of the microlens flattened out, which may due to residual resin.

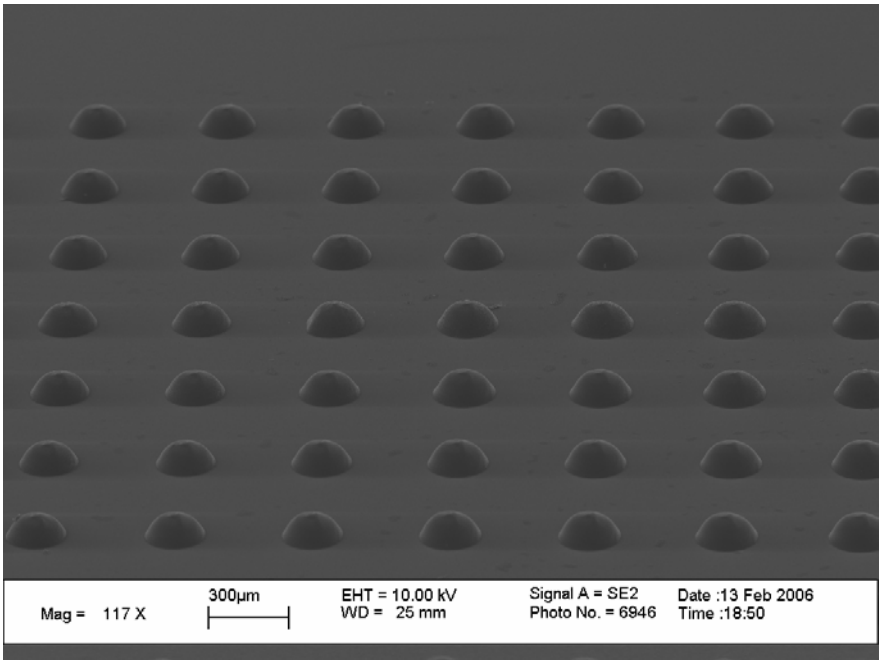

Figure 3.7. SEM micrograph of the microlens array.

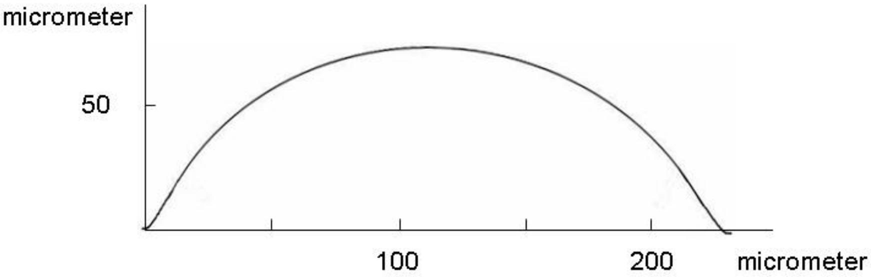

Figure 3.8. Surface profile of a microlens.

The surface roughness was measured by scanning several randomly chosen areas (5 X 5 µm) using AFM. The average surface toughness was 3.0 ± 0.2 nm. Apparently, the surface roughness far exceeded the theoretical possible resolution of 4 µm (image pixel size). We attribute this result to two possible reasons. Firstly, the projection lens was not able to resolve each micro-mirror. The image of each micro-mirror was blurred and was superposed to form a smooth gradient as opposed to a discrete pattern. Second, a thin film of the residual resin may have been left over the surface of the microlenses. The surface tension smoothened out the rough surface. After post exposure, the thin film became the new surface of the microlens.

DMD-based projection lithography offered a considerable degree of flexibility in fabricating microoptical elements. Almost all kinds of microlenses, including aspheric lens and cylindrical lens, can be fabricated using this technique, although only spherical microlens array was demonstrated here. However, there are several important factors that may limit the viability of this technology in certain applications.

Firstly, it is difficult to correlate the intensity profile with resulting microlens profile using theoretical calculation. This is true for most of the techniques that rely on exposing photo-sensitive material by an intensity gradient. It includes laser direct writing, grey scale method, and etc. Experimental calibration combined with semi-empirical equations could and has helped designing fabrication parameters.

Secondly, the residual resin left on the microlenses could change the profile. We have found that as-exposed resin was not completely crosslinked and could swell upon rinsing with solvent. Compressed air could remove the residual more effectively, though it often left a thin film of the resin on the surface.

Thirdly, the resin near the bottom of the microlens receives more energy than that near the tip, which is buried deeper into the surface. This causes inhomogeneous photocrosslinking reaction and may consequently lead to inhomogeneous mechanical and optical properties. As a result, the microlenses may not perform as designed. Flush exposing with UV light can re-activate photocrosslinking reaction and hence improve the uniformity of the properties.

Fourthly, the cross-talking effect may be observed as packing density increases. It may be a result of limited optical resolution and diffusion of reactive species across the element boundary. Additional modification on the intensity profile is necessary in order to fabricate close packed microlens arrays.

Fifthly, the refractive indices may be different in solid and liquid regions due to change in packing density. Light can be focused by the solid part if the refractive index of the solid is greater than that of the liquid. Or light can be diverged by the solid part if the refractive index of the solid is lower than that of the liquid.

3.3 CONCLUSION

In this chapter, DMD-based projection lithography has been shown to be a viable technology for the parallel fabrication of microoptics. Microlens arrays with a spherical surface profile were demonstrated. The prototype microlens array had a pitch of 510 µm and each element had diameter and sag of 230 µm and 72 µm, respectively. Smaller lens dimension and higher packing density are achievable, while it is limited by optical resolution and diffusion of reactive species. This technology is of practical interest for a large number of applications in which the attraction of low-cost, fast turn-around and flexible design outweighs the current limitation of resolution and profile fidelity. These limitations are of experimental origin and are expected to be further reduced with improvement in DMD resolution and post processing techniques.

Reference

[1] Aagard, R.L., *3-Layer Optical-Waveguide for Photolithographic Fabrication of Thin-Film Lenses.* Journal of Vacuum Science & Technology, 1977. **14**(1): p. 275-277.

[2] Basrour, S., Ballandras, S., Hauden, D., *Application of the LIGA process in microoptics.* Annales De Physique, 1995. **20**(5-6): p. 693-700.

[3] Tamagawa, Y. and Ichioka, Y., *Modulation transfer function of blazed diffractive optics produced by diamond turning.* Optical Review, 1999. **6**(4): p. 288-292.

[4] Danzebrink, R. and Aegerter, M.A., *Deposition of optical microlens arrays by ink-jet processes.* Thin Solid Films, 2001. **392**(2): p. 223-225.

[5] Yang, H.H., Chao, C.K., Wei, M. K., Lin, C.P., *High fill-factor microlens array mold insert fabrication using a thermal reflow process.* Journal of Micromechanics and Microengineering, 2004. **14**(8): p. 1197-1204.

[6] Fritze, M., Stern, M.B., Wyatt, P.W., *Laser-fabricated glass microlens arrays.* Optics Letters, 1998. **23**(2): p. 141-143.

[7] Hutley, M.C., *Optical Techniques for the Generation of Microlens Arrays.* Journal of Modern Optics, 1990. **37**(2): p. 253-265.

[8] He, M., Yuan, X.C., Ngo, N.Q., Tao, S.H., *Single-step fabrication of a microlens array in sol-gel material by direct laser writing and its application in optical coupling.* Journal of Optics a-Pure and Applied Optics, 2004. **6**(1): p. 94-97.

[9] Yao, J., Cui, Z., Gao, F.H., Zhang, Y.X., Gao, F., Du, J.L., Su, J.Q., Guo, Y.K., *Design of hybrid micro optical elements with coded gray-tone mask.* Microelectronic Engineering, 2001. **57-8**: p. 793-799.

[10] Liu, J.S., Waddie, A.J., Taghizadeh, M.R., *Fabrication of diffractive-optical elements by using halftone gray-scale masks.* Optics Communications, 2002. **208**(1-3): p. 31-40.

[11] Lu, Y.T., Chu, C.S., Lin, H.Y., *Characterization of the gray-scale photolithography with high-resolution gray steps for the precise fabrication of diffractive optics.* Optical Engineering, 2004. **43**(11): p. 2666-2670.

[12] Gale, M., *Replication, in Micro-optics: elements, systems and applications*, Herzig, H.-P. (ed), p. 152-177, Taylor & Francis, London, 1997,.

Chapter 4: Mechanisms of Photoinitiated Polymerization and Crosslinking and Numeric Modeling

4.1 PHOTOINITIATED POLYMERIZATION

Photo-initiated polymerization and polymer crosslinking are viable strategies for biomaterial synthesis. These reactions can be carried out under a wide range of conditions, including variations in monomer and initiator structures, concentration of functional groups and initiator, temperature, atmosphere, irradiation intensity, and exposure time. Photo-initiated polymerization and polymer crosslinking also provide an avenue to fast and contamination-free manufacturing of MEMS and micro-opto-mechanical systems (MOMS).

While fabrication based on photopolymerization allows a range of materials to be produced and has a number of advantages compared to other types of micro-fabrication processes, there are several constraints that must be addressed when implementing photopolymerization technology. The most important caveat is that only a thin layer of resin is solidified at one exposure. As light from the illumination source penetrates the sample, it is absorbed by the initiating species (along with monomer and polymer moieties in some systems), causing a decrease in the light intensity with depth into the sample. This gradient in light intensity causes gradients in the polymerization rate and double bond conversion. The sample surface closest to the illumination source may have a higher polymerization rate and conversion due to the increased rate of photoinitiation, giving an inhomogeneous sample for ‘optically thick’ films [1]. Photobleaching initiators, which have a greatly decreased absorbance after photolysis, and non-photobleaching initiators, whose absorbance do not vary significantly after photolysis, lead to different polymerization scenarios. It is important to determine proper system parameters to build layers of polymers with a minimum thickness and homogeneous properties in fabricating tissue engineering scaffolds. On the other hand, controlling the curing depth via grey scale exposure is particularly essential to fabricating geometric elements using projection lithography. Also, polymerization does not necessarily terminate once the light has been turned off. In fact, dark reactions are common in photopolymerization and shall be considered in designing system parameters. Flach and Chartoff have modeled the influence of light intensity on curing depth and monomer conversion and dark reaction with both stationary and moving laser beam [2]. Pavlinec and Moszner have experimentally investigated dark reactions and what post-curing influences affected these reactions [3].

Our model was established based on Flach and Chartoff's work and intended to provide guidance to fabrication of tissue engineering scaffolds and microlens arrays. Numerical results were obtained based on kinetic data from literatures. Due to the lack of experimental data on PEG(1000)DMA, only the system consisting of HDDA and Irgacure 651 was analyzed.

4.2 MODELING

Photoinitiated radical polymerization can be described by the following reaction sequence:

$$S \xrightarrow{hv,k_{i1}} R\cdot \tag{4.1}$$

$$R\cdot + M \xrightarrow{k_{i2}} RM\cdot \tag{4.2}$$

$$RM\cdot + M \xrightarrow{k_p} RM_2\cdot \tag{4.3}$$

$$\downarrow$$

$$RM_{n-1}\cdot + M \xrightarrow{k_p} RM_n\cdot \tag{4.4}$$

$$RM_{m1}\cdot + RM_n\cdot \xrightarrow{k_t} RM_{m+n}R \tag{4.5}$$

where S stands for the initiator, R for the radical, M for the monomer, k_{i1} for the rate of generation of primary radical, k_{i2} for the rate of generation of macro radical, k_p for the propagation rate constant, k_t for the radical combination rate constant assuming bi-molecular combination.

Initiation process: The process begins with initiation and radical transfer, followed by propagation, and ended by termination where two active polymer radicals form dead polymer.

Two basic steps characterize photoinitiation: the absorption of light to excite a compound and the resulting photochemical reaction of the excited compound. Absorption of a photon of light causes electronic excitation. The energy causing excitation, E, is described by

$$E = hc/\lambda \tag{4.6}$$

where h is Planck’s constant, c is the speed of light, and ¸ λ is the wavelength of the exciting light. Light absorption is described by

$$a = \varepsilon Cl, \tag{4.7}$$

where ε is the molar absorptivity (extinction coefficient), C is the concentration of the species, and l is the light path length. The extinction coefficient, a constant for a compound at a specific wavelength, is an experimental measure of the probability of absorption at that wavelength. The magnitude of the extinction coefficient depends upon the compound’s chromophore, the chemical moiety responsible for the absorption of light. Typical chromophores contain unsaturated functional groups such as C=C, C=O, NO_2, or N=N. Knowledge of the absorption characteristics of the individual species aids in the design and development of microstructures and devices, by allowing proper choice of initiator concentration and radiation source. The absorption of photons may lead to bond scission, which generates one or more primary radicals.

In a liquid solution, effective radical yields are substantially lower because of cage recombination. The solvent surrounding the initiator molecule at the moment of scission forms a molecular “cage”, which must rearrange before the initiator fragments can separate. It is important for us to keep in mind that the quantum yield of initiation also depends on monomer concentration. Noyes’ calculation has indicated that a higher monomer concentration may significantly improve quantum yield because monomer is catching primary radicals before recombination [4]. This is part of the reason we observed a shorter gelation time in resin with a higher monomer concentration. On the other hand, a highly viscous solution increases the chance of cage recombination and hence decreases the quantum yield.

In most cases, fragmentation occurs from the excited triplet state; the triplet state yield, therefore, is an important parameter. In the presence of air, fragmentation from the triplet state competes primarily with triplet quenching by oxygen. Molecular oxygen has a triplet ground state, which reacts eagerly with excited triplets, leading to the formation of singlet oxygen and the ground state of the initiator. This reaction does not reduce the number of initiator molecules but retards the rate of radical generation. This undesirable reaction with oxygen occur prevalently at the air interface where the concentration of O_2 is $\sim 10^{-2}$ M relative to $10^{-3} - 10^{-4}$ M in organic and aqueous media. This is particularly important in stereolithography, where polymerization only occurs in a thin layer adjacent to the air interface. It is not only necessary to remove oxygen dissolved in the bulk resin, but also to prevent ingress of ambient oxygen, especially at a low concentration of initiator.

Investigating how system parameters, such as the light intensity and exposure time, affect the initiation process and hence the geometries of solidified polymer is of particular interest in stereolithography. It has long been recognized that classical Beer-Lambert law is not directly applicable to photopolymerization. The change in absorptivity which accompanies the photochemical reaction results in significant time-varying concentration gradients.

We start from the simplest scenario, in which the intensity profile of the light follows a uniform distribution, while a more complex profile can be substituted in difference cases.

$$I = I_0, \text{ at } z = 0 \tag{4.8}$$

where I_0 is a constant light intensity and $z = 0$ at the liquid surface. With ε being the absorptivity constant of the photoinitiator, the rate of change of the intensity with respect to the depth is

$$\frac{\partial I(t,z)}{\partial z} = -\varepsilon SI \tag{4.9}$$

where S is the concentration of the photoinitiator. The rate of conversion is proportional to the light intensity and initiator concentration.

$$\frac{\partial S(t,z)}{\partial z} = -\gamma\varepsilon IS \tag{4.10}$$

where γ is the quantum yield. To solve the equation, let

$$Q(t,z) = -\varepsilon\gamma\int_0^t I(t,z) \tag{4.11}$$

$$S = S_0 e^Q \tag{4.12}$$

Differentiate with respect to z and t,

$$\frac{\partial^2 Q}{\partial t \partial z} = -\varepsilon S_0 e^Q \frac{\partial Q}{\partial t} \tag{4.13}$$

Integrate with respect to t,

$$\frac{\partial Q}{\partial z} = -\varepsilon S_0 e^Q + C(z) \tag{4.14}$$

$$C(z) = \varepsilon S_0 \tag{4.15}$$

Thus,

$$\frac{\partial Q}{\partial z} = -\varepsilon S_0 (e^Q - 1) \tag{4.16}$$

Integrate with respect to z,

$$Q - \log(1 - e^Q) = \gamma S_0 z + G(t) \tag{4.15}$$

Apply boundary condition *Q(0,t)=-εγI₀t* and *I(0,t)=I₀,*

$$G(t) = -\varepsilon \gamma I_0 t - \log(1 - e^{-\varepsilon \gamma I_0 t}) \tag{4.16}$$

Solving for *Q* yields,

$$Q = \gamma S_0 z + G(t) - \log(1 + e^{\gamma S_0 z + G(t)}) \tag{4.17}$$

Solving for *I* by differentiating *Q* with respect to *t* gives,

$$I(z,t) = I_0[1 - e^{-\gamma \varepsilon I_0 t}(1 - e^{\varepsilon S_0 z})]^{-1} \tag{4.18}$$

$$S(z,t) = S_0[1 - e^{-\varepsilon S_0 z}(1 - e^{\gamma \varepsilon I_0 t})]^{-1} \tag{4.19}$$

The peak light intensity was converted to Einstein (mole of photon) assuming an effective wavelength of 365 nm. Extinction coefficients were estimated from UV-Vis spectra of Irgacure 2959 and Irgacure 651 (Appendix). Using parameter values for HDDA photopolymerization in table 4.1, we calculated solutions for equation (4.19). Figure 4.1 depicted the concentration of photoinitiator at various depths in the resin at *t* = 0.5s, 1s, and 3s. It was shown that the light intensity strongly influences the conversion of the photoinitiator to primary radical since conversion was greatest at the surface and at the center of the beam. The conversion quickly diminished towards the bottom of the resin. We also noted that the conversion occurred almost instantaneously. Figure 4.2 shows the photoinitiator conversion at various depths in the resin containing 100% (w/v) and 0.1% Irgacure 2959. It was noticeable that when the photoinitiator concentration was low the generation of radical was slow and light penetration was deep.

Table 4.1 Parameter values for the modeled HDDA/Irgacure 651 system.

Molecular weight of HDDA	226.27
Density of HDDA	1.01 g/ml
Concentration of HDDA	80%
Molecular weight of Irgacure 651	256.3
Molar concentration of HDDA	3.54×10^3 mol/m^3
Molar concentration of Irgacure 651	58.5 mol/m^3
Extinction coefficient of Irgacure 651	20.0 m^2/mol *
Quantum yield	0.1 *
Peak light intensity	3.05×10^{-6} Einstein/m^2 s
Reaction rate constant k_p	1.2×10^2 m^2 mol^{-1} s^{-1}
Reaction rate constant k_t	2.1×10^2 m^2 mol^{-1} s^{-1}

* [5]

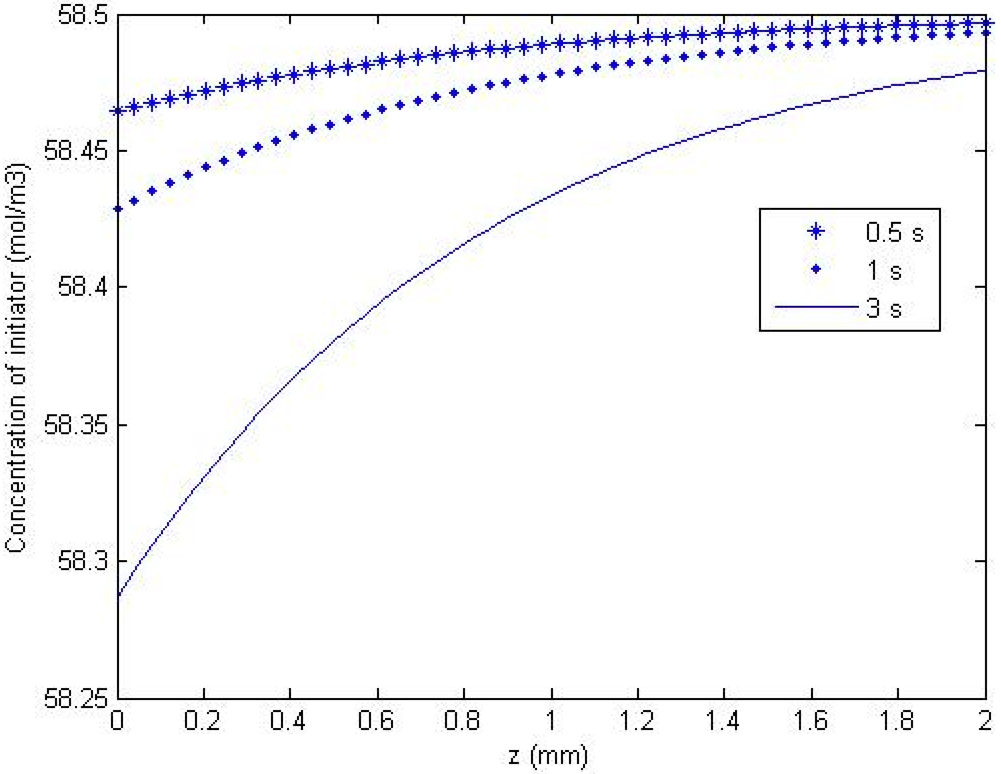

Figure 4.1. Photoinitiator (Irgacure 651) conversion with respect to depth *z* after exposure of 0.5, 1, and 3 seconds. The original concentration was 58.5 mol/m^3.

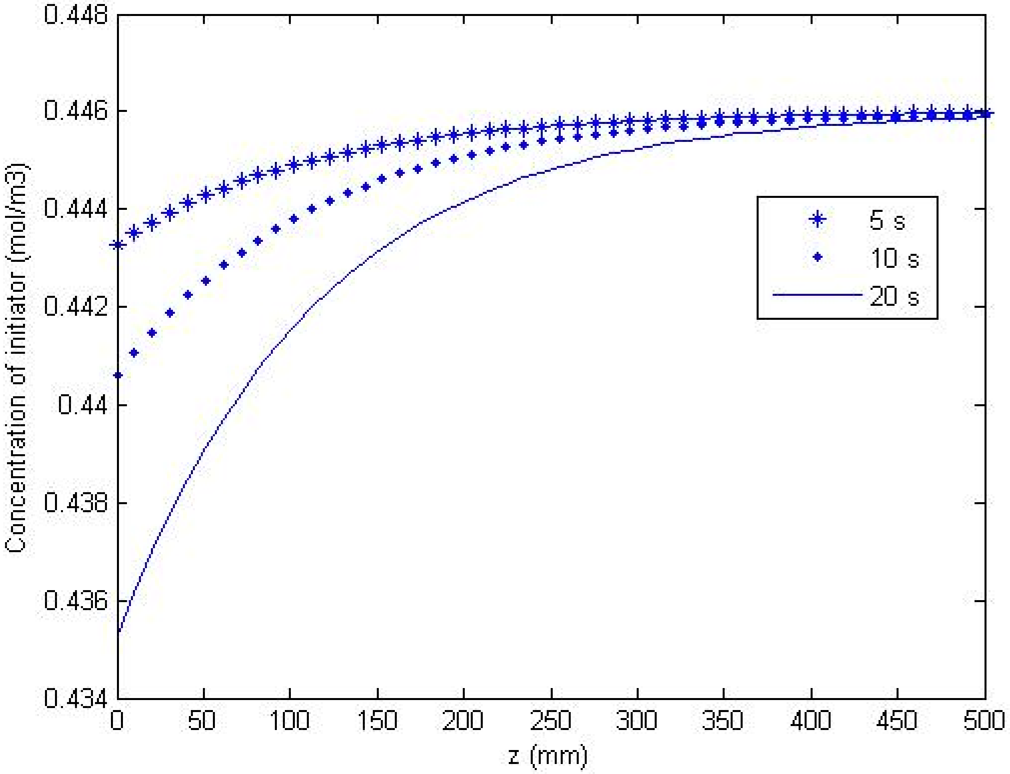

Figure 4.2. Photoinitiator (Irgacure 2959) conversion with respect to depth *z* after exposure of 5, 10, and 20 seconds. The original concentration was 0.45 mol/m^3.

Polymerization process: From the point of view of elementary reaction steps, free-radical crosslinking polymerization does not differ from the linear polymerization of monovinyl compounds. However, the kinetics of network formation show special features arising from the participation of a multi-unsaturated monomer are complicated by other factors not observed in linear polymerizations.

Once a radical chain has been initiated, it propagates spontaneously until it is terminated by encounter with another radical, by disproportionation or in some other way. We assumed bi-molecular termination mechanism (one macroradical is terminated by another), which is the typical method [5]. This process is second order in relation to the total concentration of radicals:

$$r_t = -\frac{d[R]}{dt} = 2k_t[R]^2 \tag{4.20}$$

where r_t is the termination rate. Free radical termination is a diffusion-controlled process. The most important effect of diffusion control for the termination process is the gel effect observed in concentrated systems. Diffusion, includes translational (center-of-mass) and segmental (segmental reorientation), is affected by the extent of conversion. Translational diffusion decreases as reaction proceeds due to an increasing viscosity of the system, which segmental diffusion increases. When the increase in segmental diffusion is taken over by decrease in translational diffusion, the rate of termination decreases rapidly as the reaction proceeds.

On the other hand, propagation involves the reaction of small monomer molecules and only one macro radical. Therefore, propagation is much less hindered by diffusion. The difference in propagation and termination rates induces autoacceleration. At high conversions, propagation also becomes diffusion controlled, and the rate of reaction decreases.

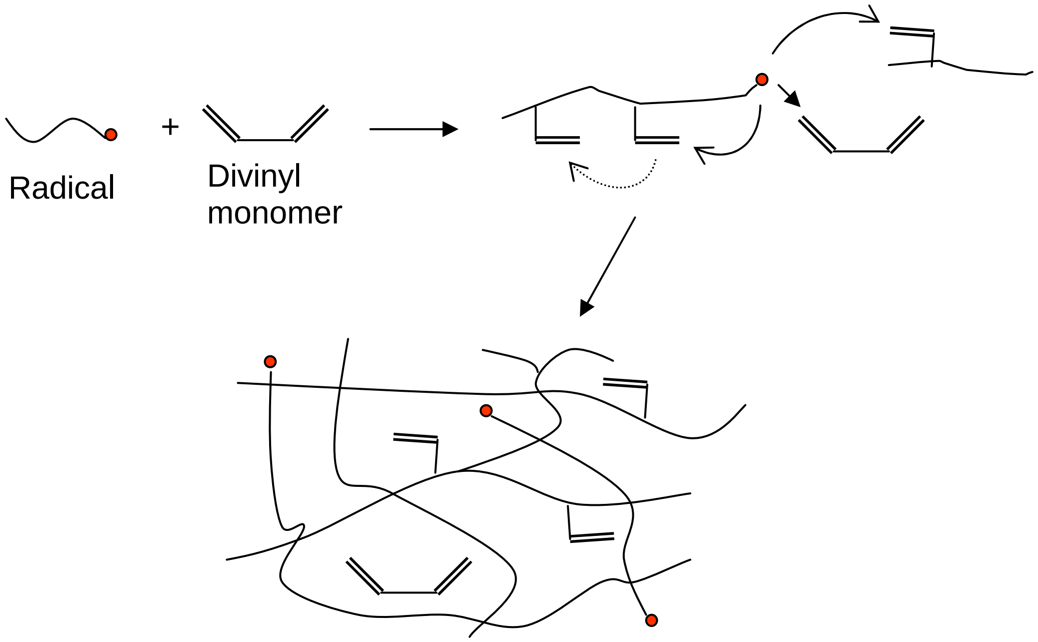

Figure 4.3. Network formation.

For multifunctional systems such as di(methyl)acrylates, propagation can proceed by either intramolecular path or intermolecular path (Figure 4.3). For short or flexible molecules, such as HDDA, the apparent reactivity of pendant double bonds on the same chain is initially enhanced due to their larger concentration in the vicinity of the radical site. This leads to extensive cyclization and formation of microgels in the beginning of polymerization. Further reaction occurs by the chemical joining of microgel particles. Cyclization not only causes a delay in gelation time, but also decreases conversion due to entrapping of unreacted radicals. Moreover, the formation of microgels is the reason for network inhomogeneity, which affects optical properties, and can lead to a significant reduction in the mechanical strength. Cyclization can be suppressed when the connecting "bridge" is very long, as for α , ω-unsatuated monomers like PEG(1000)DMA [6]. The gelation point we measure in our experiment is when microgels join together to form one large molecule. This can occur at conversions as low as 1-2%! Therefore, we must understand that the gelation time only indicates how fast the gel formation occurs, not the polymerization rate or conversion rate. We have found that some systems form gel rather quickly but the final structure is not as stiff compared to systems that have slower gel formation. During scaffold fabrication, we shall evaluate the trade-off between the fabrication speed and structure stiffness for different applications.

We modeled the polymerization reaction as first order differential equations that represent the mass balance of the reacting species:

$$\frac{\partial M(z,t)}{\partial t} = -k_p M(z,t) R(z,t) \tag{4.21}$$

$$\frac{\partial R(z,t)}{\partial t} = -\frac{\partial S(z,t)}{\partial t} - k_t R(z,t)^2 \tag{4.22}$$

where M is the concentration of monomer, R is the concentration of radicals, k_p is the reaction rate constant for propagation, k_t is the reaction rate constant for termination. To simplify the model, we did not consider the second initiation term because k_{i2} was negligible as compared to k_p. We also neglected the diffusion of reactive species, the effect of inhibitors, and the changes in the viscosity of the reaction medium. As mentioned earlier, gel formation significantly limited the mobility of macro radicals. A portion of these radicals were trapped and were not able to propagate. Radical trapping was a rather complicated effect. Although we did not incorporate this factor in our model, we should keep in mind that the final conversion rate may be less than 1. Polymerization did not cease once the light was extinguished, but reactions continue in the dark period. This model represented the dark reaction. The determination of actual polymerization rate coefficients for crosslinking systems is very difficult due to the complicated behavior of the reaction with respect to reaction kinetics, especially the very early onset of autoacceleration. They may be considered as composite values for several processes contributing to propagation and termination. In this model, we used averaged rate constants obtained from Ref. [5].

To model the formation of a microlens element, we formulated a hemispherical intensity distribution. Since it was axial symmetric, it can be represented in 2D (Figure 4.4).

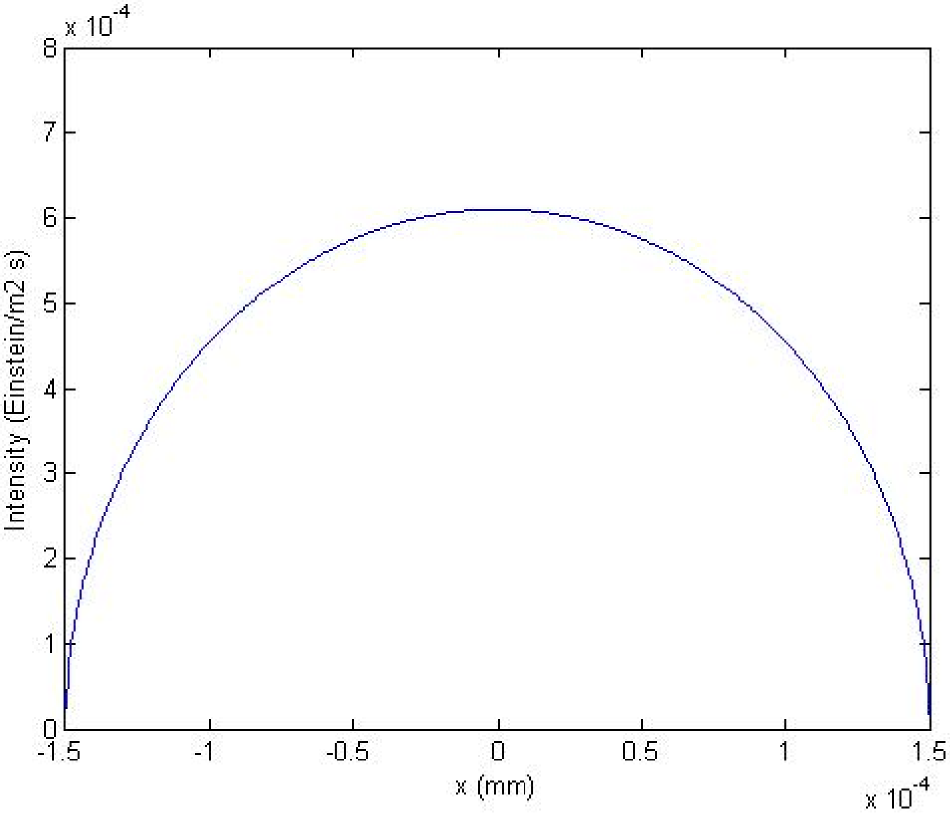

Figure 4.4. A Hemispherical intensity distribution.

Equation (4.20) and (4.21) were solved using a finite difference method:

$$M_{t+1} = M_t + \Delta t \cdot (-k_p M_t R_r) \tag{4.23}$$

$$R_{t+1} = S_t - S_{t+1} + R_t - \Delta t \cdot k_t R_t^2 \tag{4.24}$$

The total reaction time consisted of the exposure time and dark reaction time. Figure 4.5 shown the monomer concentration after 1.3 seconds of exposure and 1.7 seconds of dark reaction. We noted that a very low concentration of primary radical was needed to lead to a high monomer conversion. A high concentration of photoinitiator was used to lower the penetration depth.

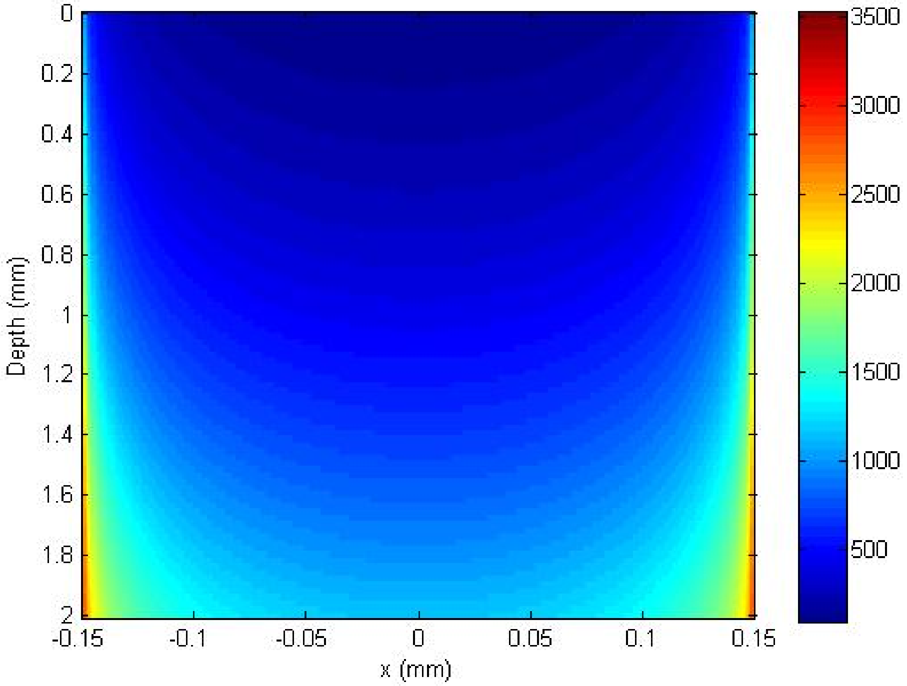

Figure 4.5. Monomer concentration after 1.3 seconds of exposure and 1.7 seconds of dark reaction.

In understanding the curing depth dependence, we first define the cure depth as the depth to which a 3-dimensional gel network is formed during photopolymerization. Coupled with this idea is the concept of a critical conversion for gelation [7-10]. Since the photon propagation through the medium is graded rather than discretized, gel is only formed up to the point at which the degree of cross-linking and polymerization is sufficient to form a solid gel network [11, 12]. The curing depth thus corresponds to a thickness attainable via experimental measurement. Figure 4.6 shows a contour of the monomer conversion rate after 1.3 seconds of exposure and 1.7 seconds of dark reaction. Firstly, we noted that the light fluence lower than a threshold may result in a monomer conversion rate below the critical conversion for gelation. In our case, the actual diameter of the microlens element might be smaller than the projected pattern unless the minimum fluence exceeded the threshold. Secondly, the shape of the contour did not follow that of the light intensity distribution. It was flatter in the center of the beam and steeper on the edge. Thirdly, the penetration of gel formation was deeper than that we observed in the experiment. In addition to the factors illustrated in the context, the discrepancy between the measured intensity and the actual effective intensity may have induced error. The energy meter was sensitive to a broadband of wavelengths, while only a portion of the spectrum was absorbed by the photoinitiator and induced radical generation. Therefore, the effective intensity was lower than that measured.

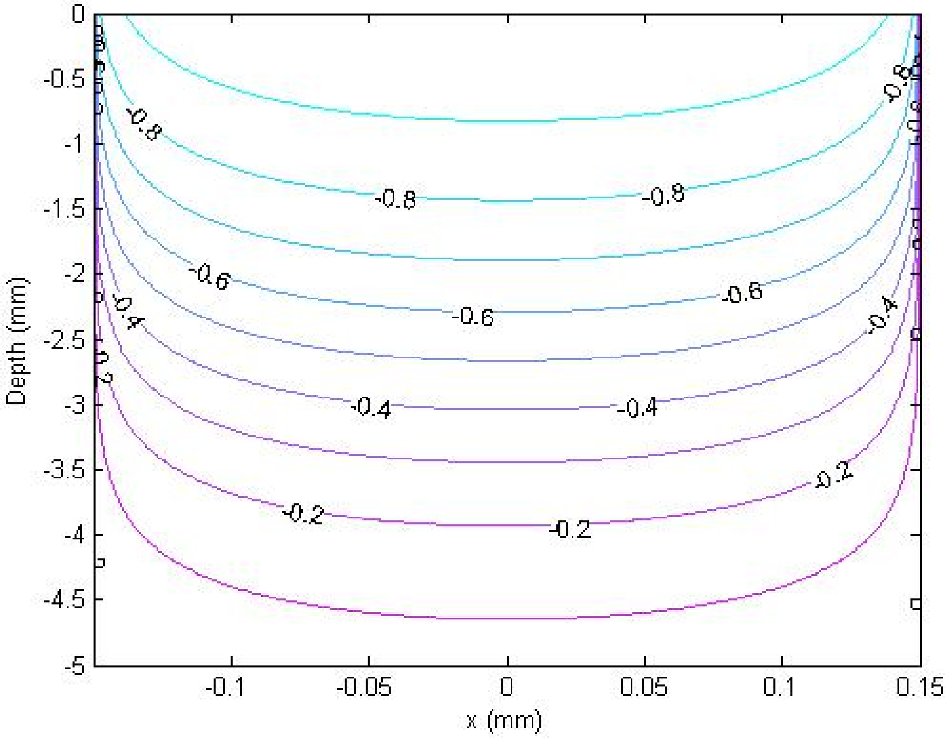

Figure 4.6. Contours of the monomer conversion rate after 1.3 seconds of exposure and 1.7 seconds of dark reaction.

Figure 4.7 illustrated the monomer conversion as a function of the depth for different exposure times with the same dark reaction time. A larger percentage of the monomer was converted to polymer as the exposure time increased.

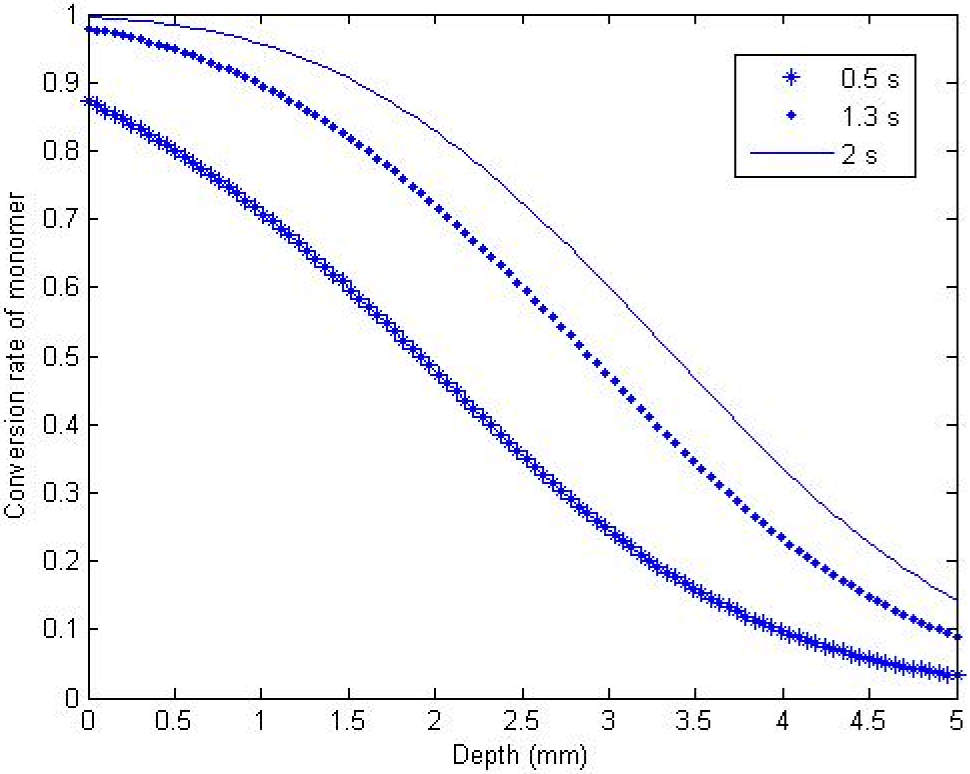

Figure 4.7. Monomer conversion as a function of the exposure times of 0.5, 1.3, and 2 seconds. The dark reaction time remained the same as 1.7 seconds.

Figure 4.8 shows the monomer conversion as a function of depth for different dark reaction times with the same exposure time. The contribution of dark reaction to the monomer conversion was more significant in the middle region of the plot. It was because that the rate of increase of monomer conversion depended upon the multiplex of the radical concentration and monomer concentration.

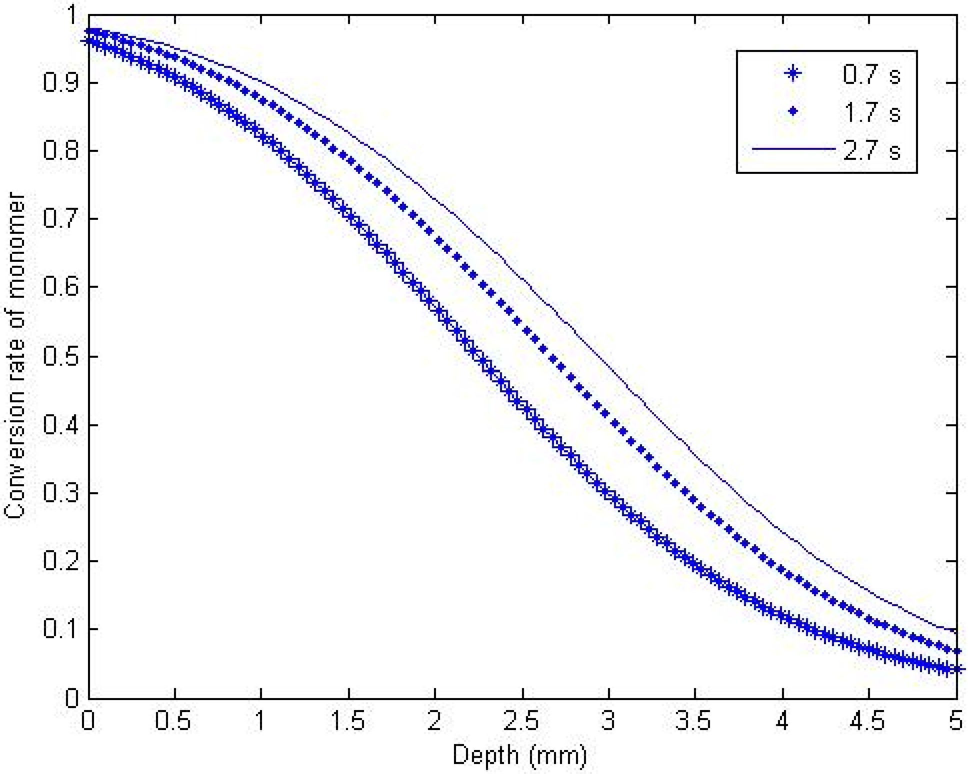

Figure 4.8. Monomer conversion as a function of dark reaction times of 0.7, 1.7, and 2.7 seconds. The exposure time remained the same as 1.3 seconds.

The geometry of the microoptical elements is determined by the light intensity and exposure time. Theoretically any geometry can be made by a properly designed projection pattern. For instance, a prism-like intensity distribution should result in a prism. The intensity distribution is shown in Figure 4.9. This pattern induced a prism-like photoinitiator concentration gradient (Figure 4.10) and hence a prism (Figure 4.11). The actual shape of the prism highly depended upon the gelation point conversion as the slope of the prism would be distorted if gelation point conversion was less than 80%.

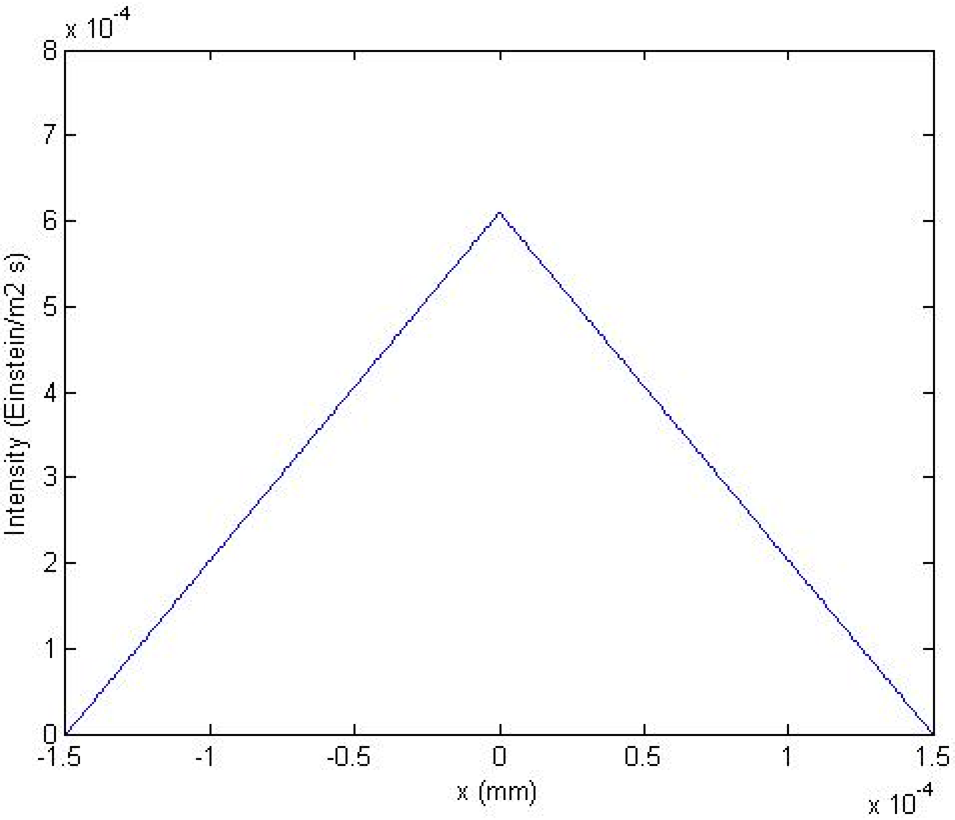

Figure 4.9. Prism-like intensity distribution.

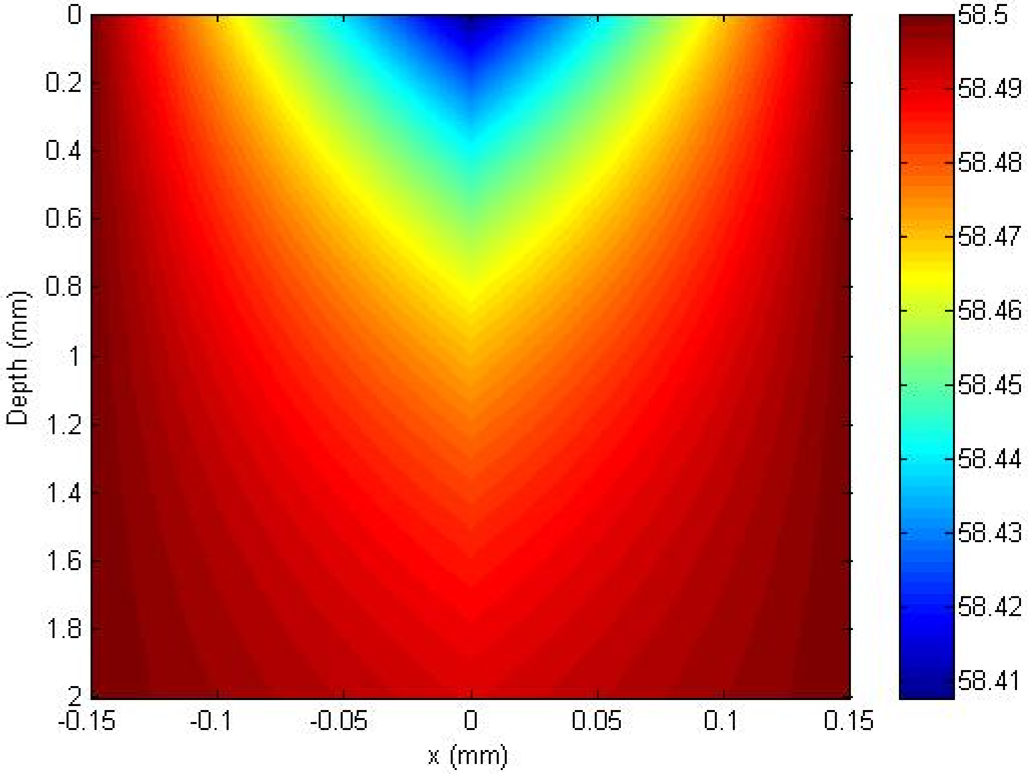

Figure 4.10. Photoinitiator(Irgacure 651) concentration after 1.3 second exposure by the prism-like pattern.

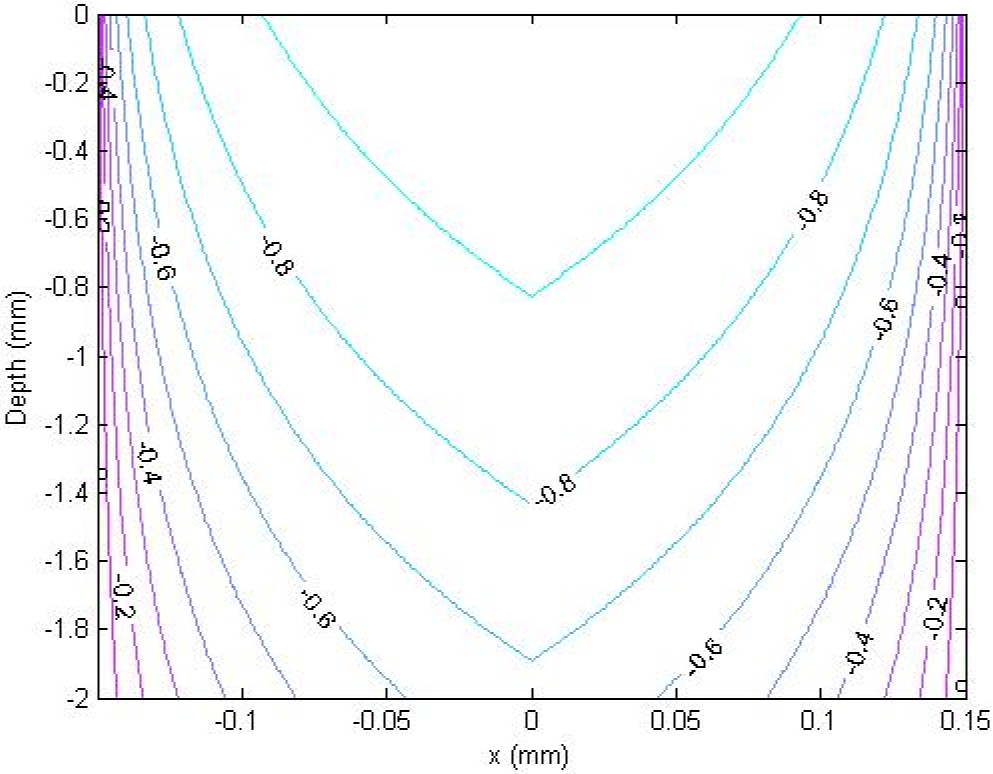

Figure 4.11. Contours of monomer conversion rate after 1.3 seconds of exposure of the prism-like pattern and 1.7 seconds of dark reaction.

4.3 CONCLUSION

In this chapter, we modeled photopolymerization for a photobleaching initiator with the intention to guide the fabrication of microlens arrays using DMD-based projection lithography. We first derived analytic equations that represented photobleaching initiator consumption. We solved differential equations that described the polymerization process using finite difference method assuming bi-molecular termination mechanism.

We showed that the light intensity strongly influenced the polymerization. When the intensity was able to penetrate deeper into the resin, more polymer was formed at these depths. The shape of the polymer resembled that of the microlens element. This model provided guidance to the fabrication of microoptics with desired geometries.

However, the accuracy of the model was limited by assumptions made. Firstly, we assumed that the photoinitiator was the only absorbing medium, whereas HDDA had certain amount of absorption at the effective wavelength as well. Secondly, we were not able to take into account the radical trapping effect. As a matter of fact, radical trapping could be significant in concentrated and viscous systems. We believe this was the reason why monomer conversion was higher than that we observed in experiments at the same location. Thirdly, k_p and k_t were assumed constant throughout the reaction. In fact, they vary at different stages of the reaction.

While the first limitation could be resolved by addition of a non-photobleaching medium, the second and third limitation could only be resolved by using more advanced computational methods. As we have discussed, the mobility of reactive species was one of the most important factor in modeling photopolymerization. A molecular dynamics modeling is a promising candidate to simulate the movement of primary radicals, polymer chains, and chain segments. The major challenge is that it may require extremely large amount of computation power.

Reference

[1] Goodner, M.D., Lee, H.R. Bowman, C.N., *Method for determining the kinetic parameters in diffusion-controlled free-radical homopolymerizations.* Industrial & Engineering Chemistry Research, 1997. **36**(4): p. 1247-1252.

[2] Flach, L., Chartoff, R.P., *A Process Model for Nonisothermal Photopolymerization with a Laser-Light Source .1. Basic Model Development.* Polymer Engineering and Science, 1995. **35**(6): p. 483-492.

[3] Pavlinec, J., Moszner, N., *Dark reactions of free radicals crosslinked polymer networks trapped in densely after photopolymerization.* Journal of Applied Polymer Science, 2003. **89**(3): p. 579-588.

[4] Noyes, R.M., Elektrochem., 1960, **64**:, p. 153.

[5] Perry, M.F. and Young, G.W., *A mathematical model for photopolymerization from a stationary laser light source.* Macromolecular Theory and Simulations, 2005. **14**(1): p. 26-39.

[6] Dušek, K., *Network formation involving polyfunctional polymer chains*. In: Stepto RFT (ed). p. 64, *Polymer networks: principles of their formation, structure and properties.* Blackie Academic and Professional, London, 1998.

[7] P.J. Flory, *Principles of Polymer Chemistry,* Cornell University, Press, Ithaca, NY, 1953.

[8] Rubinstein, M., Colby, R.H., *Elastic-Modulus and Equilibrium Swelling of near-Critical Gels.* Macromolecules, 1994. **27**(12): p. 3184-3190.

[9] Gottlieb, M., Macosko, C.W., *On the Suppression-of-Junction-Fluctuations Parameter in Flory Network Theory.* Macromolecules, 1982. **15**(2): p. 535-537.

[10] Muthukumar, M., Winter, H.H., *Fractal Dimension of a Cross-Linking Polymer at the Gel Point.* Macromolecules, 1986. **19**(4): p. 1284-1285.

[11] Young, J.S., Kannurpatti, A.R., Bowman, C.N., *Effect of comonomer concentration and functionality on photopolymerization rates, mechanical properties and heterogeneity of the polymer.* Macromolecular Chemistry and Physics, 1998. **199**(6): p. 1043-1049.

[12] Kannurpatti, A.R., Bowman, C.N., *Structural evolution of dimethacrylate networks studied by dielectric spectroscopy.* Macromolecules, 1998. **31**(10): p. 3311-3316.

CHAPTER 5: LASER-ASSISTED PHOTOTHERMAL IMPRINTING OF NANOCOMPOSITE

5.1 INTRODUCTION

Thermal embossing/imprinting has been proven as a low cost, mass fabrication method for direct patterning of thermoplastic polymers [1, 2]. Micron-sized features have been imprinted on polymers such as poly(methylmethacrylate) (PMMA) and poly(lactic acid) for biomedical applications, using silicon based molds [3, 4]. By employing a SiO_2/Si mold fabricated by reactive ion etching and e-beam lithography, features as small as 25 nm have been imprinted on PMMA when both the mold and PMMA were heated to a temperature above the glass transition temperature of PMMA (105 °C) [1]. Most recently, the time of the imprinting process has been dramatically shortened by using a pulsed laser as the heating source [5]. As compare to heating the mold or the substrate using conventional heaters, a UV laser beam passes through a transparent quartz mold to heat a thin layer of polymer and the underlying silicon substrate. The viscosity of the polymer layer is reduced by melting and the relief pattern on the mold is successfully imprinted into the polymer within a very short time. However, weak light absorption by the polymer and heat penetration to the silicon substrate has been identified as potential problems.

On the other hand, carbon nanofibers have been recognized as important materials for polymer fillers and reinforcements. Polymers properly filled with carbon nanofibers have shown improved electrical, thermal, and mechanical properties with little property trade-offs [6-10]. For example, polypropylene isotropically filled with carbon nanofibers has shown enhanced thermal stability and as much as a 350% increase in dynamic modulus [10]. Epoxy filled with 1 wt % carbon nanotube has shown a 125% increase in thermal conductivity [11]. For these emerging materials, novel micro/nano fabrication techniques need be developed to meet the requirements of precise device manufacturing [12, 13].

In this chapter, we demonstrate a laser-based, photothermal imprinting method for direct patterning of carbon nanofiber-reinforced, high density polyethylene (HDPE) nanocomposites. Pulsed laser beams of UV and visible wavelengths (pulse width = 10 ns, wavelength of 532 nm and 355 nm) are used to heat the nanofibers in the polymer matrix. Heat is conducted from the nanofibers to the polymer and imprinting is realized when a quartz mold is pressed against the softened/melted polymer composite. Simple heat conduction simulation is carried out to calculate the temperature evolution of both the nanofibers and surrounding polymer matrix.

5.2 EXPERIMENTAL

Carbon nanofibers called Pyrograf-III^{TM} (Applied Sciences, Inc.) were produced by a catalytic process of hydrocarbons in a vapor state. Vapor-grown carbon fibers (VGCFs) have a circular cross-section with diameters ranging from 20 to 200 nm and a central hollow core usually called filaments with diameters of tens of nanometers. Results of scanning electron microscope (SEM) analysis showed that the VGCFs were highly clustered and contained dispersed amorphous carbon and metal catalysts. The preparation of HDPE filled with VGCF was reported by Lozano et al [10]. VGCFs were mixed with the HDPE matrix (10% w/w) in an internal mixer where high shear rates were required to overcome the nanofiber agglomerates. After mixing, the material was compression molded at temperatures ranging from 170 to 200°C between two dust-free parallel silicon wafers to form thin sheets.

To make the quartz mold, a piece of fused quartz plate of surface roughness less than a few nanometers was sputter-coated with a 100 nm chrome layer. Subsequently, an e-beam resist of 500 nm thickness was spin-coated onto the chrome layer. A pattern was directly written onto the resist by electron beam lithography. The exposed resist was developed and the underlying chrome was removed by wet etching to reveal the quartz. The quartz was dry-etched by reactive ion etching (RIE) and the residual resist/chrome was removed using an acetone/chrome etch. Finally, the quartz was treated with (tridecafluoro-1, 1, 2, 2,-tetrahydrooctyl)-1-trichlorosilane vapor to create a surface with low interfacial free energy.

A schematic of the experimental setup is shown in Figure 5.1. An Nd:YAG laser of 10 ns pulse width and 355 nm and 532 nm wavelengths were used for the imprinting process. The quartz mold shown in Figure 5.2a was pressed against the polymer substrate. A single pulse from the laser was passed through the quartz mold, softening or partially melting the top layer of the polymer composite substrate. The relief pattern of the mold was thus imprinted into the substrate and the quartz mold was released after the re-solidification of substrate.

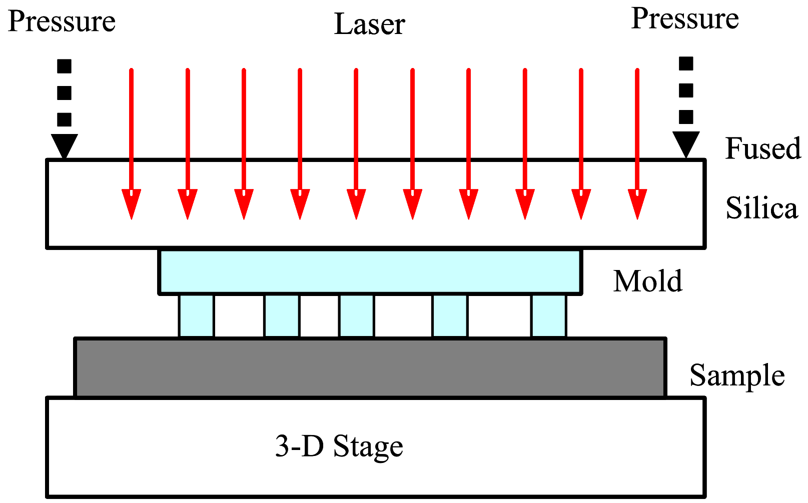

Figure 5.1. Schematic setup of the laser-assisted photothermal imprinting process.

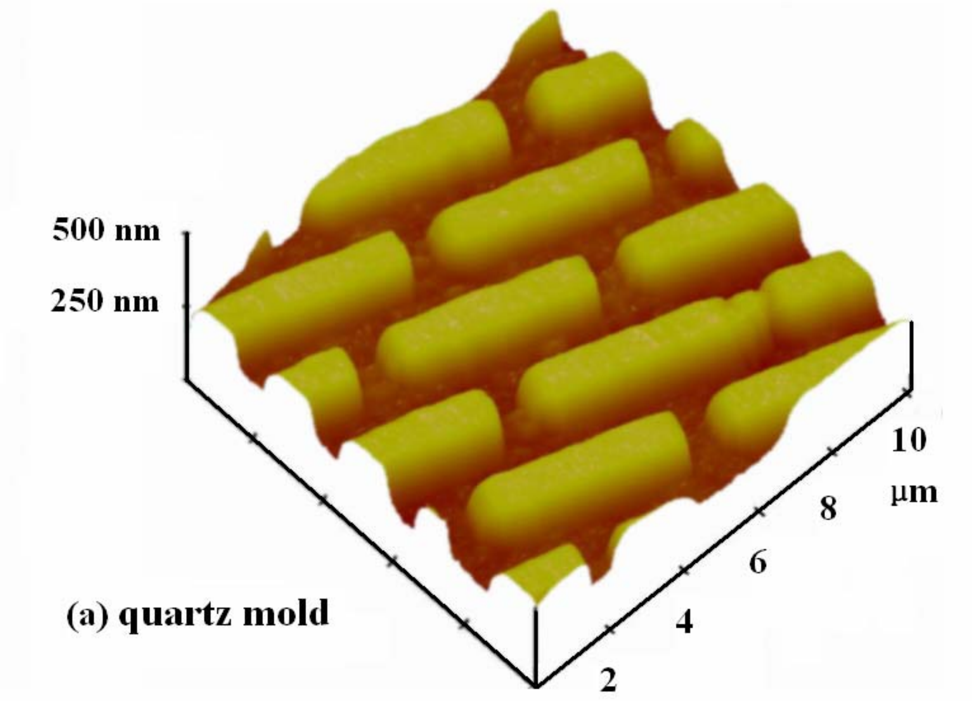
(a) quartz mold

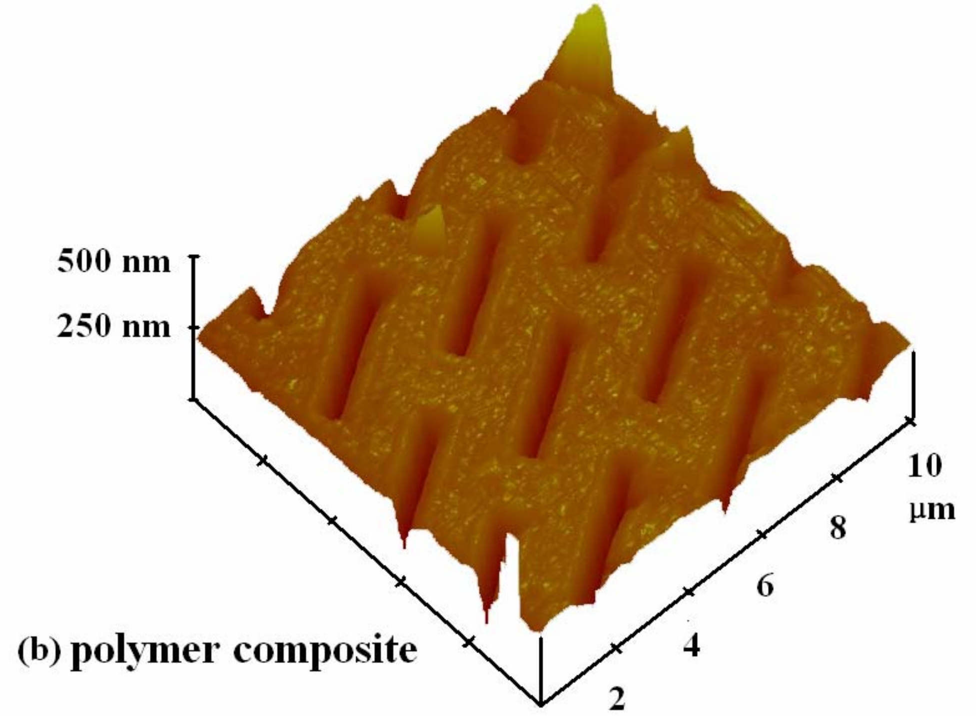
(b) polymer composite

Figure 5.2. AFM images of (a) the quartz mold and (b) the imprinted polymer composite.

The imprinted pattern on the polymer nanocomposite showed high fidelity after being exposed to both the 355 nm and the 532 nm laser beams. The imprinted pattern (Figure 5.2b) had vertical sidewalls and flat smooth top and bottom surfaces, which were identical to the geometry of the quartz mold. As shown in Figure 5.3 after a single 355 nm laser pulse at a fluence of 0.3 J/cm^2, the pattern was completely transferred to the polymer. As illustrated in Figure 5.4, successful pattern transfer was also achieved with a 532 nm laser pulse of the same fluence. However, the surfaces appeared to be porous with noticeable clusters of tangling nanofibers. Since the nanocomposite absorbs the 532 nm laser more strongly, the fluence was closer to the ablation threshold. Therefore, the top surface layer of HDPE was evaporated, leaving the thermally stable carbon nanofibers. By lowering the fluence, we obtained patterns identical to that of a 355 nm laser. Observable defects on the imprinted pattern were a result of ambient dust and material non-uniformity.

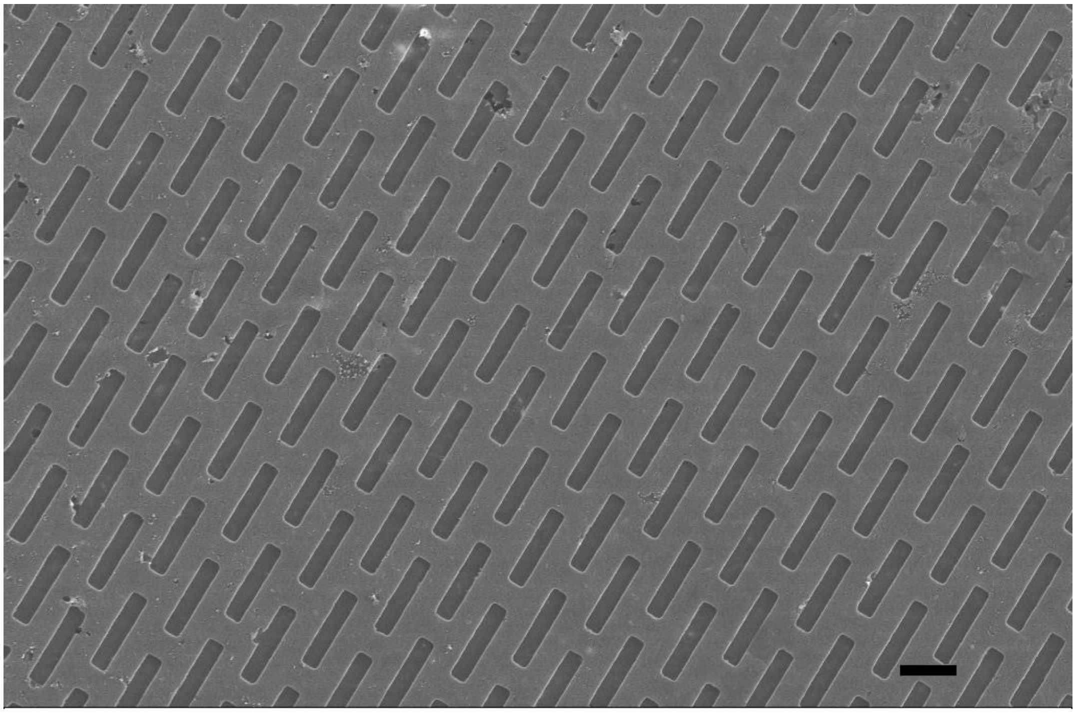

Figure 5.3. SEM images of imprinted surface of polymer composite using 355 nm laser. Scale bars indicate 2 μm.

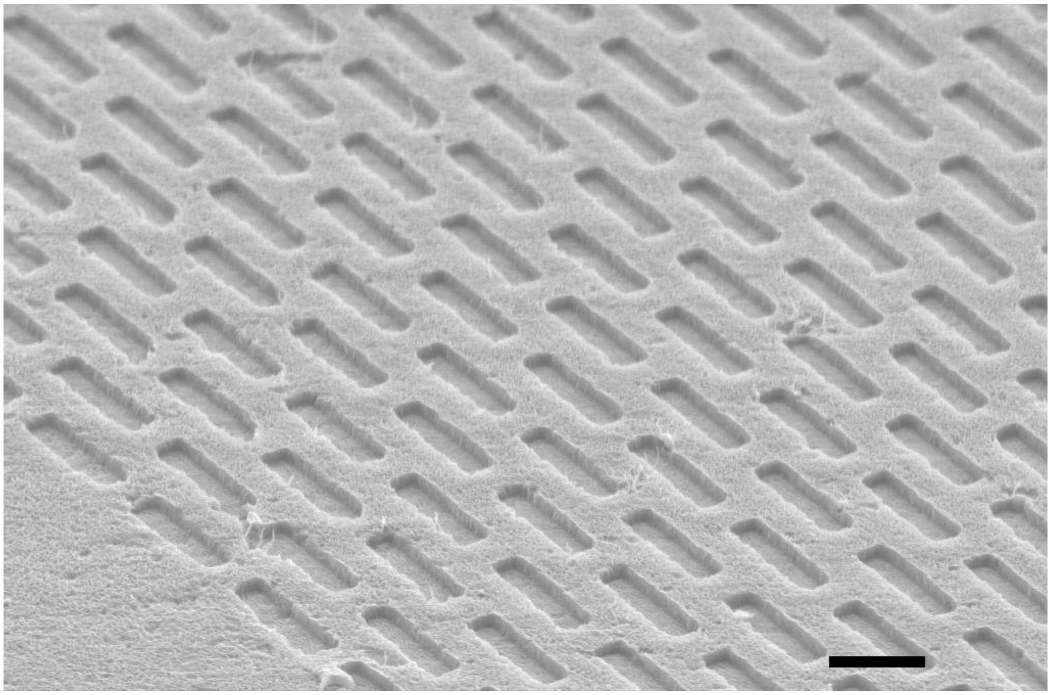

Figure 5.4. SEM images of imprinted surface of polymer composite using 532 nm laser. Scale bars indicate 2 μm.

We have measured the absorption coefficients of the pristine HDPE as 0.42 mm^{-1} at 355 nm and 0.33 mm^{-1} at 532 nm. Due to weak absorption, softening the surface layer of pristine HDPE was difficult. Although the HDPE may absorb radiation in the deep UV spectrum more strongly (e.g. $\alpha \sim 50$ mm^{-1} at 193 nm solely on the basis of carbonyl groups), it may be directly ablated due to photochemical reaction [14, 15]. By adding a small amount of carbon nanofibers to the HDPE matrix we obtained absorption coefficients of 5.71 mm^{-1} at 355 nm and 8.98 mm^{-1} at 532 nm. The highly absorbent carbon nanofibers absorbed the laser radiation and the phonon energy produced by non-radiative decay was responsible for the melting of surrounding polymer. It has been reported that the VGCF filled polymer composites have a much higher thermal conductivity, making it possible to produce deeper patterns [11].

5.3 NUMERICAL MODELING

To help understand the photothermal effect that facilitates the imprinting process, a simple numerical study was conducted using the Fourier heat conduction model, and this model is still valid for nanosecond laser heating processes [16]. Our model consists of two parts, the carbon nanofiber which absorbs the laser radiation and the polymer matrix part that surrounds the nanofiber. The two parts are connected by heat conduction through the interface. All material properties except the specific heat of the nanofiber were obtained from the manufacturer and the handbook [17, 18]. The specific heat of nanofiber was approximated as that of graphite due to lack of information. Although the thermal conductivity of an isolated multi-wall carbon nanofiber was estimated as 1900 W/mK, the effective thermal conductivity of the composite is much smaller than expected due to the interfacial conduction resistance. It was found that the interfacial thermal resistance introduces considerable error in the pure conduction model for nanocomposite materials [19]. Results of molecular dynamics simulation have shown that the energy transfer between the carbon nanofiber and the polymer can be characterized by low-frequency phonon vibration [20]. The high frequency mode phonons resulting from the photothermal effect have to first transfer to a low frequency mode and thus energy transfer is significantly hampered. An interfacial conductance of 5 MW/m$^{2}\cdot$K was incorporated into the model to account for the interfacial heat conduction effect. From the simulation, it is shown that the nanofiber reached temperatures as high as ~1000 K while the temperature in the surrounding HDPE was much lower during the process. Figure 5.5 shows the temperature profile of a nanofiber of 120 nm in diameter and the surrounding HDPE matrix. The results indicate that the HDPE was partially melted both in time and space.

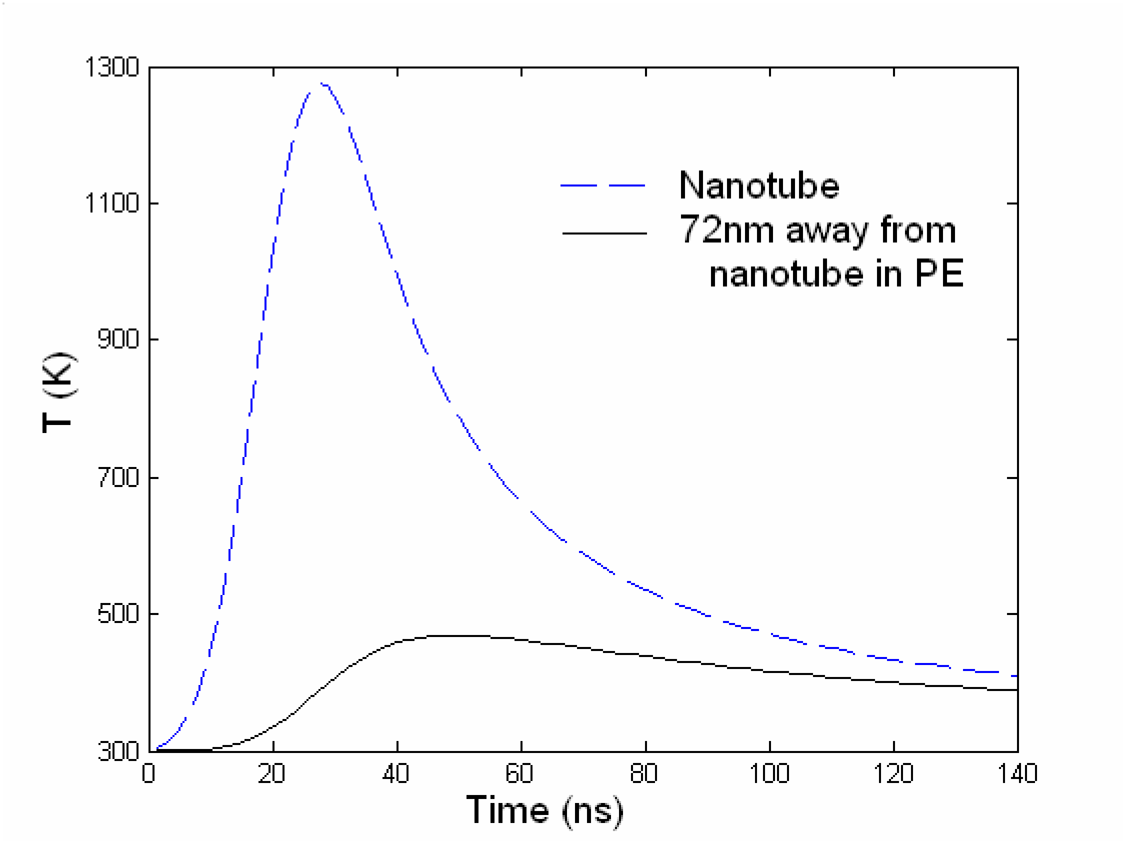

Figure 5.5. Simulation results of temperature evolution in the carbon nanofiber and surrounding polymer matrix after the incidence of a single laser pulse. The melting temperature of the polymer matrix is about 390 K.

5.4 CONCLUSION

In summary, laser-assisted photothermal imprinting is capable of patterning micro-features onto polymeric nanocomposites. By adding carbon nanofibers to the polymer matrix, higher optical absorption levels for a wide bandwidth and higher heat conductance levels can be obtained, dramatically enhancing the imprinting process. We expect nanoscale features are achievable when using a quartz mold with nano-relief structures. This method could be used to fabricate micro/nano-system devices using polymeric nanocomposites with enhanced mechanical, thermal, and optical properties.

Reference

[1] Chou, S.Y., Krauss, P.R., Renstrom, P.J., *Imprint lithography with 25-nanometer resolution.* Science, 1996. **272**(5258): p. 85-87.

[2] Chou, S.Y., Krauss, P.R., Zhang, W., Guo, L.J., Zhuang, L., *Sub-10 nm imprint lithography and applications.* Journal of Vacuum Science & Technology B, 1997. **15**(6): p. 2897-2904.

[3] Armani, D.K., Liu, C., *Mircofabrication technology for polycaprolactone, a biodegradable polymer.* Journal of Micromechanics and Microengineering, 2000. **10**(1): p. 80-84.

[4] Miller, C., Shanks, H., Witt, A., Rutkowski, G., Mallapragada, S., *Oriented Schwann cell growth on micropatterned biodegradable polymer substrates.* Biomaterials, 2001. **22**(11): p. 1263-1269.

[5] Xia, Q.F., Keimel, C., Ge, H.X., Yu, Z.N., Wu, W., Chou, S.Y., *Ultrafast patterning of nanostructures in polymers using laser assisted nanoimprint lithography.* Applied Physics Letters, 2003. **83**(21): p. 4417-4419.

[6] Ash, B.J., Rogers, D.F., Wiegand, C.J., Schadler, L.S., Siegel, R.W., Benicewicz, B.C., Apple, T., *Mechanical properties of Al2O3/polymethylmethacrylate nanocomposites.* Polymer Composites, 2002. **23**(6): p. 1014-1025.

[7] Ramasubramaniam, R., Chen, J., Liu, H.Y., *Homogeneous carbon nanotube/polymer composites for electrical applications.* Applied Physics Letters, 2003. **83**(14): p. 2928-2930.

[8] Sennett, M., Welsh, E., Wright, J.B., Li, W.Z., Wen, J.G., Ren, Z.F., *Dispersion and alignment of carbon nanotubes in polycarbonate.* Applied Physics a-Materials Science & Processing, 2003. **76**(1): p. 111-113.

[9] Wang, Z. and Pinnavaia, T.J., *Nanolayer reinforcement of elastomeric polyurethane.* Chemistry of Materials, 1998. **10**(12): p. 3769.

[10] Lozano, K., Barrera, E.V., *Nanofiber-reinforced thermoplastic composites. I. Thermoanalytical and mechanical analyses.* Journal of Applied Polymer Science, 2001. **79**(1): p. 125-133.

[11] Biercuk, M.J., Llaguno, M.C., Radosavljevic, M., Hyun, J.K., Johnson, A.T., Fischer, J.E., *Carbon nanotube composites for thermal management.* Applied Physics Letters, 2002. **80**(15): p. 2767-2769.

[12] Fournet, P., Coleman, J.N., Lahr, B., Drury, A., Blau, W.J., O'Brien, D.F., Horhold, H.H., *Enhanced brightness in organic light-emitting diodes using a carbon nanotube composite as an electron-transport layer.* Journal of Applied Physics, 2001. **90**(2): p. 969-975.

[13] Blanchet, G.B., Fincher, C.R., Gao, F., *Polyaniline nanotube composites: A high-resolution printable conductor.* Applied Physics Letters, 2003. **82**(8): p. 1290-1292.

[14] Dyer, P.E., Karnakis, D.M., *High-Quality Arf Laser-Ablation of Photoincubated Polyethylene.* Applied Physics Letters, 1994. **64**(11): p. 1344-1346.

[15] Chen, S., Kancharla, V.V., Lu, Y., *Laser-based microscale patterning of biodegradable polymers for biomedical applications.* International Journal of Materials & Product Technology, 2003. **18**(4-6): p. 457-468.

[16] Chen, G., Tien, C.L., *Thermally-Induced Optical Nonlinearity During Transient Heating of Thin-Films.* Journal of Heat Transfer-Transactions of the Asme, 1994. **116**(2): p. 311-316.

[17] Physical properties of Pyrograf-III were found on the Applied Sciences, website: www.apsci.com.

[18] Wilks, E.S. (ed), *Industrial Polymers Handbook: products, processes, applications*, p. 647, Wiley-VCH, New York, 2001.

[19] Hu, M., Wang, X., Hartland, G.V., Salgueirino-Maceira, V., Liz-Marzan, L.M.., *Heat dissipation in gold-silica core-shell nanoparticles.* Chemical Physics Letters, 2003. **372**(5-6): p. 767-772.

[20] . Huxtable, S.T., Cahill, D. G., Shenogin, S., Xue, L. P., Ozisik, R., Barone, P., Usrey, M., Strano, M. S., Siddons, G., Shim, M., Keblinski, P., *Interfacial heat flow in carbon nanotube suspensions.* Nature Materials, 2003. **2**(11): p. 731-734.

Chapter 6: Summary and Prospects

In this dissertation, we demonstrated a powerful DMD-μSL technology in creating pre-designed, spatially patterned scaffolds for applications in cell and tissue engineering. The characterization of the fabrication process and properties of scaffolds will greatly influence the design optimization and hence the efficacy of tissue engineering scaffolds targeting at particular types of tissues and organs.

The success of cell adhesion, proliferation, and differentiation is highly dependent on the design of the scaffold, which includes design of the material and fabrication. That design, in turn, depends on both the tissue as well as the environment in which the tissue resides. Numerous design requirements and variables, as well as the interactions between these variables, create an enormous potential design space. Consequently, many materials utilized to date have been used because they meet one requirement (e.g. cells can easily be mixed with the gel) without regard for other design parameters (e.g. degradation or mechanical properties). Further development on materials will have a great impact on tissue engineering. Co-polymers (e.g., PEG-poly (lactic acid)-PEG di(meth)acrylate) and polymer composites (e.g., hydroxyl apatite composites) could be engineered to meet comprehensive requirements for a specific type of tissue. Various vehicles for bioactive molecule delivery need to be placed incorporated into the scaffold strategically such that specific signals are delivered in an appropriate spatial and temporal manner. On the other hand, more consideration needs to be made on the fabrication of scaffolds regarding to the influence and requirements of external mechanical (i.e. fluid flow) and electrical signals. In addition, most of current scaffold fabrication has been designed in a dimension of micrometers. Nanostructured scaffolds may provide insight into cellular response to objects smaller than the cell itself.

Projection micro-stereolithography would likely expand the process window, allowing high throughput as well as excellent single die registration. Novel designs in dynamic photomasks and imaging optics have rendered a diffraction limited resolution. Imprinting, though limited in 2D or quasi-3D, is probably the best technology when a nanometer feature size and high throughput are demanded. A complex micro/nanostructure may be created by combining two or more fabrication methods. That requires a comprehensive understanding of how materials behave in the fabrication environment (i.e. chemical and physical reaction).

Appendix A

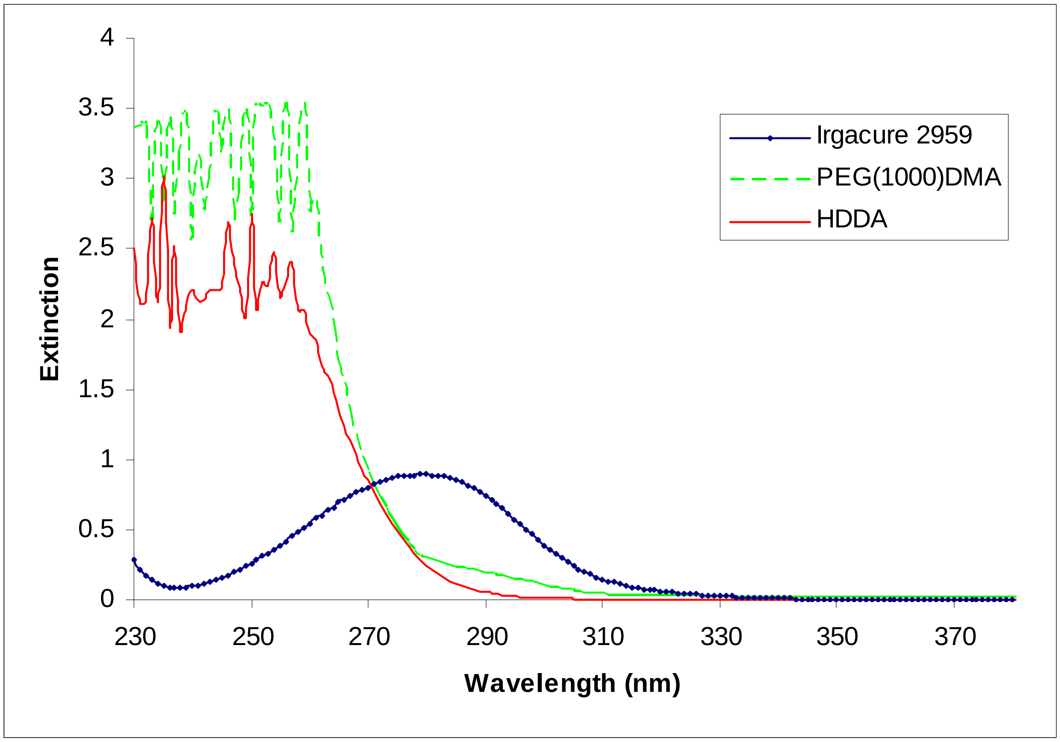

Figure A1. UV-Vis spectra. Irgacure 2959 0.01% (w/v) in water (blue dotted line); PEG(1000)DMA 1% (w/v) in water (red smooth line); HDDA 0.5% (v/v) in acetonitrile.

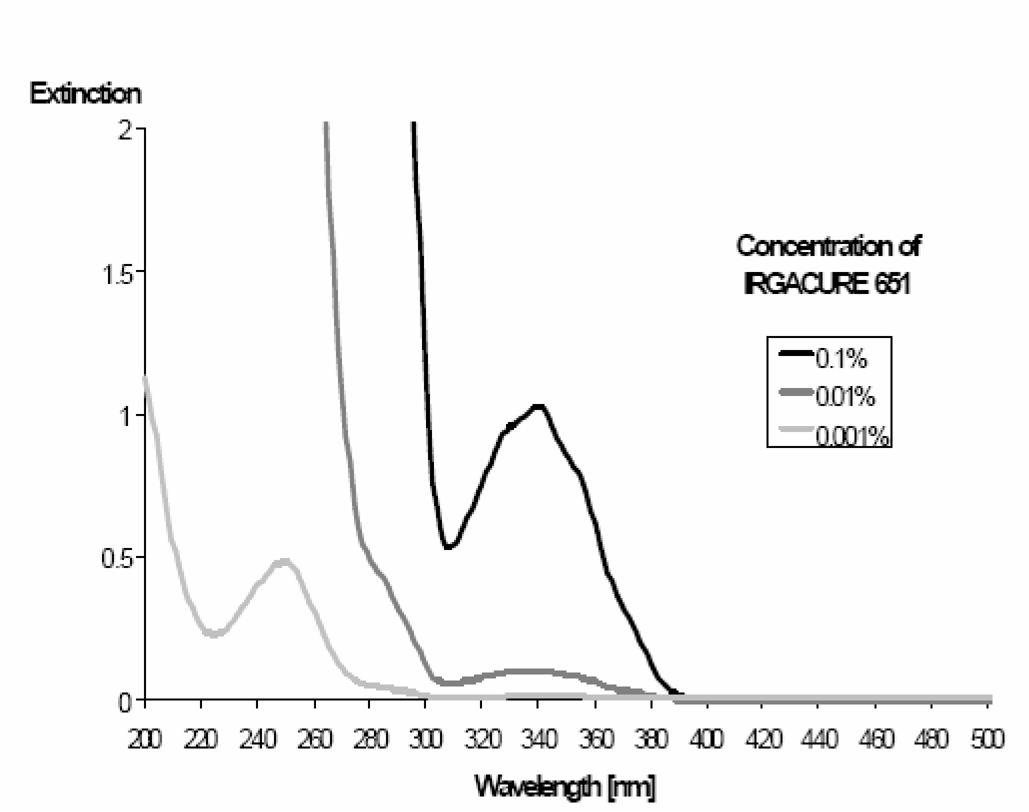

Figure A2. UV-Vis spectra. Irgacure 651 in acetonitrile.

Appendix B

1) Photoinitiator (Irgacure 651) concentration after exposed by a hemispherical pattern.

```
%initiator concentration vs time; hemispherical distribution

x=-1.5e-4:1e-6:1.5e-4;        % Beam width
I0 = 200*3.05e-6;            % Peak intensity
S0 = 58.5;                  % Initial initiator concentration
eps = 20;                   % Extinction
gam = 0.1;                  % Quantum yield
I=zeros(1,length(x));
t = 1.3;                    % Exposure time

for i=1:length(x)
   I(i)=I0/max(x)*(max(x)^2-x(i)^2)^0.5;   % define distribution
end

z = linspace(0,-0.002,1000);   % surface to 2 mm deep
S = zeros(length(x),length(z));
for i=1:length(x)
for j=1:length(z)
   S(i,j)=S0*(1-exp(eps*S0*z(j))*(1-exp(gam*eps*I(i)*t)))^-1;
end
end

clims = [58.3 58.5];
imagesc(1000*x,-1000*z,S',clims);
xlabel('x (mm)');
ylabel('Depth (mm)');
colorbar;
```

2) Photoinitiator (Irgacure 651) concentration after exposed by a prism-like pattern.

```
%initiator concentration vs time; Prism distribution

x=-1.5e-4:1e-6:1.5e-4;        % Beam width
I0 = 200*3.05e-6;            % Peak intensity
S0 = 58.5;                  % Initial initiator concentration
eps = 20;                   % Extinction
gam = 0.1;                  % Quantum yield
I=zeros(1,length(x));
t = 1.3;                    % Exposure time
```

```
for i=1:(length(x)-1)/2                   %form intensity distribution
      I(i)=I0*(min(x)-x(i))/min(x);
      end

      for i=(length(x)+1)/2:length(x)
         I(i)=I0*(max(x)-x(i))/max(x);
      end

z = linspace(0,-0.002,1000); % surface to 2 mm deep
S = zeros(length(x),length(z));
for i=1:length(x)
for j=1:length(z)
   S(i,j)=S0*(1-exp(eps*S0*z(j))*(1-exp(gam*eps*I(i)*t)))^-1;
end
end

%clims = [58.4 58.5];
imagesc(1000*x,-1000*z,S');
xlabel('x (mm)');
ylabel('Depth (mm)');
colorbar;
```

3) Monomer (HDDA) conversion rate after exposed by a hemispherical pattern.

```
%Polymerization Conversion

clear

x=-1.5e-4:1e-6:1.5e-4;      % Define beam diameter
I0 = 200*3.05e-6;          % Define peak intensity in Einstein
S0 = 58.5;                % Initial concen of initiator
eps = 20;                 % Extinction coef
gam = 0.1;                % Quantum yield
I=zeros(1,length(x));      % Initialize light intensity as zero
t = 0:0.01:3;              % total observed time = exposure time +
post-exposure time
exposure_t = 1.3;          % exposure time
d_t = max(t)/length(t);     % time step
kp = 1.2e2;                % Propagation coef
kt = 2.13e2;               % Terminiation coef

z = linspace(0,-0.005,100); % Define vertical dimension
S = zeros(length(x),length(z)); % form matrix for initiator concen
R = zeros(length(x),length(z)); % form matrix for radical concen
M = zeros(length(x),length(z)); % form matrix for monomer concen
M(:,:) = 3.54e3; % define initial monomer concen
```

```
for k=1:length(t)-1

   if t(k)<=exposure_t                         %exposure period
     for i=1:length(x)                         %form intensity distribution
     I(i)=I0/max(x)*(max(x)^2-x(i)^2)^0.5;
     end
   else I(:)=0;                                %dark period
   end

   for i=1:length(x)
     for j=1:length(z)
     S(i,j)=S0*(1-exp(eps*S0*z(j))*(1-exp(gam*eps*I(i)*t(k))))^-1; %
initiator concen
     S_plus(i,j)=S0*(1-exp(eps*S0*z(j))*(1-exp(gam*eps*I(i)*t(k+1))))^-
1;
     end
   end
   R_plus=S-S_plus+R-d_t*kt.*R.^2;
   M_plus=M+d_t*-1*kp.*M.*R;
   R=R_plus;
   M=M_plus;
end

Conversion = (M-3.54e3)./3.54e3;
contour(1000*x,-1000*z,Conversion');
[C,h] = contour(1000*x,1000*z,Conversion');
set(h,'ShowText','on','TextStep',get(h,'LevelStep')*2)
colormap cool
xlabel('x (mm)');
ylabel('Depth (mm)');
```

Bibliography

Chapter 1

[1] Yang, J.N., Liu, Y.J., Rauch, C.B., Stevens, R.L., Liu, R.H., Lenigk, R., Grodzinski, P.., *High sensitivity PCR assay in plastic micro reactors.* Lab on a Chip, 2002. **2**(4): p. 179-187.

[2] Baldini, L., Wilson, A. J., Hong, J., Hamilton, A.D., *Pattern-based detection of different proteins using an array of fluorescent protein surface receptors.* Journal of the American Chemical Society, 2004. **126**(18): p. 5656-5657.

[3] Chua, C.K., Leong, K.F., *Rapid Prototyping: Principles and Applications in Manufacturing,* John Wiley, Singapore, 1997.;

[4] Chu, T.M.G., Orton, D.G., Hollister, S.J., Feinberg, S.E., Halloran, J.W., *Mechanical and in vivo performance of hydroxyapatite implants with controlled architectures.* Biomaterials, 2002. **23**(5): p. 1283-1293.

[5] Cabral, J.T., Hudson, S.D., Harrison, C., Douglas, J.F., *Frontal photopolymerization for microfluidic applications.* Langmuir, 2004. **20**(23): p. 10020-10029.

[6] Nguyen, L.H., Straub, M., Gu, M., *Acrylate-based photopolymer for two-photon microfabrication and photonic applications.* Advanced Functional Materials, 2005. **15**(2): p. 209-216.

[7] Moreau W.M., *Semiconductor Lithography:Principles and Materials,* Plenum, New York, 1988..

[8] Intel New Release, *Intel First to Demonstrate Working 45 nm Chips*, Jan, 2006.

[9] Pease, R.F.W., *Nanolithography and Its Prospects as a Manufacturing Technology.* Journal of Vacuum Science & Technology B, 1992. **10**(1): p. 278-285.

[10] Hand, A., *Infrastructure Steps Closer to EUV Lithography*, Semiconductor International, September 1, 2005.

[11] Colburn, M., Johnson, S., Stewart, M., Damle, S., Bailey, T., Choi, B., Wedlake, M., Michaelson, T., Sreenivasan, S.V., Ekerdt, J., Willson, C.G., *Step and Flash Imprint Lithography: A new approach to high resolution patterning*, Proc. SPIE, Emerging Lithographic Technologies III, (1999) **379**: p. 3676.

[12] Chou, S.Y., Krauss, P.R., Renstrom, P.J., *Nanoimprint lithography.* Journal of Vacuum Science & Technology B, 1996. **14**(6): p. 4129-4133.

Chapter 2

[1] Procedure number: National Inpatient Profile 1991 Data, Hospital Discharge Survey, length of stay, 1991 Diagnostic Related Groupings, Federal Register, Department of Health and Human Services (Medicare-based information).

[2] American Liver Foundation, Vital Statistics of the United States. 1988.

[3] Langer, R., Vacanti, J.P., *Tissue Engineering.* Science, 1993. **260**(5110): p. 920-926.

[4] Hutmacher, D.W., Goh, J.C.H., Teoh, S.H., *An introduction to biodegradable materials for tissue engineering applications.* Annals Academy of Medicine Singapore, 2001. **30**(2): p. 183-191.

[5] M. Madou, *Fundamentals of Microfabrication*, CRC, 2002.

[6] Zhang, X., Jiang, X.N., Sun, C., *Micro-stereolithography of polymeric and ceramic microstructures.* Sensors and Actuators a-Physical, 1999. **77**(2): p. 149-156.

[7] Kai, C.C., Fai, L.K., Liquid-based rapid prototyping systems. In *Rapid Prototyping: Principles and Applications in Manufacturing*. 1st Ed, pp 27-77, John Wiley & Sons, New York, 1997.

[8] Kawata, S., Sun, H., Tanaka, T., Takada, K., *Finer features for functional microdevices - Micromachines can be created with higher resolution using two-photon absorption.* Nature, 2001. **412**(6848): p. 697-698.

[9] Takagi, T. and Nakajima, N., *Photoforming applied to fine forming.* Jsme International Journal Series C-Dynamics Control Robotics Design and Manufacturing, 1995. **38**(4): p. 811-817.

[10] Bertsch, A., Lorenz, H., Renaud, P., *3D microfabrication by combining microstereolithography and thick resist UV lithography.* Sensors and Actuators a-Physical, 1999. **73**(1-2): p. 14-23.

[11] Itoga, K., Yamato, M., Kobayashi, J., Kikuchi, A., Okano, T., *Cell micropatterning using photopolymerization with a liquid crystal device commercial projector.* Biomaterials, 2004. **25**(11): p. 2047-2053.

[12] Peppas, N.A., Mikos, A.G., *Preparation methods and structure of hydrogels*, In: Peppas NA (ed.), p. 1-26, *Hydrogels in medicine and pharmacy: Fundamentals*. CRC Press, Boca Raton, FL, 1986.

[13] Anseth, K.S., Newman, S.M., Bowman, C.N., *Polymeric dental composites: Properties and reaction behavior of multimethacrylate dental restorations.* Biopolymers Ii, 1995. **122**: p. 177-217.

[14] Koh, W.G., Revzin, A., Pishko, M.V., *Poly(ethylene glycol) hydrogel microstructures encapsulating living cells.* Langmuir, 2002. **18**(7): p. 2459-2462.

[15] Siegel, R., Howell, J., *Thermal Radiation Heat Transfer*, Taylor & Francis, 2001.

[16] Hutmacher, D.W., *Scaffolds in tissue engineering bone and cartilage.* Biomaterials, 2000. **21**(24): p. 2529-2543.

[17] Woodfield, T.B.F., Malda, J., de Wijn, J., Peters, F., Riesle, J., van Blitterswijk, C. A., *Design of porous scaffolds for cartilage tissue engineering using a three-dimensional fiber-deposition technique.* Biomaterials, 2004. **25**(18): p. 4149-4161.

[18] Cuppone, M., Seedhom, B.B., Berry, E., Ostell, A.E., *The longitudinal Young's modulus of cortical bone in the midshaft of human femur and its correlation with CT scanning data.* Calcified Tissue International, 2004. **74**(3): p. 302-309.

[19] Scherzer, T. and Decker, U., *Real-time FTIR-ATR spectroscopy to study the kinetics of ultrafast photopolymerization reactions induced by monochromatic UV light.* Vibrational Spectroscopy, 1999. **19**(2): p. 385-398.

[20] Anseth, K.S., Kline, L.M., Walker, T.A., Anderson, K.J., Bowman, C.N., *Reaction-Kinetics and Volume Relaxation During Polymerizations of Multiethylene Glycol Dimethacrylates.* Macromolecules, 1995. **28**(7): p. 2491-2499.

[21] Billmeyer, F.W., *Textbook of Polymer Science*, 3rd ed., p. 65, Wiley, New York, 1984.

[22] Studer, K., Decker, C., Beck, E., Schwalm, R., *Overcoming oxygen inhibition in UV-curing of acrylate coatings by carbon dioxide inerting, Part I.* Progress in Organic Coatings, 2003. **48**(1): p. 92-100.

[23] Goodner, M.D., Lee, H.R., Bowman, C.N., *Method for determining the kinetic parameters in diffusion-controlled free-radical homopolymerizations.* Industrial & Engineering Chemistry Research, 1997. **36**(4): p. 1247-1252.

[24] Luck, R.M., Sadhir, R.K., *Expanding Monomers*, pp. 1, CRC Press, Boca Raton, FL, 1992.

[25] Bowman, C.N., Peppas, N.A., *Coupling of Kinetics and Volume Relaxation During Polymerizations of Multiacrylates and Multimethacrylates.* Macromolecules, 1991. **24**(8): p. 1914-1920.

[26] Corkhill, P.H., Fitton, J.H., Tighe, B.J., *Towards a Synthetic Articular-Cartilage.* Journal of Biomaterials Science-Polymer Edition, 1993. **4**(6): p. 615-630.

Chapter 3

[1] Aagard, R.L., *3-Layer Optical-Waveguide for Photolithographic Fabrication of Thin-Film Lenses.* Journal of Vacuum Science & Technology, 1977. **14**(1): p. 275-277.

[2] Basrour, S., Ballandras, S., Hauden, D., *Application of the LIGA process in microoptics.* Annales De Physique, 1995. **20**(5-6): p. 693-700.

[3] Tamagawa, Y. and Ichioka, Y., *Modulation transfer function of blazed diffractive optics produced by diamond turning.* Optical Review, 1999. **6**(4): p. 288-292.

[4] Danzebrink, R. and Aegerter, M.A., *Deposition of optical microlens arrays by ink-jet processes.* Thin Solid Films, 2001. **392**(2): p. 223-225.

[5] Yang, H.H., Chao, C.K., Wei, M. K., Lin, C.P., *High fill-factor microlens array mold insert fabrication using a thermal reflow process.* Journal of Micromechanics and Microengineering, 2004. **14**(8): p. 1197-1204.

[6] Fritze, M., Stern, M.B., Wyatt, P.W., *Laser-fabricated glass microlens arrays.* Optics Letters, 1998. **23**(2): p. 141-143.

[7] Hutley, M.C., *Optical Techniques for the Generation of Microlens Arrays.* Journal of Modern Optics, 1990. **37**(2): p. 253-265.

[8] He, M., Yuan, X.C., Ngo, N.Q., Tao, S.H., *Single-step fabrication of a microlens array in sol-gel material by direct laser writing and its application in optical coupling.* Journal of Optics a-Pure and Applied Optics, 2004. **6**(1): p. 94-97.

[9] Yao, J., Cui, Z., Gao, F.H., Zhang, Y.X., Gao, F., Du, J.L., Su, J.Q., Guo, Y.K., *Design of hybrid micro optical elements with coded gray-tone mask.* Microelectronic Engineering, 2001. **57-8**: p. 793-799.

[10] Liu, J.S., Waddie, A.J., Taghizadeh, M.R., *Fabrication of diffractive-optical elements by using halftone gray-scale masks.* Optics Communications, 2002. **208**(1-3): p. 31-40.

[11] Lu, Y.T., Chu, C.S., Lin, H.Y., *Characterization of the gray-scale photolithography with high-resolution gray steps for the precise fabrication of diffractive optics.* Optical Engineering, 2004. **43**(11): p. 2666-2670.

[12] Gale, M., *Replication, in Micro-optics: elements, systems and applications*, Herzig, H.-P. (ed), p. 152-177, Taylor & Francis, London, 1997,.

[12] Gale, M., *Replication, in Micro-optics: elements, systems and applications*, Herzig, H.-P. (ed), pp. 152-177, Taylor & Francis, London, 1997,.

Chapter 4

[1] Goodner, M.D., Lee, H.R. Bowman, C.N., *Method for determining the kinetic parameters in diffusion-controlled free-radical homopolymerizations.* Industrial & Engineering Chemistry Research, 1997. **36**(4): p. 1247-1252.

[2] Flach, L., Chartoff, R.P., *A Process Model for Nonisothermal Photopolymerization with a Laser-Light Source .1. Basic Model Development.* Polymer Engineering and Science, 1995. **35**(6): p. 483-492.

[3] Pavlinec, J., Moszner, N., *Dark reactions of free radicals crosslinked polymer networks trapped in densely after photopolymerization.* Journal of Applied Polymer Science, 2003. **89**(3): p. 579-588.

[4] Noyes, R.M., Elektrochem., 1960, **64**:, p. 153.

[5] Perry, M.F. and Young, G.W., *A mathematical model for photopolymerization from a stationary laser light source.* Macromolecular Theory and Simulations, 2005. **14**(1): p. 26-39.

[6] Dušek, K., *Network formation involving polyfunctional polymer chains*. In: Stepto RFT (ed). p. 64, *Polymer networks: principles of their formation, structure and properties.* Blackie Academic and Professional, London, 1998.

[7] P.J. Flory, *Principles of Polymer Chemistry,* Cornell University, Press, Ithaca, NY, 1953.

[8] Rubinstein, M., Colby, R.H., *Elastic-Modulus and Equilibrium Swelling of near-Critical Gels.* Macromolecules, 1994. **27**(12): p. 3184-3190.

[9] Gottlieb, M., Macosko, C.W., *On the Suppression-of-Junction-Fluctuations Parameter in Flory Network Theory.* Macromolecules, 1982. **15**(2): p. 535-537.

[10] Muthukumar, M., Winter, H.H., *Fractal Dimension of a Cross-Linking Polymer at the Gel Point.* Macromolecules, 1986. **19**(4): p. 1284-1285.

[11] Young, J.S., Kannurpatti, A.R., Bowman, C.N., *Effect of comonomer concentration and functionality on photopolymerization rates, mechanical properties and*

heterogeneity of the polymer. Macromolecular Chemistry and Physics, 1998. **199**(6): p. 1043-1049.

[12] Kannurpatti, A.R., Bowman, C.N., *Structural evolution of dimethacrylate networks studied by dielectric spectroscopy.* Macromolecules, 1998. **31**(10): p. 3311-3316.

Chapter 5

[1] Chou, S.Y., Krauss, P.R., Renstrom, P.J., *Imprint lithography with 25-nanometer resolution.* Science, 1996. **272**(5258): p. 85-87.

[2] Chou, S.Y., Krauss, P.R., Zhang, W., Guo, L.J., Zhuang, L., *Sub-10 nm imprint lithography and applications.* Journal of Vacuum Science & Technology B, 1997. **15**(6): p. 2897-2904.

[3] Armani, D.K., Liu, C., *Mircofabrication technology for polycaprolactone, a biodegradable polymer.* Journal of Micromechanics and Microengineering, 2000. **10**(1): p. 80-84.

[4] Miller, C., Shanks, H., Witt, A., Rutkowski, G., Mallapragada, S., *Oriented Schwann cell growth on micropatterned biodegradable polymer substrates.* Biomaterials, 2001. **22**(11): p. 1263-1269.

[5] Xia, Q.F., Keimel, C., Ge, H.X., Yu, Z.N., Wu, W., Chou, S.Y., *Ultrafast patterning of nanostructures in polymers using laser assisted nanoimprint lithography.* Applied Physics Letters, 2003. **83**(21): p. 4417-4419.

[6] Ash, B.J., Rogers, D.F., Wiegand, C.J., Schadler, L.S., Siegel, R.W., Benicewicz, B.C., Apple, T., *Mechanical properties of Al2O3/polymethylmethacrylate nanocomposites.* Polymer Composites, 2002. **23**(6): p. 1014-1025.

[7] Ramasubramaniam, R., Chen, J., Liu, H.Y., *Homogeneous carbon nanotube/polymer composites for electrical applications.* Applied Physics Letters, 2003. **83**(14): p. 2928-2930.

[8] Sennett, M., Welsh, E., Wright, J.B., Li, W.Z., Wen, J.G., Ren, Z.F., *Dispersion and alignment of carbon nanotubes in polycarbonate.* Applied Physics a-Materials Science & Processing, 2003. **76**(1): p. 111-113.

[9] Wang, Z. and Pinnavaia, T.J., *Nanolayer reinforcement of elastomeric polyurethane.* Chemistry of Materials, 1998. **10**(12): p. 3769.

[10] Lozano, K., Barrera, E.V., *Nanofiber-reinforced thermoplastic composites. I. Thermoanalytical and mechanical analyses.* Journal of Applied Polymer Science, 2001. **79**(1): p. 125-133.

[11] Biercuk, M.J., Llaguno, M.C., Radosavljevic, M., Hyun, J.K., Johnson, A.T., Fischer, J.E., *Carbon nanotube composites for thermal management.* Applied Physics Letters, 2002. **80**(15): p. 2767-2769.

[12] Fournet, P., Coleman, J.N., Lahr, B., Drury, A., Blau, W.J., O'Brien, D.F., Horhold, H.H., *Enhanced brightness in organic light-emitting diodes using a carbon nanotube composite as an electron-transport layer.* Journal of Applied Physics, 2001. **90**(2): p. 969-975.

[13] Blanchet, G.B., Fincher, C.R., Gao, F., *Polyaniline nanotube composites: A high-resolution printable conductor.* Applied Physics Letters, 2003. **82**(8): p. 1290-1292.

[14] Dyer, P.E., Karnakis, D.M., *High-Quality Arf Laser-Ablation of Photoincubated Polyethylene.* Applied Physics Letters, 1994. **64**(11): p. 1344-1346.

[15] Chen, S., Kancharla, V.V., Lu, Y., *Laser-based microscale patterning of biodegradable polymers for biomedical applications.* International Journal of Materials & Product Technology, 2003. **18**(4-6): p. 457-468.

[16] Chen, G., Tien, C.L., *Thermally-Induced Optical Nonlinearity During Transient Heating of Thin-Films.* Journal of Heat Transfer-Transactions of the Asme, 1994. **116**(2): p. 311-316.

[17] Physical properties of Pyrograf-III were found on the Applied Sciences, website: www.apsci.com.

[18] Wilks, E.S. (ed), *Industrial Polymers Handbook: products, processes, applications*, p. 647, Wiley-VCH, New York, 2001.

[19] Hu, M., Wang, X., Hartland, G.V., Salgueirino-Maceira, V., Liz-Marzan, L.M.., *Heat dissipation in gold-silica core-shell nanoparticles.* Chemical Physics Letters, 2003. **372**(5-6): p. 767-772.

[20] . Huxtable, S.T., Cahill, D. G., Shenogin, S., Xue, L. P., Ozisik, R., Barone, P., Usrey, M., Strano, M. S., Siddons, G., Shim, M., Keblinski, P., *Interfacial heat flow in carbon nanotube suspensions.* Nature Materials, 2003. **2**(11): p. 731-734.

Vita

Yi Lu was born November 18th, 1978 in Hangzhou, China. He did his schooling at Hangzhou High School, Hangzhou and attended college at the Department of Chemistry and Chemical Engineering, Shanghai Jiao Tong University, Shanghai, China. He graduated as a Bachelor of Science in Polymer Science and Engineering in 2001. He earned his Master of Science in Engineering from the Department of Mechanical Engineering at the University of Texas at Austin in 2003.

He continued pursuing his Doctorate in Mechanical Engineering under the guidance of Professor Shaochen Chen at the University of Texas at Austin. His research focused on micro/nano-fabrication of polymeric materials for biomedical and optical applications.

Permanent address: Room 506, No. 11 Hua Jia Chi, Kai Xuan Road, Hangzhou,
Zhejiang, China 310006

This dissertation was typed by the author.